NONLINEAR FIELD DYNAMICS IN GENERAL RELATIVITY:

BLACK HOLE CRITICAL PHENOMENA

AND TOPOLOGICAL DEFECTS

by

STEVEN LAWRENCE LIEBLING, A.B., M.A.

DISSERTATION

Presented to the Faculty of the Graduate School of

The University of Texas at Austin

in Partial Fulfillment

of the Requirements

for the Degree of

DOCTOR OF PHILOSOPHY

THE UNIVERSITY OF TEXAS AT AUSTIN

May 1998

NONLINEAR FIELD DYNAMICS IN GENERAL RELATIVITY:

BLACK HOLE CRITICAL PHENOMENA

AND TOPOLOGICAL DEFECTS

APPROVED BY
DISSERTATION COMMITTEE:

Supervisor: _____

_____

_____

_____

_____

To Tiffany

Acknowledgements

I would like to thank Matthew Choptuik, my thesis advisor, for his assistance and guidance throughout my graduate career.

NONLINEAR FIELD DYNAMICS IN GENERAL RELATIVITY:

BLACK HOLE CRITICAL PHENOMENA

AND TOPOLOGICAL DEFECTS

Publication No. _____

Steven Lawrence Liebling, Ph.D.
The University of Texas at Austin, 1998

Supervisor: Matthew W. Choptuik

Increasingly, numerical simulations are being called upon to answer physical questions that strictly analytic methods have historically either ignored or failed to address. In particular, numerical relativity is beginning to provide answers about dynamical problems lacking the special conditions and symmetries required by the analytic methods. An exceptional example of the success of numerical relativity has been the emergence of the study of nonlinear phenomena occurring at the threshold of black hole formation, *black hole critical phenomena.*

Here, I study critical phenomena occurring for a self-coupled, complex scalar field in spherical symmetry, namely the harmonic map model. The model contains a free constant κ which parameterizes a bifurcation in the stability of the critical solution. The implications of this change in stability are examined in the context of multiply unstable critical solutions. The model also contains two regions in which the non-gravitational, nonlinear effects dominate and the possibility of singularity formation in finite time is discussed. In one of these regions, a new critical solution is found which appears to have a unique structure.

The harmonic map represents the same physical system as a triplet scalar field with a symmetry-breaking ("Mexican hat") potential in the limit where the coupling goes to infinity. Hence the model contains nontrivial topological issues which are addressed in both the harmonic map model with just the two bosonic degrees of freedom and the triplet scalar field model containing all three degrees of freedom. In particular, the triplet scalar field is modeled in flat space and the dynamics of monopoles and texture collapse are studied. These evolutions show that the collapse of toroidally symmetric textures nucleate monopole-antimonopole pairs, while the collapse of so-called spherically symmetric textures do not.

    To answer questions about angular momentum scaling at the threshold of black hole formation and to study the stability of critical solutions to non-spherically symmetric perturbations, a project is undertaken to model axisymmetric gravitational collapse. A significant component of such a project is a method to solve the four elliptic constraint equations, and a solver for that purpose is constructed using multigrid methods. Tests of this solver indicate that it fails to adequately handle the boundary conditions and requires further development.

Table of Contents

List of Tables

List of Figures

xiv

Chapter 1

Introduction

Despite the successes of quantum field theory and string theory, classical field theory still holds secrets. Arguably one of the most interesting of these classical field theories is Einstein's geometric description of gravity, general relativity (GR), elegantly expressed as one tensor equation

$$G_{\mu\nu} = 8\pi T_{\mu\nu}, \tag{1.1}$$

where $G_{\mu\nu}$ is a rank two tensor describing the curvature of the universe and $T_{\mu\nu}$ describes the stress-energy contained in that universe. Without the requisite skills in tensor algebra, this equation yields little insight.

However, general relativity can also be described with a Lagrangian formulation. This formulation is equivalent to the "principle of least action" which tells us that classically free projectiles travel in straight lines. Given an action for a field theory, solutions to the theory are simply those fields which make the action an extremum. Once a correct action is constructed, varying the action yields the equations of motion. For general relativity with no matter or non-gravitational energy, the action is

$$S = \int d^4x \sqrt{-g} \; R \tag{1.2}$$

where R is the Ricci scalar describing the curvature of the universe, $\sqrt{-g}$ is the determinant of the spacetime metric $g_{\mu\nu}$, and $\sqrt{-g} \; d^4x$ is the appropriate volume element over which to integrate. Variation of this action with respect to changes in $g_{\mu\nu}$ yield Einstein's equation in vacuum $G_{\mu\nu} = 0$.

Vacuum gravity is not a universe empty of everything as the name might suggest. This theory contains black holes, possibly charged and spinning, gravitational radiation, and singularities. However, the above action (1.2) can serve as a base on which various other nonlinear theories can be constructed. The addition of a real scalar field ψ, for example, changes the action to

$$S = \int d^4x \sqrt{-g} \Big[R - \psi_{,\mu}\psi^{,\mu} \Big] \tag{1.3}$$

1

where partial differentiation is represented by $\psi_{,\mu} = \partial\psi/\partial x^{\mu}$. The possibility of studying every field theory that can be constructed in this way may seem at first arbitrary, disconnected from some reality, or, worse yet according to many physicists, too *mathematical*. However, these studies answer questions about what is possible in relativity, a theory with an acclaimed history of proving itself under experimental scrutiny [92].

For example, consider the idea of inflation which asserts that the universe expanded exponentially in time from an extremely small size. This paradigm has had much success in explaining, among other things, the structure in the universe occurring on all scales. This paradigm, however, requires a field, generally taken to be a scalar field, to drive the inflation, and no experimental evidence has sprung forth to demonstrate the existence of any scalar field in nature. In fact many physicists are currently exploring various scalar field theories in an effort to fine tune the turn-on and turn-off of inflation so that their results match physical observables of the universe. All this work occurs to describe the physical universe with a theory consisting of scalar fields despite the fact that no one has seen a scalar field!

This work concerns itself mainly with the modeling of gravitational collapse of scalar fields. It is with gravitational collapse that general relativity differentiates itself most from Newtonian gravity. While the accurate prediction of the shift of the perihelion of Mercury demonstrated that GR is a more accurate description of gravity than Newtonian, that effect, and others like it occurring in orbiting astrophysical systems, are often well approximated by perturbation theory around the Newtonian answer [92]. More globally, the topological and causal aspects of GR also attract much attention but are less amenable to numerical modeling than gravitational collapse precisely because they are global.

Gravitational collapse is interesting in part because of the possibility of singularity formation. In simple mathematics, a singular point might occur in some equation such as $y = (2 - x)^2 / (1 + x)$. Here, when $x = -1$, the equation fails to give any information as to what y is. Defining a singularity in general relativity is not as simple [89]. Roughly, a point in spacetime where some physical quantity invariant with respect to changes of coordinates is either not defined or not finite represents a singularity of that spacetime. At these singularities, Einstein's theory does not give us any physical information.

Whereas in mathematics, one can simply assert that the function $y(x)$ is not defined on the domain of $x = -1$, physicists are stuck with the domain that is the universe. Hence, were we to view a singularity through our telescope, lacking any information about this point, we could observe literally anything coming from it. Of course, once this "stuff" leaves the singular point it would have to obey the physical laws. However, the singular point itself is somewhat like a get-out-of-jail-free-card.

Gravitational collapse can produce these singularities, however, in general they occur inside a black hole. The black hole hides the singularity from observers in the rest of the

universe. A conjecture called "cosmic censorship" posits that these singularities generically form inside a horizon such as a black hole and are hidden to observation (for a review see [90]). The proof or disproof of this conjecture attracts significant effort, the implications of its validity possibly being quite significant.

Success has been found in finding so-called naked singularities, those singularities not hidden behind a horizon. However, the issue of whether these naked singularities are generic is significant here. Suppose the universe were a tabletop on which various pencils were scattered in some pencil big bang. Also suppose that dire circumstances awaited any resident of this universe were they to come upon a pencil balanced on its graphite point. These pencil cosmologists would then try to determine the chances of there being pencils standing on their points, the possibility of which is quite small. In this situation, discovery of a pencil balanced on its point would be non-generic.

The naked singularities found so far in general have been non-generic requiring either the worst of luck or precise engineering of some part of the universe. One example of such a non-generic naked singularity occurs in the study of critical phenomena.

As mentioned before, strong field effects of GR appear in gravitational collapse, and it is these strong field effects that hold so much interest. However, the collapse of very little energy fails to excite any strong field effects. In between strong field and weak field lies the region in which black hole critical phenomena occur.

Take for example some spherical shell of energy and let it collapse. For a small initial amount of energy, the radius of this shell initially shrinks due to gravity. At some point, however, the inherent tendency of the energy to disperse counteracts the gravity and the radius then increases as the energy disperses to infinity.

The evolution of a large amount of initial energy behaves quite differently. The radius of the shell initially shrinks due to gravity as before. However, for a sufficiently large amount of energy, the shell contracts to less than its Schwarzschild radius and a black hole is formed. Any energy not trapped within the event horizon of the black hole generically disperses to infinity in keeping with the *no-hair theorem*. This conjecture (the use of "theorem" is a misnomer) posits that any black hole will settle down into a stationary one completely describable by only three numbers, the mass, angular momentum, and charge. In this way, any two black holes with these same three numbers (the black hole's hair, so-to-speak) would be indistinguishable, and we would not be able to determine how each was formed. Hence, the scalar field outside the black hole must, according to the conjecture, radiate away if it is not trapped inside the black hole. While the conjecture appears to require some weakening in order to be proven, numerical evolutions show that indeed the scalar field does radiate away.

Unlike regular fermionic matter for which the Chandrasekhar limit imposes a finite minimum mass, Choptuik modeled this collapse numerically and found that his model could form black holes of ever decreasing mass dependent only on the resolution afforded by the code [24]. This result is important because in the limit that the mass goes to zero, a solution is found which has no black hole (or event horizon) but retains the singularity. Lacking a horizon to hide the singularity, it becomes naked.

These singular solutions are called critical solutions because they are precisely balanced between dispersal and collapse. They result from a very deliberate process of tuning down the black hole mass until you approach the critical solution. They are obviously not generic though Hawking conceded a bet as a result of this work [15, 52]. Though non-generic, these critical solutions require the tuning of only one parameter. In contrast, to balance a pencil on a table would require the tuning of at least two parameters, the azimuthal angle and the angle it forms with the table.

Perhaps more interesting than the cosmological implications for cosmic censorship are the aspects similar to those studied in nonlinear dynamics. Choptuik found that the critical solution resulting from one family of initial data was identical to that found by tuning any family he could construct. This independence on initial data indicated the solution was universal. Further, he found that the black hole mass for those configurations above, but near, criticality (*supercritical* configurations), followed a power law for some exponent γ which was also universal with respect to initial data.

Even more intriguing was the discovery that the critical solution found exhibits a type of self-similarity. Self-similarity describes something which looks identical regardless of what scale is used to observe. For example, imagine a line. Now in the mind's eye, rescale the mental picture as if you were zooming out on a copy machine. This will look identical to your first mental picture. Now, try to do the same thing with a circle. The pictures are not the same. The line is self-similar, but the circle is not. The key here is that associated with the line is just some arbitrary angle with respect to some axes. This angle is not altered by the scale transformation. However, the circle has a definite length associated with it, the radius of curvature. This length sets the scale of your mental picture because this length changes with scale transformations. The self-similar critical solutions are invariant with respect to a special kind of scale transformation as discussed further in Chapter 2.

The results of Choptuik near the threshold for black hole formation are entirely due to his numerically modeling of the evolution of the collapse of a scalar field. So-called analytic work (operationally defined as work *not* involving any numerics) had not predicted any such interesting phenomena. The few closed-form solutions of Einstein's equations that exist have come from simplifying assumptions to reduce the complexity of the equations to be solved. For example, the Schwarzschild solution is derived assuming a static and spherically

symmetric ansatz for the spacetime. Other analytic solutions can be found substituting a CSS ansatz for the static ansatz. However, lacking some assumption such as static, the field equations remain a very complicated set of partial differential equations (PDE) even in spherical symmetry.

The success of this discovery, and the new field of interest that has opened up as a result, indicate a bright future for numerical relativity. After all, the modeling of PDEs on a numerical grid resembles a nonlinear perturbative model of the field theory where the perturbation parameter is the grid spacing and is continuous. With a well written model, the behavior in the limit that the grid spacing goes to zero is well defined, measurable, and leads to the continuum limit.

This introduction has only briefly introduced critical phenomena and Chapter 2 presents more details. This chapter is then followed by a discussion of critical phenomena in the Brans-Dicke model in Chapter 3. This chapter summarizes work by Choptuik and myself in which we find two distinct self-similar critical solutions present in the model at the threshold for black hole formation. In the region of parameter space in which the model approximates GR, Choptuik's original critical solution is found. However, as the coupling parameter is changed, a bifurcation occurs and a different critical solution is observed.

The stability of a family of irregular, spherically symmetric, static solutions in the Brans-Dicke model is studied in Chapter 4. A linear perturbation analysis is conducted, and one unstable mode is found. This study is complemented by fully nonlinear, numerical evolutions of the static solution in which a perturbation is introduced. These evolution confirm the results of the perturbation analysis and suggest that these static solutions represent critical solutions.

As a generalization of the Brans-Dicke model studied in Chapters 3 and 4, the harmonic map has a rich parameter space. The model is motivated by inducing a metric on an internal target space and is parameterized by the constant curvature of this space. The geometric roots of the theory make it quite elegant. In Chapter 5, I present the harmonic map and discuss various aspects of the theory which make it interesting, in particular the correspondences of the model to other models such as Brans-Dicke gravity.

The harmonic map model duplicates the critical phenomena observed in Chapter 3 in the region of parameter space in which the models are equivalent. However, as a generalization of Brans-Dicke gravity, the parameter space is now enlarged, and in this new region, a new critical solution is found. While the previously mentioned critical solutions display forms of self similarity, the symmetry of this new critical solution is not yet clear. Discussion of this new solution is contained in Chapter 6.

The presence of multiple critical solutions in the harmonic map whose stability depends on the curvature of the target space allows the study of multiply unstable critical

solutions. Chapter 6 concludes with a discussion of these multiply unstable critical solutions and the process by which two unstable modes can be tuned.

The results just mentioned have all assumed spherical symmetry. This assumption greatly simplifies the computational problem and equations of motion, but it also excludes the possibility of gravitational degrees of freedom, angular momentum, and non-spherical collapse. Hence, a model capable of modeling collapse only assuming symmetry about an axis, *axisymmetry*, would be quite useful.

As a step towards completion of such a model, the modeling of a charged scalar field in axisymmetric flat space is undertaken in Chapter 7. Various tests of the code are described which show the code to be fully second-order convergent.

Motivated both by the success in axisymmetry and by the nontrivial topological issues presented by the harmonic map, a study of the collapse of Hopf textures is described in Chapter 8. The issue of monopole pair nucleation from the collapse of texture is clarified.

Rounding out these chapters, I describe the current state of a fully gravitational, axisymmetric collapse model in Chapter 9. I present a brief discussion of the derivation of the (2+1)+1 equations, and then discuss the construction of a multigrid solver to solve the four elliptic constraints. Tests show that this solver needs further development in order to properly handle the boundary conditions.

Finally, I conclude in Chapter 10 and discuss further work.

Chapter 2

Theoretical Aspects of Critical Phenomena

Good review articles on critical phenomena have been published recently so I present only a brief discussion here of the features of critical phenomena [10, 39, 40].

The work presented here describes the collapse of scalar fields. Scalar fields are infinite dimensional, requiring in general the specification of the field at an infinite number of points, even on a compact domain. For example, the specification of initial data for a scalar field $\phi(r)$ in spherical symmetry on a compact numerical domain $r = 0 \ldots 10$ has an infinite number of degrees of freedom corresponding to the freedom to specify $\phi(r_i)$ for all $r_i \in [0 \ldots 10]$.

Because of this infinite dimensionality, sketching canonical phase space portraits common to the field of nonlinear dynamics becomes quite difficult. Therefore, instead of beginning with scalar fields, I will introduce some terms borrowed from nonlinear dynamics with a finite dimensional toy model which shares some features of critical phenomena in Section 2.1. With this toy model, the phase space picture is quite clear. Drawing from this toy model, I then introduce the particulars of black hole critical phenomena in Section 2.2.

2.1   Toy Critical Phenomena

Consider an infinitely small ball on a plane (x, y) influenced only by the effects of a potential $V(x, y)$. Let the position of the ball at all times be described by $(x(t), y(t))$.

The equations of motion for the ball are then

$$\begin{aligned} \ddot{x}(t) &= -\frac{\partial V}{\partial x} \\ \ddot{y}(t) &= -\frac{\partial V}{\partial y}. \end{aligned} \tag{2.1}$$

Being a second-order system, the initial data necessary to determine the system for all time consists of the position (x_o, y_o) and velocity (v_o, u_o) of the ball at the initial time $t = 0$.

Let the potential take the form

$$V(x, y) = -A^2 \frac{x^2}{2} - B^2 \frac{y^2}{2} \tag{2.2}$$

such that the equations of motion are then

$$
\begin{aligned}
\ddot{x}(t) &= A^2\, x \\
\ddot{y}(t) &= B^2\, y.
\end{aligned}
\tag{2.3}
$$

The solution to this in terms of the initial data is then

$$
\begin{aligned}
x(t) &= \left(\frac{x_o + v_o/A}{2}\right) e^{At} + \left(\frac{x_o - v_o/A}{2}\right) e^{-At} \\
y(t) &= \left(\frac{y_o + u_o/B}{2}\right) e^{Bt} + \left(\frac{y_o - u_o/B}{2}\right) e^{-Bt}.
\end{aligned}
\tag{2.4}
$$

It is now instructive to consider various permutations of $A^2 = \pm 1$ and $B^2 = \pm 1$. Consider first $A^2 = -1 = B^2$ with zero initial velocity, $v_o = 0 = u_o$. The solution is then

$$
\begin{aligned}
x(t) &= x_o \cos t \\
y(t) &= y_o \cos t.
\end{aligned}
\tag{2.5}
$$

In this case, the potential is just a harmonic well, and the ball oscillates around the point $(0,0)$. For the initial condition $x_o = 0 = y_o$, the ball simply sits at the origin. Hence, the origin is a *fixed point* of the equations. If we were to add a damping term so that the ball steadily loses energy, then it is clear that the ball will eventually settle down to the fixed point. In this case, all trajectories lead to the fixed point and it is called an *attractor*. The *basin of attraction* is the region of parameter space for which trajectories end at the fixed point. For this case, the fixed point $(0,0)$ has the entire plane as its basin of attraction.

These terms are fundamental to the field of nonlinear dynamics and dynamical systems, but my be unfamiliar to relativists. Rigorous definitions can be found in any nonlinear dynamics text such as [35, 36].

Things become more interesting when we flip the sign of B^2 (keeping $v_o = 0 = u_o$) so that the potential becomes

$$
V(x,y) = \frac{x^2}{2} - \frac{y^2}{2}
\tag{2.6}
$$

and the solution is

$$
\begin{aligned}
x(t) &= x_o \cos t \\
y(t) &= \left(\frac{y_o}{2}\right) e^{t} + \left(\frac{y_o}{2}\right) e^{-t}.
\end{aligned}
\tag{2.7}
$$

The potential now looks like a saddle where the point $(0,0)$ is the saddle point. Note that the origin is still a fixed point, however, trajectories near it are not attracted to it as they were in the damped harmonic case above. Instead, consider the trajectory of the initial data $(x_o = 0, y_o = \pm\epsilon)$ for some small ϵ. This configuration begins arbitrarily close to the fixed

point, but as $t \to \infty$ the value of $y(t)$ goes to $\pm\infty$. Clearly then the fixed point is not an attractor. Nearby trajectories are sent away from the fixed point.

That the position along the y-axis grows when the ball is perturbed from the fixed point indicates that the fixed point has an instability. For a fixed point to be an attractor then, it must have no unstable modes associated with it.

The concept of tuning an unstable mode will become important below. To tune the unstable mode in this system the initial data must be expressed as a function of some parameter, generally called p. The construction of this parameterization is not necessarily trivial requiring some knowledge of the nature of the mode so that one is sure a critical solution is a member of the p-family. Here, it is apparent that a family with $y_o = 0$ must be part of the family because the location of the fixed point is known exactly.

Hence, taking the family of initial data

$$x = 3.0 \qquad y = p, \tag{2.8}$$

we examine the trajectory for $p = 1$. This trajectory leads to $y \to \infty$ while x oscillates about $x = 0$. Trying $p = -2$ shows that $y \to -\infty$. So, the critical solution is bracketed. Bisecting this bracket, we try $p = -0.5$ for which $y \to -\infty$, again. The new bracket is $p \in [-0.5 \ldots 1]$. Continuation of this trivial search approaches the critical solution $p = 0$ for which the trajectory, in the damped case, asymptotes to the origin. Because this tuning effectively removes the effect of the unstable mode, fixed points with one unstable mode are called *intermediate attractors* [6].

The case where $A^2 = 1 = B^2$ has the solution

$$
\begin{aligned}
x(t) &= \left(\frac{x_o}{2}\right) e^t + \left(\frac{x_o}{2}\right) e^{-t} \\
y(t) &= \left(\frac{y_o}{2}\right) e^t + \left(\frac{y_o}{2}\right) e^{-t},
\end{aligned}
\tag{2.9}
$$

and the potential looks like a parabolic hill. Again, the point $(0,0)$ is a fixed point, but perturbations in *either* x or y send the trajectory away. Hence, the fixed point now has two unstable modes. Tuning the family of initial data shown in Equation (2.8) only tunes the mode in y. The x position will always tend to plus or minus infinity. Hence, the fixed point is no longer an intermediate attractor.

2.2   Black Hole Criticality as a Phase Transition

Returning now to the scalar field $\phi(r,t)$ coupled to gravity, using a 3+1 ADM decomposition of spacetime into space and time [64, 96], initial data consists of the specification of the field $\phi(r,0)$ and its time derivative $\partial\phi(r,0)/\partial t$ at the initial time. For weak initial data, the

evolution approximates the flat space wave equation in spherical symmetry. For strong-field initial data, a black hole forms. The evolution of the initial configuration can then be thought of as a phase transition from a singularity free space into a space with a black hole. In the limit where the initial energy is just sufficient to form a black hole, the features of this phase transition can then be studied, where the mass of any black hole that forms, M, serves as an order parameter.

Let the scalar field be described initially by a Gaussian pulse with center C, width D, and amplitude A. As with the toy model, consider only time-symmetric initial conditions. Because gravitational radiation is transverse, no gravitational waves propagate in spherical symmetry [64]. The time dependent, spherically symmetric metric is completely determined, up to gauge, by the specification of the scalar field initially, and has no degrees of freedom.

The infinite dimensional configuration space at the initial time has now been reduced, completely arbitrarily, to a three dimensional space (C, D, A). Because the initial energy of the scalar field is proportional to the spatial integral of the square of its derivatives, variation of any of these parameters with the others fixed yields a one-parameter family of initial data.

Because each of (C, D, A) parameterizes the initial energy of the scalar field, it is useful to study the behavior of M with respect to one of these parameters, holding the others fixed. Continuing the analogy with phase transitions, if M has some finite minimum such as the Chandrasekhar limit for fermionic matter, then the phase transition is said to be Type I, because $M(p)$ is discontinuous at the critical point p^*.

If, however, $M(p)$ is continuous, then black holes of arbitrarily small masses form in the limit $p \to p^*$. The first derivative $\partial M(p)/\partial p$ is discontinuous and this is called a Type II phase transition.

In either case, the solution for $p = p^*$ is called the *critical solution* as it separates initial configurations which form black holes from those that do not. In the case of a Type II transition, the solution has a singularity with no horizon. Because the singularity is visible to observers at infinity, the Type II critical solution has a naked singularity.

2.3   Self-Similarities

Only two types of Type II critical solutions have been found, differentiated by the type of self-similarity they possess.

The simpler of the two is continuous self-similarity (CSS). The scalar field $\phi(r, t)$ is CSS if

$$\phi(r, t) = \phi\left(\frac{r}{-t}\right). \tag{2.10}$$
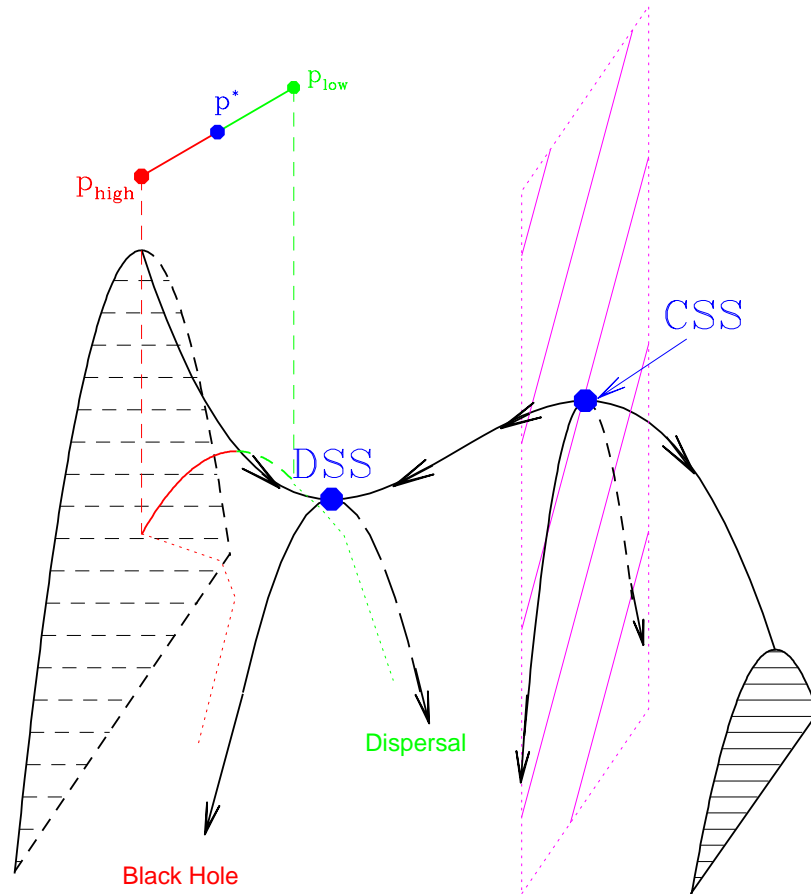
Figure 2.1: Schematic of a section of parameter space. The critical surface separating states which form a black hole from those that disperse is represented by the bold curve running right to left. The DSS and CSS critical solutions are fixed points on the critical surface represented by filled circles. The dotted curves represent the trajectories of field configurations which are either slightly supercritical (p_{high}) or subcritical (p_{low}) and which bracket the critical solution p^*. The arrows on the critical surface show the flow and demonstrate that the DSS is an intermediate attractor while the CSS has two relevant (unstable) modes and is not an intermediate attractor.
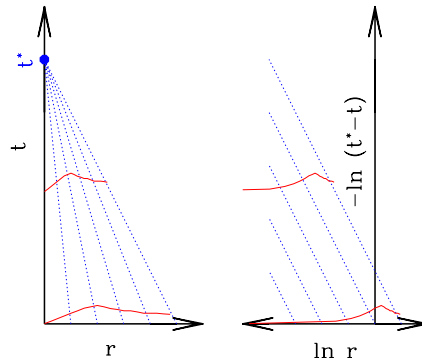
Figure 2.2: Diagram of self-similar solution. Dashed lines represents characteristic lines on which the exactly self-similar solution is constant. The two diagrams are equivalent and represent the same self-similar solution. The diagram on the right shows the solution in more natural units $\ln r$ and -$\ln (t^* - t)$.

Before discussing the aspects of this type of solution, notice that on the left side of Equation (2.10) is a function of two coordinates while that on the right is just one coordinate, $z = -r/t$. Thus, CSS solutions to 1D evolution equations can be found by assuming CSS, and solving the resultant ODEs avoiding the difficulties of solving PDEs. This important point explains the abundance of papers finding these CSS solutions and their perturbative spectra [28, 29, 53, 45, 43, 44, 61].

To better understand the self-similarity of Equation (2.10), define

$$\xi = \ln r \quad \tau = \ln |t| \quad u = \tau - \xi \quad v = \tau + \xi. \tag{2.11}$$

The CSS ansatz then implies

$$\begin{aligned} \phi(r,t) &= \phi(\xi - \tau) \\ &= \phi(u). \end{aligned}$$

In the plane spanned by $\xi \times \tau$ or $u \times v$, a CSS solution simply travels along increasing v with unchanged profile $\phi(u)$ (see Figure 2.2).

The other type of critical solution, and in fact the first type found acting as a critical solution, is discretely self-similar (DSS). For the scalar field to be DSS, it must satisfy

$$\phi(r,t) = \phi(\ln r, \ln |t|) = \phi(\ln r + n\Delta, \ln |t| + n\Delta)$$
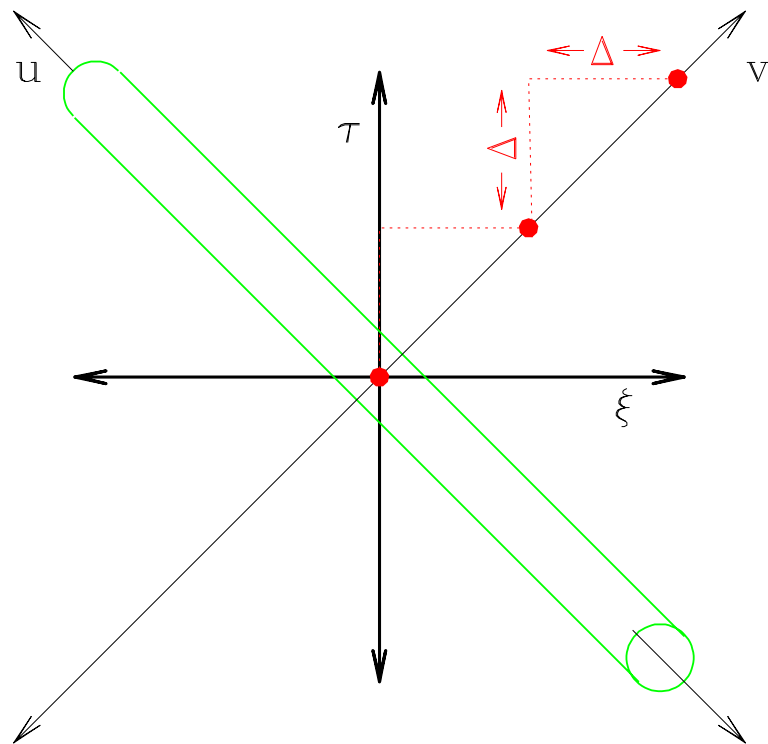
Figure 2.3: Schematic of self-similarity in the $\tau \times \xi$ plane. A CSS solution is defined for all u and whose 'evolution' is trivial in v. In other words, the CSS solution can be translated invariantly along the v direction. In contrast, a DSS solution is defined on the semi-infinite rectangle bounded by some constant coordinate in v, say v_o, and $v_o + \sqrt{2}\Delta$, for all u. Because of the periodicity of the DSS, we can identify the sides of this rectangle $v = v_o$ and $v = v_o + \Delta$ to get an infinite cylinder as shown. The DSS is then the solution obtained by rolling out this cylinder along the v axis.

$$\begin{aligned} \phi(\xi, \tau) &= \phi(\xi + n\Delta, \tau + n\Delta) \\ &= \phi(u, v + n\sqrt{2}\Delta) \end{aligned}$$

for a real constant Δ unique to the solution and arbitrary integer n. Note also that proper time along the axis must be properly normalized so that the period in ξ and the period in τ are the same $\Delta_\tau = \Delta_\xi$.

Consider the DSS again on the $\tau \times \xi$ plane as shown in Figure 2.3. Whereas the CSS is invariant with changes in v, the DSS repeats itself every distance $\sqrt{2}\;\Delta$ along the v axis. If the DSS were DSS for every conceivable value of Δ, it would become CSS. Instead, take the semi-infinite rectangle bounded by $v = 0$ and $v = \sqrt{2}\Delta$. Identify the two edges and form a cylinder. Just as the CSS is defined on a line v constant, the DSS is defined on this infinite cylinder. The evolution of the DSS is can then be pictured by rolling the cylinder along the v axis.

If the cylinder is now turned on its end, you see just a circle. We have projected out the infinite degree of freedom, and we see just a limit cycle. As an evolution in a new time coordinate v, the solution is periodic. Similarly, if we do the same to the CSS, we turn the line on its (nonexistent) end, and see just a point. There is no evolution in v. The CSS is the analog of a limit point.

2.4   Universality

If we take either the CSS or DSS critical solution and analyze its perturbation spectrum, we find that when the critical solution has only one unstable mode, tuning a suitable, but general, one parameter family of initial data will find it in a critical search. That any general family will find it independent of the details of the initial data, indicates that the critical solution is universal.

This universality can be explained by looking at the perturbation spectrum about the critical solution. Consider some solution near the CSS solution in phase space, $\phi(r, t)$. Locally, this solution can be expressed as a sum of the modes around the critical solution

$$\phi(r, t) = \phi_0(u) + \Sigma_{i=1}^{\infty} C_i f_i(u) e^{\sigma_i \tau} \tag{2.12}$$

where $\phi_0(u)$ is the CSS solution. Here, $\tau = \ln|t^* - t|$, where t^* is the collapse time which can be set to zero. The coefficients C_i represent the excitations of the various modes which depend on the distance from criticality $p - p^*$. Because when $p = p^*$ the critical solution must be recovered, then we have $C_i(p^*) = 0$.

If the critical solution has only one unstable mode, then for $|p - p^*|$ sufficiently small, the behavior of this mode will dominate that of the damped modes. Without loss of

generality, let this mode be the first mode such that $\sigma_1 > 0$ is the eigenvalue of the unstable mode. We can then linearize Equation (2.12) around $p = p^*$ to get

$$\phi = \phi_0 + (p - p^*)\frac{dC_1}{dp^*}f_1 e^{\sigma_1 \tau} \tag{2.13}$$

where f_1 is the unstable mode associated with the unstable eigenvalue σ_1. Because ϕ_0 is critical and separates collapse from dispersal, the sign of $p - p^*$ determines whether the non-critical solution disperses or forms a black hole.

Now consider the process of tuning. As one approaches $p - p^* = 0$, the coefficients C_i collectively are tuned to zero, so that $\phi(r, t) \to \phi_0(u)$. However, for $p - p^* \neq 0$, however small that difference may be, the unstable mode will grow exponential in τ. Hence, in the process of tuning, the critical solution will be approached for progressively longer amounts of time as $C_1 \to 0$. Also in this limit, effects due to the damped modes decreases, and hence memory of the initial data vanishes with the coefficients C_i. Near criticality, the solution is dominated by the critical solution and hence the critical solution is universal.

2.5 Mass Scaling

Similar arguments explain the power-law mass scaling observed in the mass of the black holes that form for supercritical evolutions. A self-similar spacetime cannot form a finite mass black hole because no length scale is determined. Here, departures from the self-similar solution determines a length scale and hence the mass of the black hole which eventually forms. In other words, if one compared two near critical solutions, the one that stayed "close" to the self-similar solution longer would have a smaller mass. In order to define this time "close" to the self-similar solution, we pick some fiducial deviation δ. The deviation from the self-similar solution can be found from Equation (2.13)

$$\phi - \phi_0 = (p - p^*)\frac{dC_1}{dp^*}f_1 e^{\sigma_1 \tau}. \tag{2.14}$$

At the point that the perturbed solution reaches some constant and arbitrary deviation δ from self-similarity (as shown in Fig. 2.4), we have

$$\delta = (p - p^*)\frac{dC_1}{dp^*}f_1 e^{\sigma_1 \tau}. \tag{2.15}$$

For the right side to be a constant for any p, then those terms that depend on p must be constant, and hence

$$(p - p^*)e^{\sigma_1 \tau(p)} \tag{2.16}$$

is a constant where $\tau(p)$ depends on p. The mass of the black hole that forms is proportional to this time (the time is the length scale which defines the mass of the black hole). We solve
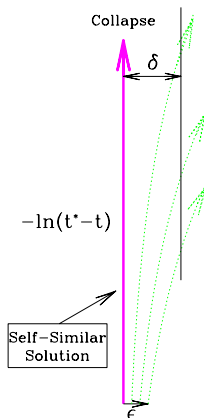
Figure 2.4: Schematic diagram of supercritical perturbations to a self-similar critical solution. The bold line in the center represents the self-similar spacetime. The arrow upwards represents the approach of the critical solution to its singular collapse to the accumulation point, t^*. Near-critical trajectories a distance (in configuration space) $\epsilon = p - p^*$ from the self-similar solution at some early time are shown with dotted lines. These trajectories diverge from the CSS exponentially in τ.

for this length scale to find the scaling relation

$$M_{\rm BH} \propto (t^* - t) \propto (p - p^*)^{1/\sigma_1} \,. \tag{2.17}$$

The mass of black holes that form for near, but super, critical initial data scales with exponent $\gamma = 1/\sigma_1$, where γ is the scaling exponent, and σ_1 is the eigenvalue of the unstable mode.

When considering mass scaling about the DSS critical solution, a periodic deviation, called a "wiggle" in the literature, is predicted by [39] and independently predicted and observed by [48]. To understanding this "wiggle", Equation (2.15) needs to be reexamined. This equation gives a relationship between the distance from criticality and the time at which the solution will depart from self-similarity. With the additional structure of the DSS as compared to the CSS, the time to reach a fiducial deviation δ from self-similarity now depends on where in the DSS cycle this occurs. Every change in $\ln(p - p^*)$ equal to $\Delta/2$, the DSS repeats itself, and hence the black hole mass then scales as

$$\ln M_{\rm BH} = \gamma\,(p - p^*) + c + f\,(\gamma \ln(p - p^*) + c), \tag{2.18}$$

where the function f has period $\Delta/(2\gamma)$.

2.6 The Renormalization Group (RG) Perspective

Much of the understanding of the phenomena explained in terms of linear perturbation analysis above can also be explained in terms of renormalization group ideas. With these RG ideas, Koike, Hara, and Adachi discuss how the critical solution represents a fixed point of a renormalization flow where the scale transformation is manifested as a translation in log time [53]. The arguments presented above then remain the same.

These ideas are extended to a cosmological model in [49]. A general introduction to these ideas as they were originally developed in statistical mechanics is presented by Schmidhuber [78]. Another nice introduction to statistical phase transitions is given by Creutz [19] while an often cited reference is [33].

2.7 Choosing a Coordinate System: Polar-Areal Coordinates

As much of what follows occurs in the polar-areal choice of coordinates, I present the form the Einstein equations take in this choice, generalized for arbitrary stress-energy. Working in spherical coordinates (t, r, θ, φ) and imposing spherical symmetry, scalar functions defined on this spacetime will be functions of coordinate time t and radial coordinate r.

Greek indices run over $0, 1, 2, 3$ on the four manifold while Latin indices run over $1, 2, 3$ on the three manifold. This presentation follows that of Choptuik [22]. Further insight concerning the 3+1 decomposition and initial value formulation of general relativity can be found in [64] and [96].

As much of this work deals with scalar fields, consider a generalized action for a set of scalar fields ϕ^a coupled to gravity with Ricci scalar R

$$S = \int d^4x \sqrt{-g} \left[R + \mathcal{L} \right] = \int d^4x \sqrt{-g} \left[R - \frac{1}{2} G_{bc} \left(\phi^a \right) \phi^b{}_{,\mu} \phi^{c\,,\mu} \right]. \qquad (2.19)$$

The metric associated with the spacetime curvature R is $g_{\mu\nu}$, while G_{bc} is the metric on the internal space of the scalar fields. The indices b and c run over n, the number of scalar fields, and hence the metric G_{bc} is a metric on an internal n-dimensional space. For simplicity, we take $G_{bc} = \text{diag}(1, 1, \cdots n)$ so that the fields only couple to each other through gravity, although for the harmonic map discussed in Chapters 5 and 6, G_{bc} is taken as a metric of constant curvature.

Variations of (2.19) with respect to the metric $g_{\mu\nu}$ yield the Einstein's field equations where the stress energy is

$$T_{\mu\nu} = g_{\mu\nu} \mathcal{L} - 2 \frac{\partial \mathcal{L}}{\partial g^{\mu\nu}}. \qquad (2.20)$$

For the set of scalar fields ϕ^a this takes the form

$$T_{\mu\nu} = \phi^a{}_{,\mu} \phi^{a\,,\nu} - \frac{1}{2} g_{\mu\nu} \phi^a{}_{,\sigma} \phi^{a\,,\sigma}. \qquad (2.21)$$

Variations of the action with respect to the scalar field ϕ^a yield the equations of motion of the matter terms

$$\Box \phi^a = \phi^a{}_{;\mu}{}^{;\mu} = \frac{1}{\sqrt{-g}} \left(\sqrt{-g} \; g^{\mu\nu} \phi^a{}_{,\mu} \right)_{,\nu} = 0. \tag{2.22}$$

To express these equations as an evolution of a three-manifold embedded in four-space, we carry-out a 3+1 decomposition into space and time using as canonically conjugate fields $\left({}^{(3)}g_{ij}, K_{ij} \right)$, two rank two, symmetric tensors defined in 3-space. The tensor K_{ij} is the extrinsic curvature of the 3-slices, and ${}^{(3)}g_{ij}$ is the metric on the 3-slice.

As a first step towards this decomposition, consider a general, spherically symmetric metric

$$ds^2 = \left[-\alpha^2(r,t) + a^2(r,t)\beta^2(r,t) \right] dt^2 + 2a^2\beta \; dt \; dr + a^2 \; dr^2 + r^2 b^2(r,t) \; d\Omega^2 \tag{2.23}$$

on this spacetime. The field $\beta(r,t)$ is the radial, and the only non-vanishing, component of the shift vector $\beta^i = (\beta, 0, 0)$, and $\alpha(r,t)$ is the lapse function. These two functions encompass the coordinate degrees of freedom. The metric is also defined in terms of the two functions $a(r,t)$ and $b(r,t)$ which specify the metric on the 3-slice itself. The term $d\Omega^2$ is the metric on the unit two-sphere.

We have the freedom to choose the condition

$$b(r,0) = 1 \qquad \dot{b}(r,t) = 0. \tag{2.24}$$

for the general metric (2.23). With this choice , the coordinate r is now an areal coordinate such that $4\pi r^2$ yields the proper surface area of a sphere centered at the origin of coordinates.

So far, we have only fully specified the three metric. We have yet to specify how the four manifold is going to be sliced into constant t, 3-slices. To do so, we need some condition on the extrinsic curvature $K^i{}_j$, which in spherical symmetry is diagonal with $K^\varphi{}_\varphi = K^\theta{}_\theta$

$$K_j{}^i = \text{diag} \left(K^r{}_r(r,t), K^\theta{}_\theta(r,t), K^\theta{}_\theta(r,t) \right). \tag{2.25}$$

Letting

$$K \equiv K^i{}_i = K^r{}_r + 2K^\theta{}_\theta, \tag{2.26}$$

we choose the polar slicing condition

$$K = K^r{}_r, \tag{2.27}$$

which is equivalent to the conditions

$$K^\theta{}_\theta = 0 \tag{2.28}$$

$$\dot{K}^\theta{}_\theta = 0. \tag{2.29}$$

The condition (2.29), when substituted into the evolution equation for $K^{\theta}{}_{\theta}$ then implies the slicing condition

$$\alpha' + \left(\frac{1-a^2}{r} - \frac{a'}{a}\right)\alpha = 0. \tag{2.30}$$

Another of the three-metric evolution equations is

$$\dot{b} = -\alpha b K^{\theta}{}_{\theta} + \frac{\beta}{r}(rb)'. \tag{2.31}$$

With the conditions of Equation (2.24), this then implies

$$\beta = \alpha r K^{\theta}{}_{\theta}. \tag{2.32}$$

By the choice of polar slicing and the resultant condition (2.28), however, the right side of the above is zero. Hence, the shift in polar-areal slicing is zero

$$\beta = 0. \tag{2.33}$$

The metric then takes the particularly simple form

$$ds^2 = -\alpha^2(r,t)\ dt^2 + a^2(r,t)\ dr^2 + r^2\ d\Omega^2. \tag{2.34}$$

With the coordinates fixed, we examine the four constraint equations. With the energy density ρ defined as

$$\rho \equiv n_{\mu} n_{\nu} T^{\mu\nu} = \alpha^2 T^{tt}, \tag{2.35}$$

the Hamiltonian constraint

$$R - K^{i}{}_{j} K^{j}{}_{i} + K^2 = 16\pi\rho \tag{2.36}$$

becomes in these coordinates

$$\frac{a'}{a} + \frac{a^2 - 1}{2r} = 4\pi r a^2 \rho. \tag{2.37}$$

Defining the momentum density

$$j_i \equiv n_{\mu} T^{\mu}{}_i = \alpha T^{t}{}_r, \tag{2.38}$$

the momentum constraints are

$$K_i{}^{j}{}_{|j} - K_{|i} = 8\pi j_i, \tag{2.39}$$

where $|$ represents covariant differentiation on the three-space with respect to the three metric. The only non-trivial component of this equation becomes

$$K^{\theta}{}_{\theta}' + \frac{(rb)'}{rb}\left(K^{\theta}{}_{\theta} - K^{r}{}_{r}\right) = -4\pi j_r, \tag{2.40}$$

which simplifies with polar-areal coordinates to

$$K^{r}{}_{r} = 4\pi r j_r. \tag{2.41}$$

Using an evolution equation for the three-metric

$$\dot{g}_{ij} = -2\alpha g_{ik} K^k{}_j + \beta^k g_{ij,k} + g_{ik}\beta^k{}_{,j} + g_{kj}\beta^k{}_{,i}, \tag{2.42}$$

we take the $i = r = j$ component to get an evolution equation for the metric component a

$$\dot{a} = -\alpha a K^r_r + (a\beta)'. \tag{2.43}$$

The combination of Equations (2.41) and (2.43) yields an evolution equation for a

$$\dot{a} = -4\pi\alpha a r j_r. \tag{2.44}$$

Moving on to the matter, introducing the auxiliary fields

$$\Phi^a(r,t) \equiv \frac{\partial}{\partial r}\phi^a(r,t) \qquad \Pi^a(r,t) \equiv \frac{a}{\alpha}\frac{\partial}{\partial t}\phi^a(r,t), \tag{2.45}$$

the equations of motion (2.22) for the scalar fields become

$$\dot{\Phi}^a = \left(\frac{\alpha}{a}\Pi^a\right)' \tag{2.46}$$

$$\dot{\Pi}^a = \frac{1}{r^2}\left(\frac{r^2\alpha}{a}\Phi^a\right)'. \tag{2.47}$$

The energy density and momentum density are

$$\rho = \frac{(\Phi^a)^2 + (\Pi^a)^2}{2a^2} \tag{2.48}$$

$$j^r = -\frac{\Phi^a \Pi^a}{a}. \tag{2.49}$$

With equations in hand, we consider appropriate boundary conditions. Local flatness at the origin is enforced by the condition

$$a(0,t) = 1, \tag{2.50}$$

and regularity of the fields there is enforced by the conditions

$$a'(0,t) = \Phi^a(0,t) = \Phi^a(0,t) = 0. \tag{2.51}$$

By the nature of the 3+1 decomposition, we have the freedom to pick a condition on α on each time slice which corresponds to a global change in the labeling of slices. We impose the condition on α at the large radius boundary of the grid $r_{\max}$

$$\alpha(r_{\max}, t) = \frac{1}{a(r_{\max}, t)}. \tag{2.52}$$

As long as no radiation is escaping from the grid, this condition implies that coordinate time t corresponds to proper time for an observer at $r = \infty$.

The nature of being restricted to a finite grid imposes the need for an artificial boundary condition on the matter fields there. Since our spacetime is asymptotically flat, we impose an approximate outgoing radiation condition on the matter fields. The flat space wave equation for some general scalar field in spherical symmetry

$$\Box \phi^a \Rightarrow (r\phi^a)_{tt} = (r\phi^a)_{rr} \tag{2.53}$$

has the solution

$$r\phi^a = f(r+t) + g(r-t) \tag{2.54}$$

for two general functions f (in-going component) and g (out-going component). To eliminate the in-going component at the outer boundary, we enforce at the boundary the condition

$$\frac{\partial (r\phi^a)}{\partial r} = -\frac{\partial (r\phi^a)}{\partial t} \tag{2.55}$$

with the equations

$$
\begin{aligned}
\dot{\Pi}^a + (\Pi^a)' + \frac{\Pi^a}{r} &= 0 \\
\dot{\Phi}^a + (\Phi^a)' + \frac{\Phi^a}{r} &= 0,
\end{aligned}
\tag{2.56}
$$

which effectively limits reflection off the outer boundary.

The metric (2.34) corresponds to a "dynamical" Schwarzschild metric, allowing the association

$$a^2(r,t) = \left(1 - \frac{2m(r,t)}{r}\right)^{-1}, \tag{2.57}$$

where the field $m(r,t)$ represents the mass aspect function measuring the amount of mass contained within a shell of radius r centered about the origin at coordinate time t. Eq. (2.57) leads to

$$m(r,t) = \frac{r}{2}\left(1 - \frac{1}{a^2}\right), \tag{2.58}$$

so that from the field $a(r,t)$, we can obtain the mass aspect function.

An advantage of polar slicing (and most slicing conditions used in numerical relativity) is that it avoids singularities. Further, because of our use of polar-areal coordinates, we cannot observe the formation of a true horizon which is a coordinate singularity in our coordinates. Instead, by monitoring $m(r,t)/r$ we can observe the formation of a horizon and hence a black hole when $m/r \to 1/2$. Where m/r approaches $1/2$, we can determine the mass of the black hole forming by simply halving the radius where the horizon forms.

2.8 Basic Finite Difference Techniques

In general throughout this work, details of the numerical techniques are only briefly mentioned. The purpose here is to introduce and define some necessary concepts, but this section is by no means a full reference. More in depth information can be found in [22]. For a more formal presentation, a variety of good books on numerical methods exist, one in particular that has been helpful is [41].

Of fundamental importance in a numerical study such as this one, is the method of using *finite differences* to approximate continuum equations. Taking the simplest of examples, consider a field $u(x)$ which satisfies the continuum equation

$$Lu(x) = \frac{du}{dx} = 0, \tag{2.59}$$

where L is a general differential operator, here taken to be differentiation. The derivative here $du/dx \equiv u'$ is defined in the limit where the differential element dx goes to zero. However, we can approximate this equation where we substitute the numerator and denominator with differences taken at two points x_1 and x_2 as

$$\frac{u(x_2) - u(x_1)}{x_2 - x_1} = 0. \tag{2.60}$$

If we now define a set of points representing the spatial domain of x such that the difference between any two adjacent points x_{i+1} and x_i is a constant, then we can speak of a *grid spacing* $\triangle x = x_{i+1} - x_i$. The spatial domain is then the set of x_i such that $x_i = x_{\min} + (i-1)\triangle x$ where $\triangle x = (x_{\max} - x_{\min})/(i-1)$ and $x_{\max}$ and $x_{\min}$ are the bounds of the numerical domain. This set of points is then called a *one-dimensional grid*, and generalizes in the obvious way to more than one dimension.

A convenient way to find an approximation to this operator L, is to first Taylor expand $u(x)$ around some arbitrary x_0

$$u(x_0 + \triangle x) = u(x_0) + \triangle x \; u'(x_0) + \frac{\triangle x^2}{2} u''(x_0) + O(\triangle x^3). \tag{2.61}$$

Re-arranging, we get

$$u'(x_0) = \frac{u(x_0 + \triangle x) - u(x_0)}{\triangle x} - \frac{\triangle x}{2} u''(x_0) + O(\triangle x^2). \tag{2.62}$$

Letting x_0 be some arbitrary grid point x_i and defining the field u_i on all grid points as $u_i \equiv u(x_i)$, then this is just the approximation we were looking for

$$Lu = u' = \frac{u_{i+1} - u_i}{\triangle x} + O(\triangle x). \tag{2.63}$$

This approximation has error terms which have been truncated of order the grid spacing, and so it is said to be first order accurate. Similar analysis shows

$$u' = \frac{u_{i+1} - u_{i-1}}{2\triangle x} + O(\triangle x^2), \tag{2.64}$$

which is called a *centered difference* and is second order accurate.

It is convenient at this point to define *truncation error*. We let $u(x)$ be a continuum solution to the original differential equation (2.59) such that it satisfies exactly

$$Lu = u' = 0. \tag{2.65}$$

We may also find the solution $\tilde{u}$ to the finite difference equation which satisfies exactly

$$\frac{\tilde{u}_{i+1} - \tilde{u}_{i-1}}{2\triangle x} = 0. \tag{2.66}$$

The truncation error τ_i is then defined on the grid and is equal to the difference between these two solutions

$$\tau_i = u(x_i) - \tilde{u}_i, \tag{2.67}$$

and represents the sum of the truncated terms of Equation (2.64). The *residual error* is the difference between a field u_i and the exact solution to the finite difference equation $\tilde{u}_i$

$$r_i = u_i - \tilde{u}_i. \tag{2.68}$$

For many of the errors, a norm is taken over all grid points of the error, and in particular I use the ℓ_2 norm often to describe the behavior of the residual in Chapter 9. The ℓ_2 norm of some field u_i is

$$\|u_i\|_2 = \sqrt{\frac{\Sigma_1^n (u_i)^2}{n}}. \tag{2.69}$$

Many of the problems considered here involve time evolution and so we therefore consider a simple advective equation

$$\dot{u} - u' = 0. \tag{2.70}$$

We can consider time in the same discrete fashion as space where a time coordinate t takes only discrete values $t^n = t_{\min} + \triangle t(n-1)$ where the initial time $t_{\min}$ is generally taken to be zero and $\triangle t$ represents the time step for the evolution. We then use the shorthand

$$u_i^n = u(x_i, t^n) = u(x_{\min} + (i-1)\triangle x, t_{\min} + (n-1)\triangle t). \tag{2.71}$$

Using differences centered in time and space, we arrive at the approximation to Equation (2.70)

$$\frac{u_i^{n+1} - u_i^{n-1}}{2\triangle t} - \frac{u_{i+1}^n - u_{i-1}^n}{2\triangle x} = 0. \tag{2.72}$$

With analysis such as above, this approximation can be shown to be second order accurate in both space and time. That is to say that the error terms are $O(\triangle x^2) + O(\triangle t^2)$. This difference approximation is called a *leap frog* update scheme and involves three time levels of information, namely $n-1$, n, and $n+1$. As Equation (2.72) can be explicitly solved for the desired value u_i^{n+1}, it is an *explicit scheme*.

The advection Equation (2.70) can also be approximated on only two time levels to second order as

$$\frac{u_i^{n+1} - u_i^n}{\triangle t} - \frac{1}{2}\left[\frac{u_{i+1}^{n+1} - u_{i-1}^{n+1}}{2\triangle x} + \frac{u_{i+1}^n - u_{i-1}^n}{2\triangle x}\right] = 0. \tag{2.73}$$

This is called a *Crank-Nicholson scheme* and because it only implicitly defines an update for u_i^{n+1} is called an *implicit scheme*.

For a smooth field u, each of these approximations often work quite well, but for features of order the grid spacing or smaller, the approximations cannot resolve them. The significance of how these approximations deal with non-smooth features cannot be underestimated. If these high-frequency components are allowed to grow in time, the scheme is unstable. A discussion of the stability analysis of any given difference scheme is beyond the scope of this work, but, in general, the stability of a scheme is dependent in part on the ratio of the time step to the grid spacing $\lambda = \triangle t/\triangle x$, which is called the *Courant factor*.

Perhaps the most telling factor in determining the correctness of a finite difference code is showing that the results converge to a unique solution as the resolution is increased. In other words, for high resolutions, the physical results are independent of resolution and hence that differences between two resolution runs decrease with resolution.

One way to measure this is by computing a *convergence factor*. We construct a solution $\tilde{u}^{(1)}$ to the finite difference equations with some grid spacing $\triangle x$. Being second order accurate in $\triangle x$, we expand this solution via a *Richardson expansion* in terms of the continuum solution u and a leading order error function e_2 as [74]

$$\tilde{u}^{(1)} = u + \triangle x^2 e_2 + \cdots. \tag{2.74}$$

We likewise compute the solutions $\tilde{u}^{(2)}$ and $\tilde{u}^{(4)}$ on coarser grids with grid spacings $2\triangle x$ and $4\triangle x$ respectively. As these solutions will all have the error function e_2 in common, we can compute the following quantity at all points common to all the grids, namely points on the coarsest grid,

$$\frac{\tilde{u}^{(4)} - \tilde{u}^{(2)}}{\tilde{u}^{(2)} - \tilde{u}^{(1)}} = \frac{12\triangle x^2}{\triangle x^2} = 4. \tag{2.75}$$

This quantity is the convergence factor, and for second order accurate schemes should be equal to 4. This expansion assumes that higher order terms are small which is often *not* the case when the resolution is low compared to the dynamics. In particular, tests in axisymmetry have indicated that even for a second order accurate code, convergence factors

at low resolutions deviate significantly from the expected value 4. However, as resolution is increased, the convergence factors approach the value 4 as shown in Chapter 7.

A sufficient procedure to generate initial data consistent with the constraints, is to freely specify the matter fields $(\Phi^a,\ \Pi^a,\ \Phi^a,\ \Pi^a)$, on the initial slice, and then use Eqs. (2.37,2.30) to solve for the metric functions a and α respectively.

We approximate the equations with finite difference equations using second-order accurate, center differences. We solve Eq. (2.37) using a point-wise Newton-Rhapson method iterating outwards with the condition (2.50). To obtain α, we take the finite difference approximation to Eq. (2.30) using differences centered about the midpoints between gridpoints. Beginning at the outer boundary, we enforce the boundary condition (2.52) and integrate inwards. This method completes the initial data. However, to obtain the next time step we use the finite difference versions of the equations of motion (2.56) to advance the matter fields, and repeat the procedure outlined above to find the geometry fields a and α.

Chapter 3

Critical Phenomena in Brans-Dicke Gravity

In this chapter, I present work done by Choptuik and myself studying the critical phenomena in Brans-Dicke gravity coupled to a free scalar field [54].

3.1 Introduction

Studies of black hole formation from the gravitational collapse of a massless scalar field have revealed interesting nonlinear phenomena at the threshold of black hole formation [24, 28]. These studies have shown that Einstein's field equations possess solutions which occur precisely at the black hole threshold and which are universal with respect to the initial conditions of the evolution. More specifically, for any type of initial field configuration whose energy is parameterized by some parameter, p, the critical solution occurs at a value of $p = p^*$ such that for all $p < p^*$ no black hole is formed, and for all $p > p^*$ a black hole is necessarily formed. This critical solution, whether obtained with an initial pulse shape such as tanh or a Gaussian pulse, is identical, erasing all detail of the initial field configuration.

Though universal with respect to initial conditions, the critical solution is dependent on the specific matter model involved. In the case of a real scalar field [24], a discretely self-similar solution (DSS) is found, characterized by an echoing exponent Δ. In other words, were an observer to take a snap-shot of the solution at some time t, he would find the same picture as when he zoomed in to a spatial scale $\exp(\Delta)$ smaller than the original at a time $t + \exp(-\Delta)$ later.

In contrast to this DSS solution, other researchers, working in an axion/dilaton model, have found that the equations possess a continuously self-similar (CSS) solution [28]. Because they found this solution by assuming continuous self-similarity and solving the appropriate ordinary differential equations, they could not show whether this CSS solution is indeed a critical solution.

We find that a free real scalar field coupled to Brans-Dicke gravity contains two distinct dynamic critical solutions. As a special case, the model includes the real scalar

field in general relativity and recovers the DSS solution as in [24]. Further, this model is sufficiently general that it contains the model studied in [28] as another special case. For this case, we find that the CSS solution is an attracting critical solution. Hence we present the novel result that for a single matter model, adjustment of a coupling parameter transitions between two unique, dynamic, attracting critical solutions. Because these two solutions are both dynamic, the model is quite different from the Yang Mills model studied in [25].

Subsequent to our study, Hirschmann and Eardley, working in an even more general model, the non-linear sigma model, which includes ours, carried-out a perturbation analysis and confirmed a change in stability near the value we find for the transition coupling parameter [43]. Further, from the eigenvalues of the unstable modes, they have been able to compute mass-scaling exponents. Their results concur with those we find from our numerical evolutions.

3.2   Equations of Motion

We work in spherical symmetry with the metric

$$ds^2 = -\alpha(r,t)^2 dt^2 + a(r,t)^2 dr^2 + r^2 d\Omega^2, \tag{3.1}$$

where $\alpha(r,t)$ represents the lapse function in the 3+1 formalism and r measures proper surface area.

The Brans-Dicke model is described by the field equations

$$G_{\mu\nu} = \frac{8\pi}{\phi(r,t)} T_{\mu\nu}^{\text{total}} \tag{3.2}$$

where $1/\phi(r,t)$ represents the freedom of the conventional gravitational constant to vary [14]. The total stress-energy tensor consists of two terms

$$T_{\mu\nu}^{\text{total}} = T_{\mu\nu}^{\text{matter}} + T_{\mu\nu}^{\text{BD}}, \tag{3.3}$$

where $T_{\mu\nu}^{\text{BD}}$ represents the energy associated with the Brans-Dicke field ϕ and $T_{\mu\nu}^{\text{matter}}$ is the conventional tensor associated with matter sources [14]. For this study our sole matter source is a free massless minimally coupled scalar field $\psi(r,t)$ governed by

$$\Box\psi = 0 \tag{3.4}$$

and whose associated stress-energy is

$$T_{\mu\nu}^{\text{matter}} = \psi_{,\mu}\psi_{,\nu} - \frac{1}{2}g_{\mu\nu}\psi^{,\rho}\psi_{,\rho}. \tag{3.5}$$

The Brans-Dicke field satisfies the generally covariant wave equation

$$\Box\phi = 4\pi\lambda T^{\text{matter}} \tag{3.6}$$

where λ, a constant, represents the strength of the coupling between the Brans-Dicke field and matter [91]. Its associated stress-energy tensor is

$$T_{\mu\nu}^{\phi} = \frac{\omega}{8\pi\phi}\left(\phi_{,\mu}\phi_{,\nu} - \frac{1}{2}g_{\mu\nu}\phi_{,\rho}\phi^{,\rho}\right) + \frac{1}{8\pi}\left(\phi_{;\mu\nu} - g_{\mu\nu}\Box\phi\right) \tag{3.7}$$

where

$$\lambda \equiv \frac{2}{2\omega + 3}. \tag{3.8}$$

The equations described above are said to be in the *Brans-Dicke frame* where masses are constant but inertial forces depend on the distribution of mass in the universe. However, it is possible to transform to a conformally related frame in which the geometry is described by Einstein's field equations coupled to a stress-energy tensor not involving second derivatives of ϕ. In this frame, the *Einstein frame*, masses vary with time, but the gravitational constant is indeed constant.

We achieve this conformal transformation via

$$\begin{aligned} e^{\xi} &\equiv \phi \\ g_{\mu\nu} &\rightarrow e^{\xi}g_{\mu\nu} \\ g^{\mu\nu} &\rightarrow e^{-\xi}g^{\mu\nu} \end{aligned} \tag{3.9}$$

after which we have the equations (now expressed in the Einstein frame)

$$T_{\mu\nu}^{\text{BD}} = \left(\frac{3+2\omega}{16\pi}\right)\left(\xi_{,\mu}\xi_{,\nu} - \frac{1}{2}g_{\mu\nu}\xi^{,\rho}\xi_{,\rho}\right) \tag{3.10}$$

$$T_{\mu\nu}^{\text{matter}} \rightarrow \frac{1}{\phi}T_{\mu\nu}^{matter} \tag{3.11}$$

$$\Box\xi = -4\pi\lambda e^{-\xi}\psi^{,\mu}\psi_{,\mu} \tag{3.12}$$

$$\Box\psi = \psi^{,\mu}\xi_{,\mu}. \tag{3.13}$$

Defining auxiliary variables in terms of the derivatives of the scalar fields

$$\Phi_{\xi} \equiv \frac{\partial}{\partial r}\xi \qquad \text{and} \qquad \Pi_{\xi} \equiv \frac{a}{\alpha}\frac{\partial}{\partial t}\xi \tag{3.14}$$

$$\Phi_{\psi} \equiv \frac{\partial}{\partial r}\psi \qquad \text{and} \qquad \Pi_{\psi} \equiv \frac{a}{\alpha}\frac{\partial}{\partial t}\psi \tag{3.15}$$

so that Equations (3.12) and (3.13) can be written in first order form as

$$\begin{aligned} \dot{\Phi}_{\xi} &= \left(\frac{\alpha}{a}\Pi_{\xi}\right)' \\ \dot{\Pi}_{\xi} &= \frac{1}{r^2}\left(\frac{r^2\alpha}{a}\Phi_{\xi}\right)' + 4\pi\lambda e^{-\xi}\frac{\alpha}{a}\left(\Phi_{\psi}^2 - \Pi_{\psi}^2\right) \\ \dot{\Phi}_{\psi} &= \left(\frac{\alpha}{a}\Pi_{\psi}\right)' \\ \dot{\Pi}_{\psi} &= \frac{1}{r^2}\left(\frac{r^2\alpha}{a}\Phi_{\psi}\right)' + \frac{\alpha}{a}\left(\Pi_{\psi}\Pi_{\xi} - \Phi_{\psi}\Phi_{\xi}\right). \end{aligned} \tag{3.16}$$

The only other necessary conditions come from the field equations, which, in the Einstein frame, are simply Einstein's field equations, $G_{\mu\nu} = 8\pi T_{\mu\nu}$. In accordance with the 3+1 formalism, we have the Hamiltonian constraint

$$a' = -\frac{a^3 - a}{2r} + 2\pi a r \left(e^{-\xi} \left(\Phi_\psi^2 + \Pi_\psi^2 \right) + \frac{1}{8\pi\lambda} \left(\Phi_\xi^2 + \Pi_\xi^2 \right) \right) \tag{3.17}$$

and the polar slicing condition

$$\alpha' = -\left(\frac{1 - a^2}{r} - \frac{a'}{a} \right) \alpha, \tag{3.18}$$

which enable us to solve for the geometry in terms of the two sources, ψ and ξ (as seen in Eqs. (2.37) and (2.30)). The derivation of these equations within the context of this choice of coordinates occurs in Section 2.7 following the formal procedure outlined in [64, 96]. These equations suffice to evolve both the fields $\psi(r,t)$ and $\xi(r,t)$, and the geometric variables $\alpha(r,t)$ and $a(r,t)$ [55].

To show that the model found in [28] is a special case of our model, we compare our Lagrangian

$$L^{\mathrm{BD}} = -\frac{1}{2} e^{-\xi} \psi^{,\rho} \psi_{,\rho} - \frac{1}{16\pi\lambda} \xi^{,\rho} \xi_{,\rho} \tag{3.19}$$

with that of [28]

$$L^\tau = -\frac{1}{32\pi} \left(e^{4\phi} a_{,\mu} a^{,\mu} + 4\phi_{,\mu} \phi^{,\mu} \right), \tag{3.20}$$

defined in terms of the axion, a, and the dilaton, ϕ. Comparing Eqs. (3.19) and (3.20), we see a correspondence between the two models with a trivial rescaling of the fields

$$\xi = -4\phi \qquad \psi = \frac{1}{\sqrt{16\pi}} a \qquad \lambda = 8. \tag{3.21}$$

3.3 Critical Results

We have found the critical solutions for a variety of initial data. Specifically, we input the initial configuration of the two fields, and specify the value of λ. The space of initial configurations is schematically represented in Fig. 3.1.

We observe for an initially vanishing scalar field that Eqs. (3.16, 3.17, 3.18) describe the real scalar field case studied in [24]. Consistent with this observation, our results recover the same DSS solution found for the real scalar field case. The equivalence between this model with $\psi(r,t) = 0$ and that of the real scalar field is shown in Fig. 3.1 as the vertical line extending through the middle of the graph.

When $\lambda \to 0+$, Weinberg shows that the Brans-Dicke model goes over to general relativity [91]. Hence, for the general situation in which both fields are present ($\psi/\xi \neq 0$), we expect to recover the results from general relativity. We do recover the general relativity
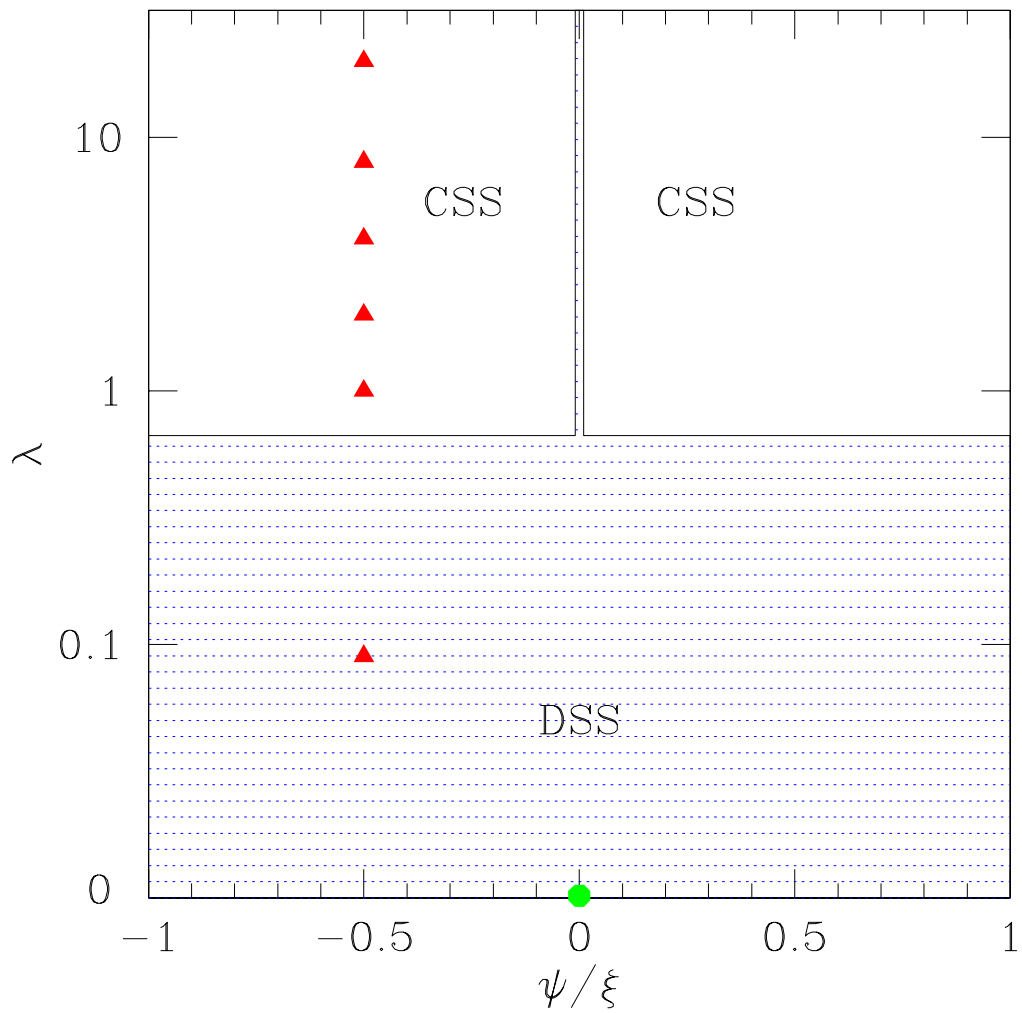
Figure 3.1: Schematic of the configuration space. The horizontal axis represents the mixing ratio between the free scalar field and the Brans-Dicke field. The darkened triangles represent the locations of the profiles displayed in Fig. 2. The darkened circle represents the location of the real scalar field in general relativity studied in [1]. For $\lambda < 2/3$, only the DSS solution is the attractor. Above $\lambda \approx 2/3$ the CSS solution attracts whenever both fields are initially present.

result, that being the DSS solution. As shown in Fig. 3.1, the critical solution is discrete for generic initial data as λ is increased up to $\lambda \approx 2/3$.

Shown in Fig. 3.2 for $\lambda = 0.09$, we have verified that this is the same DSS solution obtained for the real scalar field in general relativity [24]. In Table 3.1, we show the computed values of the echoing exponent Δ. These values correspond to that found in [24].

Around $\lambda \approx 2/3$, a remarkable transition occurs in the critical solution. As one increases λ in this region, the echos displayed by the critical solution are damped by a decreasing envelope as shown in Fig. 3.2.

At $\lambda = 8$, we recover, as expected from Eq. (3.21), the CSS solution found in [28]. In Fig. 3.3 we demonstrate that the solution found by [28] by demanding continuous self-similarity is indeed the attracting critical solution. Here we show that by a trivial rescaling of the fields at one time slice, our solution is identical to theirs.

Both the critical solutions exhibit mass-scaling in the supercritical regime. Specifically, for some family of solutions where p^* represents the critical value of a parameter, the masses of the black holes formed in the regime where $p > p^*$ follow

$$M_{\text{BH}} \sim c(p - p^*)^\gamma \qquad (3.22)$$

where γ depends on λ and c is a family dependent constant. Fig. 3.5 shows four power law fits and the associated γ's.

In keeping with the correspondence between this model for very small λ and that of general relativity, we find $\gamma = 0.37$, matching that found in [24]. Likewise, we find agreement between our values of γ and those found by perturbation analysis in [43]. We display both these sets of values in Fig. 3.4.

The appearance of these two disparate solutions leads one to examine the transition in λ-space from the DSS to the CSS. Bracketing solutions have shown that around $\lambda = 2/3$ the transition occurs (see Fig. 3.2). As λ is increased around this transition value, an envelope dampens the discrete echos into the smoothly continuous self-similar solution. Perturbation results in the non-linear sigma model confirm a change in stability of the CSS solution near $\lambda = 2/3$ [43].

The model studied here for $\lambda > 0$ is generalized by the harmonic map studied in Chapter 5, and further study of this change in stability can be found in Chapter 6. However, when $\lambda < 0$, the coupling of the two scalar contributions in the Lagrangian (3.19) change sign with respect to each other. This region of parameter space has not been studied.
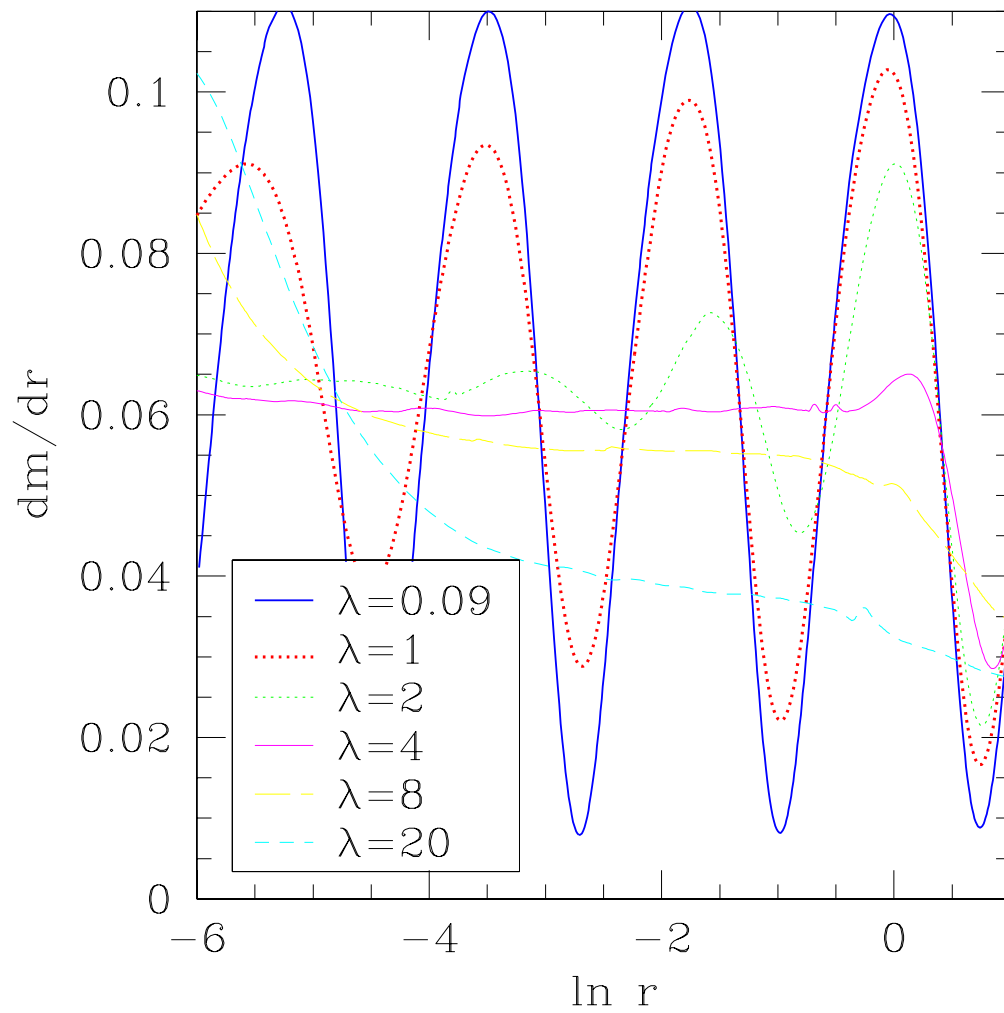
Figure 3.2: Demonstration of regime in which the solution transitions from the DSS to the CSS. We show here the mid-section of the seven solutions for various λ. For $\lambda = 0.09$ the solution is clearly the DSS, however the next solution demonstrates that the echoes get damped as one moves towards the origin. Eventually the solutions become the CSS.
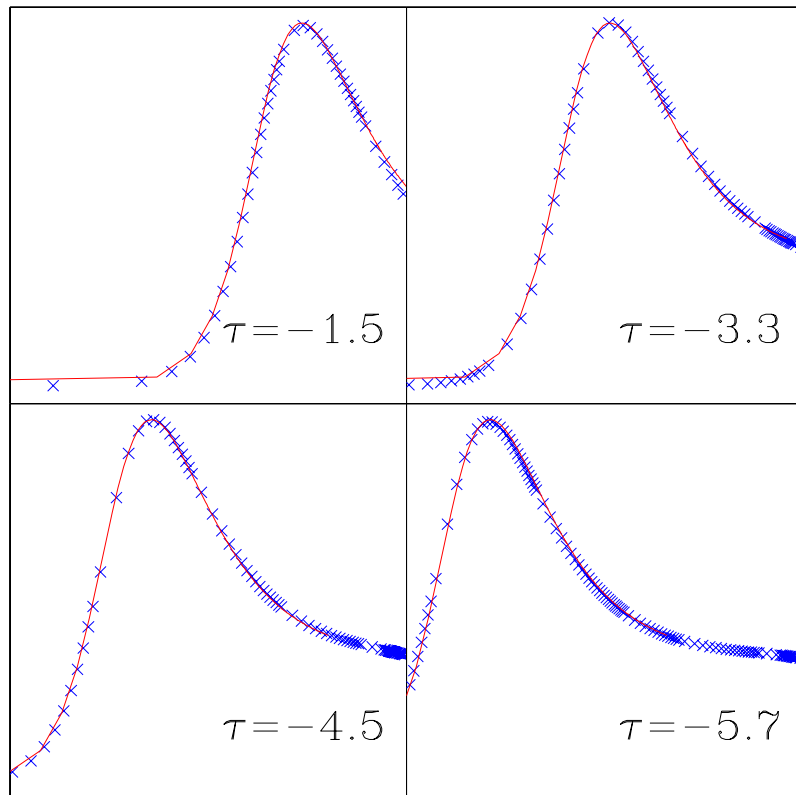
Figure 3.3: Demonstration of equivalence between the CSS solution obtained from [2] and our critical solution obtained with $\lambda = 8$. The solid line shows the metric function $a(r,t)$ versus $\ln r$ provided by Eardley. The crosses denote data points from our solution. Four time profiles are shown with $\tau = \ln(T - T^*)$, where T is the central proper time of the slice and T^* is the critical time of collapse. The Eardley and Hirschmann solution is scaled to match our profile at $\tau = -3.3$. The congruence at other times displays the equivalence of the two solutions.
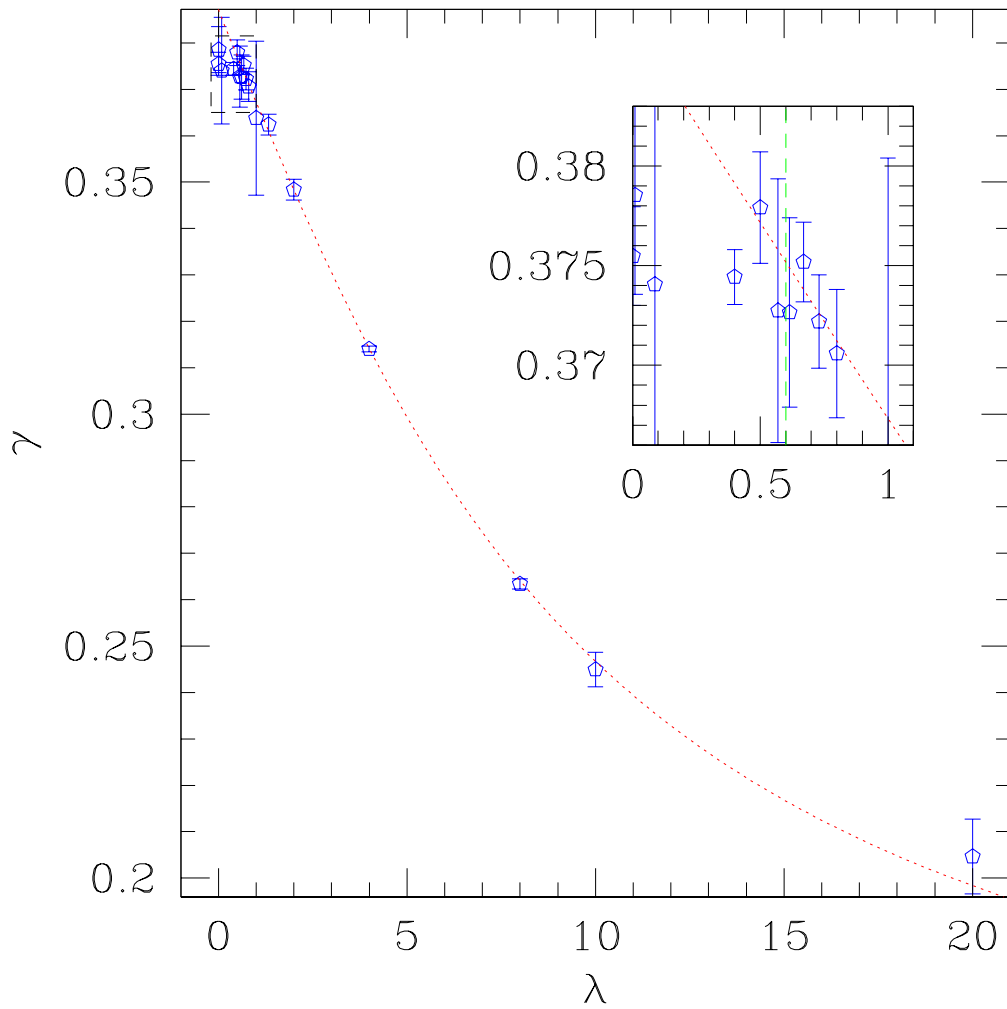
Figure 3.4: Black hole mass scaling exponents for various λ. The dotted line displays the values obtained for the non-linear sigma model in [4]. The open pentagons represent the scaling exponent obtained by least-squares fits using our numerical results. The errorbars represent a range of three standard deviations.
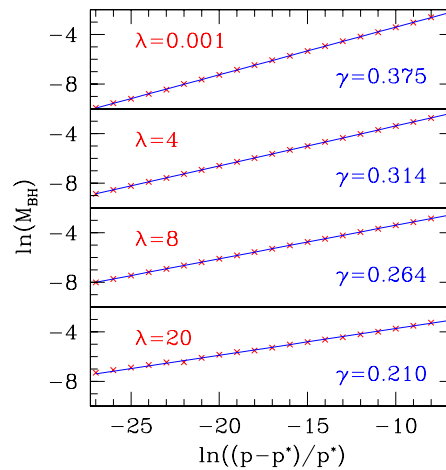
Figure 3.5: Illustration of the power-law mass scaling relation. The markers display the mass obtained for the normalized distance from criticality. The lines designate the least-squares fit line with slope γ.

Table 3.1: Mass scaling exponents γ and the spatial scaling exponents Δ for the various discretely self-similar solutions found.

λ	ω	γ	Δ
0.001	1000	0.375	
0.01	100	0.379	
0.087	10	0.374	
0.4	1.0	0.374	
0.5	0.5	0.378	
0.57	0.25	0.373	3.447
0.615	0.125	0.373	
0.67	0.0	0.375	3.447
0.73	-0.125	0.372	
0.8	-0.25	0.371	
1.0	-0.50	0.364	
1.33	-0.75	0.362	
2.0	-1.00	0.348	
4.0	-1.25	0.314	
8.0	-1.375	0.263	
10	-1.40	0.245	
20	-1.45	0.205	

Chapter 4

Example of a Stability Analysis

The study of critical phenomena lends itself to the study of stability of various solutions. In this chapter, I review work done with Choptuik and Hirschmann in which the stability of a reported soliton is studied [26].

4.1   Introduction

Recently van Putten has proposed a one parameter family (parameter ϵ) of solutions to spherically symmetric Brans-Dicke theory for use in numerical relativity as an approximate black hole [70]. These solutions have the attractive property that for small values of this parameter, the "exterior" solution approaches that of Schwarzschild. However, the event horizon of Schwarzschild is replaced with a high red-shift horizon and all metric components remain finite at this horizon. In addition to regularizing the horizon, these solutions have a global timelike coordinate.

As van Putten stresses, these solutions could have promise for numerical relativity because of the difficulties that arise when dealing numerically with boundary conditions at the horizon of a black hole. To be useful as approximate black holes, however, the solutions, like Schwarzschild, must be stable.

Here we recompute the solutions considered by van Putten and carry out a linear perturbation analysis about them. In so doing, we find, for generic ϵ, modes which grow exponentially in time. We also directly evolve perturbations on the background of these solutions and confirm the instability predicted by linear theory. Thus although of some theoretical interest, these solutions are unlikely to be of direct use in the context of mocking-up a black hole in general relativity.

4.2   The Static Solution

To begin, let us review the static family of solutions considered by van Putten. We note that they were first written down by Brans and Dicke[14] but in an isotropic coordinate system

as opposed to the Schwarzschild-like coordinates that van Putten uses.

We work in Brans-Dicke theory and assume spherical symmetry. Following van Putten, we choose a coordinate system such that the metric has the form

$$ds^2 = -e^{\nu(r,t)}dt^2 + e^{\lambda(r,t)}dr^2 + r^2 d\Omega^2. \tag{4.1}$$

Using $\phi(r,t)$ for the Brans-Dicke field, the field equations are [14]

$$G_{\mu\nu} = \frac{8\pi}{\phi}T_{\mu\nu}, \tag{4.2}$$

where, in vacuum, the Brans-Dicke stress tensor is given by

$$\begin{aligned}
T_{\mu\nu} &= \frac{\omega}{8\pi\phi}\left(\phi_{,\mu}\phi_{,\nu} - \frac{1}{2}g_{\mu\nu}\phi_{,\rho}\phi^{,\rho}\right) \\
&+ \frac{1}{8\pi}\left(\phi_{;\mu\nu} - g_{\mu\nu}\Box\phi\right),
\end{aligned} \tag{4.3}$$

and ω is the Brans-Dicke coupling constant [91]. The field ϕ satisfies the covariant wave equation [91]

$$\Box\phi = \frac{8\pi}{2\omega + 3}T^{\text{matter}} = 0. \tag{4.4}$$

This equation, along with van Putten's restriction to $\omega = 0$, simplifies Eq. (4.3) to $T_{\mu\nu} = \phi_{;\mu\nu}/8\pi$. As the stress tensor is traceless, the field equations may then be written in the simple form

$$R_{\mu\nu} = \frac{\phi_{;\mu\nu}}{\phi}, \tag{4.5}$$

where $R_{\mu\nu}$ is the usual Ricci curvature tensor.

We introduce a new field $\psi(r,t)$ such that

$$e^{\psi(r,t)} = \frac{A}{r\phi(r,t)}, \tag{4.6}$$

where A is a constant [43]. The field equations are

$$\begin{aligned}
\frac{\dot{\lambda}}{r} + \dot{\psi}' &= (\dot{\psi} + \frac{\dot{\lambda}}{2})(\frac{1}{r} + \psi') + \frac{1}{2}\nu'\dot{\psi} \\
-\frac{e^{\lambda}}{r} &= \psi' + \frac{1}{2}(\lambda' - \nu') \\
\left[e^{\frac{1}{2}(\lambda-\nu)-\psi}r\dot{\psi}\right]^{\cdot} &= \left[e^{\frac{1}{2}(\nu-\lambda)-\psi}(1 + r\psi')\right]' \\
e^{\lambda-\nu}(2\ddot{\psi} - \dot{\psi}(2\dot{\psi} + \dot{\nu})) &= (\frac{1}{r} + \psi')(\nu' + \frac{2}{r}) - \frac{1}{r}(\lambda' + \nu'),
\end{aligned} \tag{4.7}$$

where overdots and primes denote derivatives with respect to t and r, respectively. The first three equations above correspond to the tr and $\theta\theta$ components of Eq. (4.5), and the wave equation, respectively. The final equation is a convenient linear combination of the tt and rr components of Eq. (4.5), and the wave equation.

To find the time-independent solutions as van Putten does, all time derivatives appearing in Eqs. (4.7) are set to zero, yielding

$$\psi' + \frac{1}{2}(\lambda' - \nu') = \frac{-e^\lambda}{r} \qquad \psi' = \frac{1}{r}(2Z - 1)$$

$$\lambda' + \nu' = 2Z(\frac{2}{r} + \nu'), \tag{4.8}$$

where $Z \equiv \frac{1}{2}e^{\psi + \frac{1}{2}(\lambda - \nu)}$ and is identical to that defined by van Putten [70]. Details regarding the solution of this system of equations can be found in [70]; here we will only quote the results. The metric components are

$$e^\lambda = 1 - 4Z + \frac{1}{\epsilon}Z(1 - Z) \equiv \frac{1}{\epsilon}(Z_1 + Z)(Z_2 - Z)$$

$$e^\nu = \left[\frac{1 - \frac{Z}{Z_2}}{1 + \frac{Z}{Z_1}} \right]^{\frac{1}{Z_1 + Z_2}},$$

where ϵ is an integration constant, and the constants Z_1 and Z_2 are given by

$$Z_1 = 2\epsilon - \frac{1}{2} + \frac{1}{2}\sqrt{1 - 4\epsilon + 16\epsilon^2}$$

$$Z_2 = -2\epsilon + \frac{1}{2} + \frac{1}{2}\sqrt{1 - 4\epsilon + 16\epsilon^2}. \tag{4.9}$$

The field Z is found from the transcendental equation

$$\frac{|Z|^{Z_1 + Z_2}}{|Z_2 - Z|^{Z_1}|Z + Z_1|^{Z_2}} = r^{-(Z_1 + Z_2)}. \tag{4.10}$$

Note that the field ψ can be recovered once Z, λ, and ν are known.

As van Putten points out, Eq. (4.10) has four solutions, only one of which is Schwarzschild-like in its exterior (van Putten's type Ia [70]). For this solution we have $\epsilon > 0$ and $Z \to Z_2$ as $r \to 0$ while $Z \to 0$ as $r \to \infty$.

It is worthwhile to consider the small r behavior of these fields. In terms of the integration constant ϵ, this behavior is found to be

$$e^\lambda \approx \frac{Z_2^2}{\epsilon} \left(\frac{Z_2}{Z_1 + Z_2} \right)^{\frac{Z_2}{Z_1} - 1} r^{\frac{Z_2}{\epsilon}(Z_1 + Z_2)}$$

$$e^\nu \approx \left(\frac{Z_2}{Z_1 + Z_2} \right)^{\frac{Z_2}{Z_1}\frac{1}{Z_1 + Z_2}} \left(\frac{Z_1}{Z_1 + Z_2} \right)^{\frac{1}{Z_1 + Z_2}} r^{\frac{Z_2}{\epsilon}}. \tag{4.11}$$

If in addition to small r, we consider the limit of small ϵ, these expressions reduce to

$$e^\lambda \approx \frac{1}{e\epsilon}r^{1/\epsilon - 5} \qquad e^\nu \approx \frac{\epsilon}{e}r^{1/\epsilon - 3}. \tag{4.12}$$

Fig. 4.1 displays the solution to Eqs. (4.8) subject to the initial conditions derived from (4.11) for $\epsilon = 1/100$ (the same value shown in [70]).
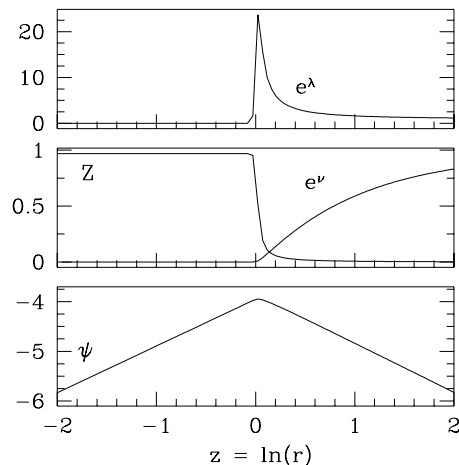
Figure 4.1: Unperturbed fields for $\epsilon = 0.01$. As $\epsilon \to 0$, the field Z approaches a step-function (see Fig. 4.3) and the field e^λ becomes more sharply peaked. This value of ϵ is chosen to correspond with Fig. 2 of [1].

4.3 Perturbation Analysis

Having constructed these static solutions, we can now address the question of their stability. For a given ϵ, such a time-independent solution used in numerical relativity as an approximate black hole, were it not stable, would either collapse to a black hole or possibly disperse leaving flat space.

To investigate stability, we perform a standard linear perturbation analysis. As such, we consider the case that the fields *do* possess a small time dependent part and make the following expansion for small δ

$$
\begin{aligned}
\psi &\rightarrow \psi_0(r) + \delta\,\psi_1(r,t) \\
\nu &\rightarrow \nu_0(r) + \delta\,\nu_1(r,t) \\
\lambda &\rightarrow \lambda_0(r) + \delta\,\lambda_1(r,t),
\end{aligned}
\tag{4.13}
$$

where subscripts 0 and 1 denote the unperturbed and perturbed fields, respectively.

We substitute the expansion (4.13) into the full set of Eqs. (4.7), keeping only terms to linear order. Because the unperturbed fields satisfy (4.7) by construction, we are left with the following linear equations for $(\psi_1,\,\nu_1,\,\lambda_1)$

$$
\begin{aligned}
\frac{\dot{\lambda}_1}{r} &= (\dot{\psi}_1 + \frac{\dot{\lambda}_1}{2})(\frac{1}{r} + \psi_0') - \dot{\psi}_1{}' + \frac{1}{2}\nu_0'\dot{\psi}_1 \\
-\frac{e^{\lambda_0}}{r}\lambda_1 &= \psi_1' + \frac{1}{2}(\lambda_1' - \nu_1')
\end{aligned}
\tag{4.14}
$$
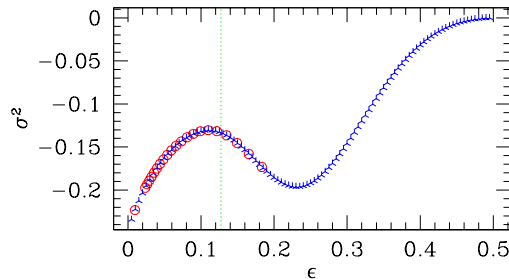
Figure 4.2: Plot of the unstable eigenvalues σ^2 versus parameter ϵ. The cross-marks and open circles represent data from two independent evaluations of the modes. Their correspondence indicates a quite small uncertainty. The vertical dotted line denotes the value of ϵ for which Figs. 4.4, 4.5, and 4.6 are computed.

$$
\begin{aligned}
0 &= \psi_1'' + (\frac{1}{r} + \psi_0') \left[\frac{1}{2}(\nu_1' - \lambda_1') - \psi_1' \right] \\
&\quad + \psi_1' \left[\frac{1}{2}(\nu_0' - \lambda_0') - \psi_0' + \frac{1}{r} \right] - e^{\lambda_0 - \nu_0} \ddot{\psi}_1 \\
\frac{1}{r}(\lambda_1' + \nu_1') &= (\frac{1}{r} + \psi_0')\nu_1' + \psi_1'(\nu_0' + \frac{2}{r}) - 2e^{\lambda_0 - \nu_0} \ddot{\psi}_1 .
\end{aligned}
$$

We perform the standard Fourier decomposition of $\psi_1(t, r)$

$$
\hat{\psi}_1(r, \sigma) = \int e^{i\sigma t} \psi_1(r, t) dt \tag{4.15}
$$

and the other perturbed fields. On substitution into (4.14), the defining relation for $\hat{\psi}_1$ then decouples from $\hat{\lambda}_1$ and $\hat{\nu}_1$, yielding a single equation

$$
\begin{aligned}
0 &= \hat{\psi}_1'' + \hat{\psi}_1' \frac{1}{r} \left[1 + e^{\lambda_0} \frac{3Z_0 - 1}{Z_0 - 1} \right] \\
&\quad + \hat{\psi}_1 \left[\sigma^2 e^{\lambda_0 - \nu_0} - \frac{Z_0}{r(Z_0 - 1)}(\nu_0' + \frac{4Z_0}{r})e^{\lambda_0} \right] \tag{4.16}
\end{aligned}
$$

which can be solved for the mode $\hat{\psi}_1(r)$. We have thus reduced the perturbation problem to a single one-dimensional ODE with the undetermined eigenvalue σ^2.

Solution of Eq. (4.16) requires appropriate boundary conditions on $\hat{\psi}_1(r)$. It is common to enforce regularity at the origin of a spherically symmetric spacetime, but in the current case the unperturbed solution is itself irregular. Thus, assuming regularity of the perturbation might seem improper. However, although ψ_0 is logarithmically divergent at $r = 0$, $\exp(\psi_0)$ is regular at the origin, going to zero as a positive power of r. Hence, it is not unreasonable to impose regularity on the field e^ψ. Further, because $\exp(\psi) = \exp(\psi_0 + \delta\psi_1) = \exp(\psi_0)(1 + \delta\psi_1)$, it is reasonable to assume the regularity of $\hat{\psi}_1$ at the origin. At most, the

41
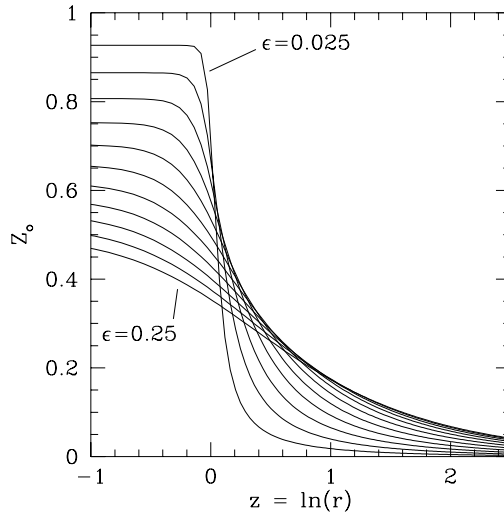
Figure 4.3: The unperturbed field $Z_0(r)$ for $0.025 \leq \epsilon \leq 0.24$ (uniform in ϵ). The field $Z_0(r)$ approaches a step function as ϵ is decreased. The approach of the unperturbed Z_0 to zero at large z signifies the approach to Schwarzschild in that region. For $z < 0$, however, the solution clearly is not Schwarzschild.

mode $\hat{\psi}_1$ could have a logarithmic divergence, however, if we can find an unstable mode with the stricter criterion of regularity, then the solutions are still, in general, unstable.

Enforcing the assumption of regularity of $\hat{\psi}_1$, allows us to find a series expansion for $\hat{\psi}_1$ near the origin. For very small r, Eq. (4.16) becomes

$$0 = \hat{\psi}_1'' + \hat{\psi}_1' \frac{1}{r} + \sigma^2 C \hat{\psi}_1 r^p. \tag{4.17}$$

The positive coefficient C is determined from Eq. (4.11) and depends on ϵ. The exponent $p = \frac{Z_2}{\epsilon}(Z_1 + Z_2 - 1)$ likewise depends only on ϵ and in such a way that $p > -2$ for $\epsilon > 0$. We can now find an expansion for $r \ll 1$

$$\hat{\psi}_1(r) = \hat{\psi}_1(0) \left[1 - \frac{\sigma^2 C}{2+p} r^{2+p} + \left(\frac{\sigma^2 C}{2+p} \right)^2 r^{4+2p} + \dots \right].$$

Because of the linearity of the problem, $\hat{\psi}_1(0)$ can be arbitrarily chosen as it reflects the scaling in the problem. It turns out that we need to use only the first couple of terms in the expansion to get accurate results.

Given a background solution to Eqs. (4.8) for a particular ϵ, we can now solve the eigenvalue problem (4.16) for the modes $\hat{\psi}_1(r)$ and corresponding characteristic frequencies σ^2. In our particular case, the instability of the original soliton solutions is indicated by the existence of one or more exponentially growing modes. These are solutions to the perturbation equations with negative eigenvalues: $\sigma^2 < 0$.

In practice, we integrate the unperturbed equations and the perturbation equation simultaneously from $r \approx 0$ to large r, looking for a solution which has a negative eigenvalue and obeys the boundary conditions. Specifically, we demand that the mode be finite at the origin and vanish asymptotically. We use a standard ODE integrator and standard shooting techniques in our search.

Although our search has not been exhaustive, we generically find precisely one growing mode for each value of ϵ. This is sufficient for us to conclude that the static solutions are unstable. The eigenvalues found for these solutions are shown in Fig. 4.2.

Having found the perturbation modes, looking at the limit $\epsilon \to 0$ is instructive. As this limit is approached, the unperturbed solution becomes more and more like Schwarzschild in the exterior, and this resemblance is precisely the reason why the family has been proposed as a good model of a black hole. With this in mind, one may wonder why Fig. 4.2 shows that, as $\epsilon \to 0$, there is still a growing mode. Certainly these results do not show Schwarzschild to be unstable; rather we point out that within the "effective horizon" of this approximate black hole, the solution is very different from the interior Schwarzschild solution for all ϵ (see Fig. 4.3). Hence, it is reasonable to assert that the solution is unstable for any ϵ, including the solution $\epsilon = 0$.

Further, since it is the case that to an outside observer, the $\epsilon = 0$ solution is indistinguishable from that of Schwarzschild, it is logical to assume that any perturbation of the solution will not change the view of this observer. In other words, as $\epsilon \to 0$, any perturbation should have decreasing support outside the "effective horizon" of the approximate black hole. Indeed, we observe this kind of behavior. As one decreases ϵ, the profile of the mode $\hat{\psi}_1$ is seen to approach that of a delta function at the position where the apparent horizon would asymptotically form.

We find additional evidence for instability by evolving the static solutions (with small perturbations added) using the full time-dependent equations of motion [54]. This has the added benefit of providing information concerning the states to which the static solutions evolve when perturbed. To this end, we have adapted a previously developed spherically symmetric code for Brans-Dicke theory [54] which allows us to evolve these solutions. Because the evolutions in [54] are performed in the Einstein conformal frame (as compared to the Brans-Dicke frame in which van Putten works and in which we have worked thus far), we transform the fields used above to the Einstein frame. In this frame, the field equations are equivalent to those for a massless scalar field minimally coupled to gravity.

After recovering the static solutions in the Einstein frame and inputing a transformed solution into the code, we introduce a small ingoing perturbation to the fields at large radius. For generic values of ϵ, we find that van Putten's solution either collapses or disperses after the
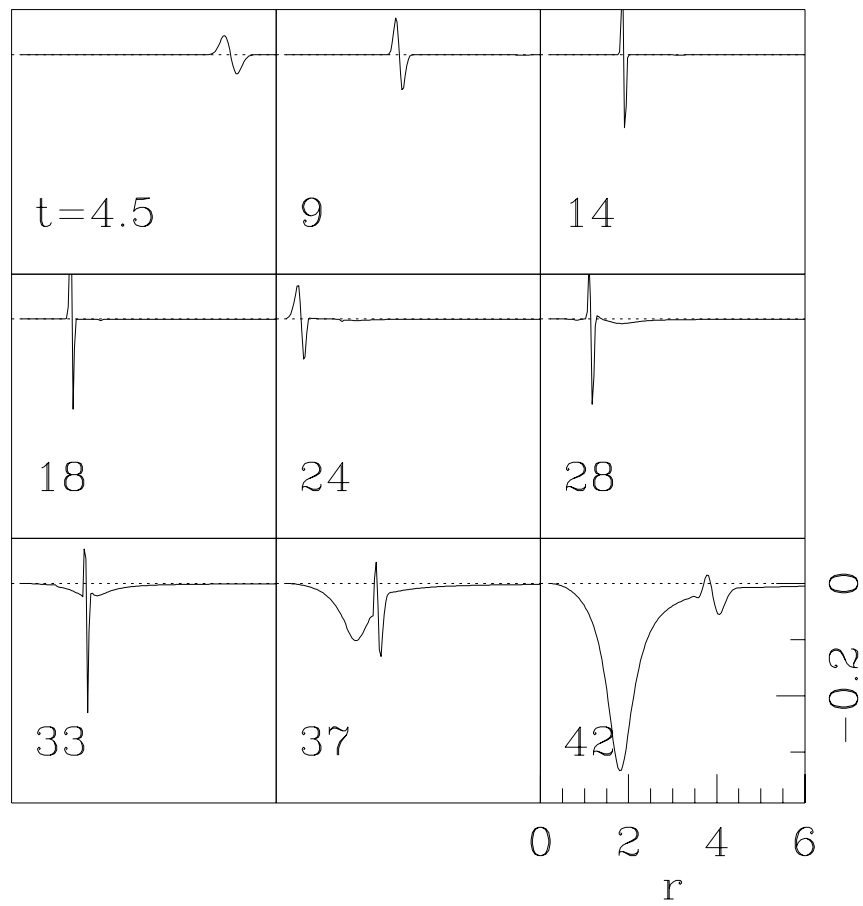
Figure 4.4: Series of snapshots of the product $r\Pi_\xi$ (related to the time derivative of ψ) in the Einstein frame. A small perturbation ($\Delta M/M = 0.018\%$) at large radius is introduced to the initially static solution ($\epsilon = 0.127$). The perturbation passes through the singularity at $r = 0$ (between $t = 24$ and 28) and escapes to $r = \infty$. As the perturbation passes the red-shift horizon (as it propagates inwards, the perturbation is seen to experience a blue-shift), the excitation of a growing mode is clearly seen.
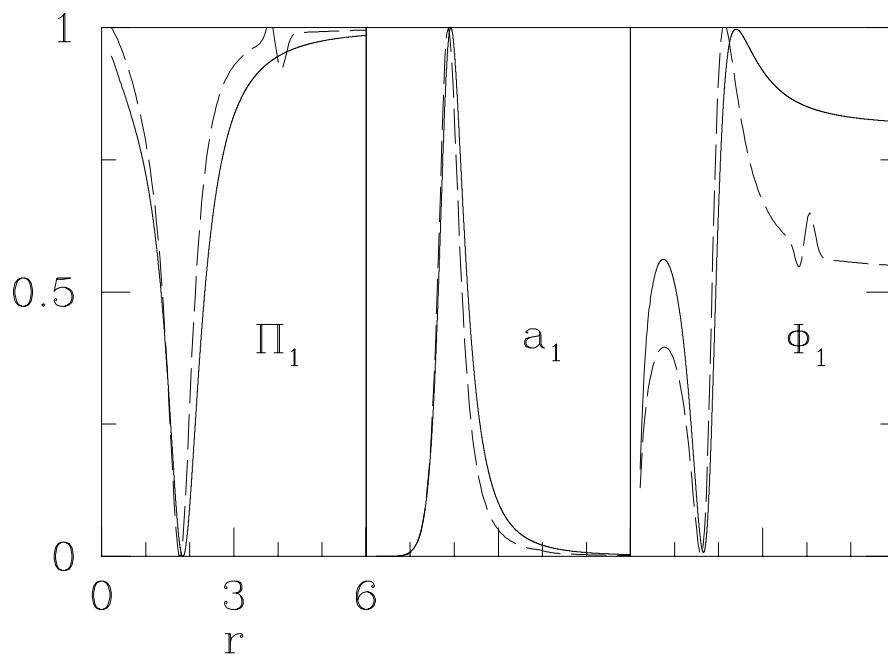
Figure 4.5: Comparison of modes computed in perturbation theory (solid lines) with modes computed from the full non-linear evolution (dashed lines). The non-linear modes were computed by taking a late-time profile from the evolution and subtracting the initial data for that field, as defined in Eq. (4.18). Perturbative modes have been numerically transformed to the Einstein frame. All fields are rescaled to the interval [0..1] and are plotted with respect to r.

perturbation reaches the high-red shift horizon. Fig. 4.4 clearly demonstrates the instability for a specific ϵ. In this case, the perturbation induces collapse to a black hole.

In order to facilitate comparison of the perturbation results with those of the fully nonlinear evolution, we first define the quantities below in terms of the fields found in [54]

$$
\begin{aligned}
\bar{a}_1 &= a(r,t) - a(r,0) \\
\bar{\Phi}_1 &= \Phi_\xi(r,t) - \Phi_\xi(r,0) \\
\bar{\Pi}_1 &= \Pi_\xi(r,t) - \Pi_\xi(r,0)
\end{aligned}
\tag{4.18}
$$

such that fields with a bar and a subscripted 1 denote nonlinear deviations from the unperturbed solution (*nonlinear modes*). By transforming the modes found from linear perturbation theory to the Einstein frame, we may now compare directly the linear modes with the nonlinear modes ($\bar{\Pi}_1$, $\bar{a}_1$, $\bar{\Phi}_1$). In Fig. 4.5 we show all the modes rescaled to the unit interval. From the near congruence, we conclude that we are observing the actual evolution of the growth of these perturbation modes.

4.4 Evidence For Criticality

In addition to confirming our perturbative results, the full evolution provides evidence that these static solutions represent critical solutions to black hole formation. By this we mean that these solutions represent a boundary in the space of solutions between those that form black holes and those that do not. To demonstrate this criticality we begin with an unperturbed solution in the Einstein frame and add a perturbation to the fields. In this case instead of the arbitrary perturbation at large r shown in Fig. 4.4, we add the predicted mode found in the perturbation analysis (solid lines of Fig. 4.5). When this mode is added with some small positive amplitude, we invariably see collapse of the van Putten approximate black hole to a genuine black hole (see the solid lines in Fig. 4.6). In contrast, when the perturbation is added with a small negative amplitude, we see dispersal of the solution (see the dashed lines in Fig. 4.6). Thus it would appear that this solution sits at the threshold between solutions that form black holes and those that disperse. We note that what it means for a solution with a naked singularity at the origin to disperse is perhaps not well defined at the moment. However, the evolution clearly indicates that the energy content is moving toward large radius.

Having found evidence that these are threshold solutions, we are led to ask if they are attracting. For them to represent attracting critical solutions (intermediate attractors) the unstable (relevant) mode which we find must be shown to be unique [53]. Because both the perturbation analysis and the full evolution appear to indicate the presence of only a single unstable mode (see Fig. 4.5), we suspect that these solutions might well represent an intermediate attractor for black hole formation. We plan to address this issue in future work.
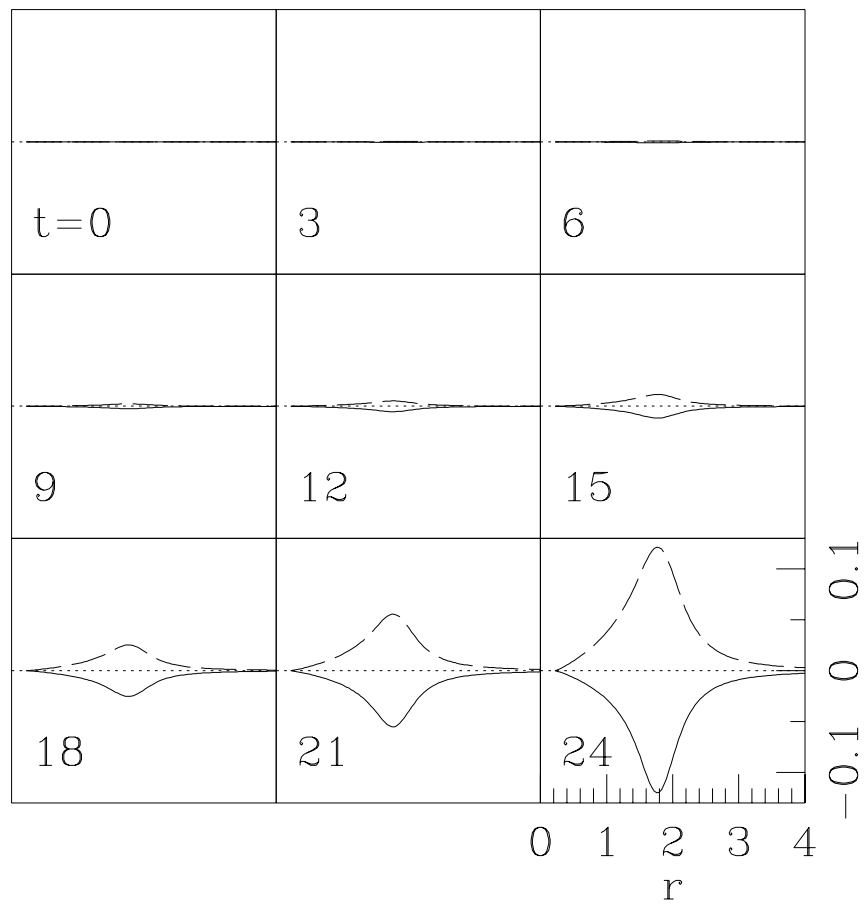
Figure 4.6: Uniform-in-time series of solution when initially perturbed with the predicted mode ($\Delta M/M = 0.004\%$, $\epsilon = 0.127$). Shown here is the field Π_ξ (related to the time derivative of ψ). The evolution shown in solid results in collapse to a black hole. The dashed line shows the evolution resulting from switching the sign of the perturbation at the initial time. That the initial sign of the introduced perturbation separates eventual collapse from dispersal indicates that the unperturbed solution is critical.

From the results presented here, these solutions would appear to be analogous to the $n = 1$ Bartnik-McKinnon (BM) solution in the Einstein-Yang-Mills (EYM) system [7]. This static solution was found to be an intermediate attractor in the gravitational collapse of spherically symmetric $SU(2)$ fields with one side of the threshold being black hole formation and the other dispersion of the Yang-Mills field [24].

After completion of this work, we became aware of other work which had considered solutions similar to those examined here. Static, spherically symmetric solutions to the minimally coupled Einstein-Klein-Gordon equations were studied by Buchdahl[16] and later by Wyman[94]. These solutions were written down in the Einstein frame in contrast to van Putten who works in vacuum Brans-Dicke (which is conformally equivalent to the Einstein-Klein-Gordon system). In addition, Jetzer and Scialom were able to show that Wyman's solutions are generically unstable by establishing the existence of a negative upper bound for the lowest eigenvalue of the perturbation[51]. Yet another paper which discusses the static solutions of Einstein-Klein-Gordon is [50].

Chapter 5

The Harmonic Map

The harmonic map model generalizes and extends the Brans-Dicke model studied in Chapters 3 and 4. Defined in terms of a complex scalar field, $F(r,t)$, the harmonic map represents a mapping from $\mathbb{R}^3$ to a hyperbolic space of constant curvature $-\kappa$. For $\kappa = 0$, the space has zero curvature and the scalar field is just a mapping into the complex plane. For $\kappa > 0$, the internal space is a hyperboloid, while for $\kappa < 0$, the field is a map $\mathbb{R}^3 \to S^2$. It is in the region $\kappa > 0$, that the harmonic model is equivalent to the Brans-Dicke model (see Section 5.2).

5.1   Equations of Motion

The action S for the model under study here is

$$S = \int d^4 x \sqrt{-g} \left(R - \frac{2|\nabla F|^2}{(1 - \kappa |F|^2)^2} \right), \tag{5.1}$$

defined in terms of a complex scalar field $F(r,t)$

$$F(r,t) = \psi(r,t) + i\phi(r,t), \tag{5.2}$$

its complex conjugate $F^*(r,t)$, and a dimensionless parameter κ. The operator ∇ represents the covariant derivative. The action (5.1) is invariant with respect to global rotations of the scalar field

$$F \to e^{i\theta} F \tag{5.3}$$

for constant angle θ, and thus has a conserved current

$$j_\mu = \frac{i\left(F F^*{}_{,\mu} - F^* F_{,\mu}\right)}{(1 - \kappa |F|^2)^2}. \tag{5.4}$$

The conserved charge is then

$$Q = \int j^t \sqrt{-g}\, d^3 x$$
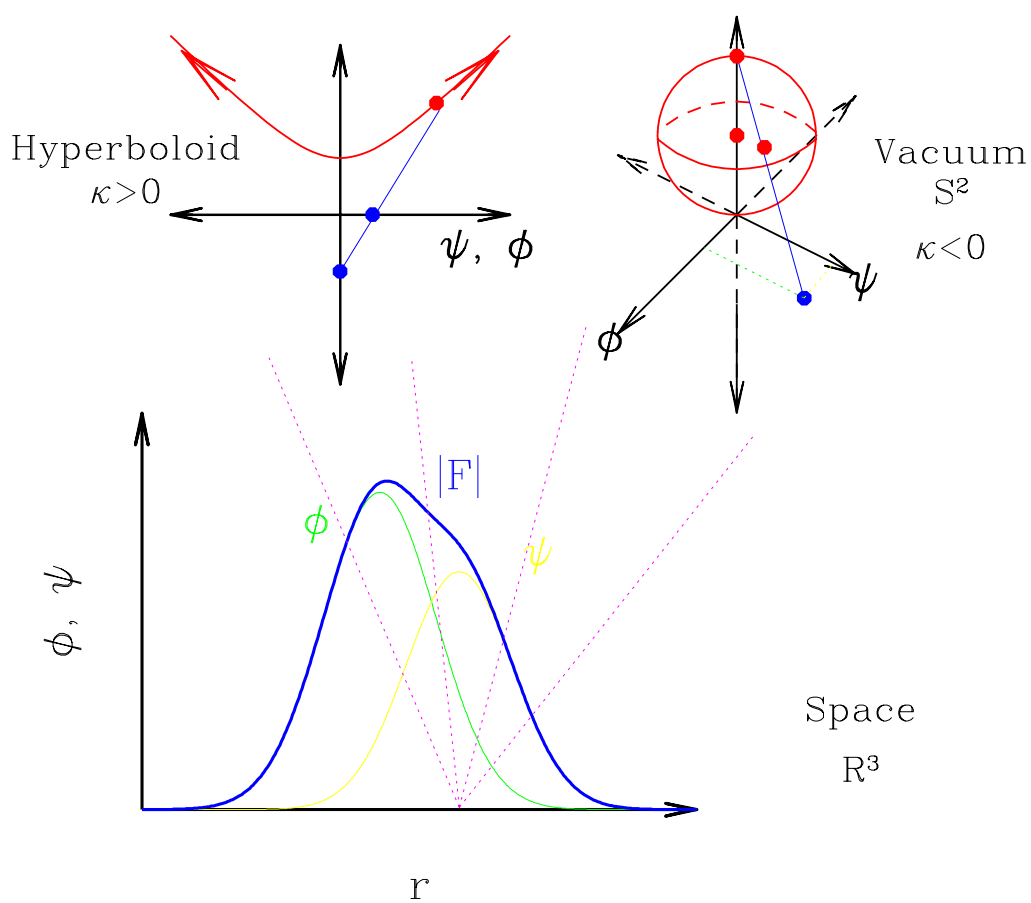
Figure 5.1: Schematic of the harmonic map model as a map from real space to an internal space. The fields ϕ and ψ are defined on the real space domain r. However, these fields themselves represent coordinates on an internal space. For $\kappa < 0$, they are stereographic coordinates of the sphere.

$$
\begin{aligned}
&= \int \frac{i\left[FF^*{}_{,t} - F^*F_{,t}\right]}{\left(1 - \kappa|F|^2\right)^2} \left(\frac{-1}{\alpha^2}\right) \left(\alpha a r^2\right) dr \\
&= \int \frac{-i\left[FF^*{}_{,t} - F^*F_{,t}\right]}{\left(1 - \kappa|F|^2\right)^2} \frac{a}{\alpha} r^2 dr \\
&= \int \frac{2\left[F_2 F_{1,t} - F_1 F_{2,t}\right]}{\left(1 - \kappa|F|^2\right)^2} \frac{a}{\alpha} r^2 dr \\
&= \int \frac{2\left[\phi_2 \Pi_1 - \phi_1 \Pi_2\right]}{\left(1 - \kappa|F|^2\right)^2} \frac{\alpha}{a} \frac{a}{\alpha} r^2 dr \\
&= \int \frac{2\left[\phi_2 \Pi_1 - \phi_1 \Pi_2\right]}{\left(1 - \kappa|F|^2\right)^2} r^2 dr.
\end{aligned}
\tag{5.5}
$$

In component form where Latin indices run over 1 and 2 for the real and imaginary components, this current is

$$
j_\mu = \frac{2}{\left(1 - \kappa|F|^2\right)^2} \epsilon_{ab} F^a F^b{}_{,\mu}.
\tag{5.6}
$$

The field equations are then

$$
G_{\mu\nu} = 8\pi T_{\mu\nu}
\tag{5.7}
$$

$$
\Box F = \frac{-2\kappa F^*}{1 - \kappa|F|^2} F_{;\mu} F^{;\mu}
\tag{5.8}
$$

where $G_{\mu\nu}$ is the usual Einstein tensor and the stress energy takes the form

$$
T_{\mu\nu} = \frac{\psi_{,\mu}\psi_{,\nu} + \phi_{,\mu}\phi_{,\nu} - \frac{1}{2}g_{\mu\nu}\left(\psi_{,\rho}\psi^{,\rho} + \phi_{,\rho}\phi^{,\rho}\right)}{4\pi(1 - \kappa\left(\psi^2 + \phi^2\right))^2}.
\tag{5.9}
$$

In terms of the real and imaginary parts of F, the wave equation becomes

$$
\begin{aligned}
\Box\psi &= -\frac{2\kappa\left[\psi\psi_{,\mu}\psi^{,\mu} - \psi\phi_{,\mu}\phi^{,\mu} + 2\phi\psi_{,\mu}\phi^{,\mu}\right]}{1 - \kappa\left(\psi^2 + \phi^2\right)} \\
\Box\phi &= -\frac{2\kappa\left[\phi\phi_{,\mu}\phi^{,\mu} - \phi\psi_{,\mu}\psi^{,\mu} + 2\psi\psi_{,\mu}\phi^{,\mu}\right]}{1 - \kappa\left(\psi^2 + \phi^2\right)}.
\end{aligned}
\tag{5.10}
$$

We work in spherically symmetry with the metric

$$
ds^2 = -\alpha^2(r,t)dt^2 + a^2(r,t)dr^2 + r^2 d\Omega^2.
\tag{5.11}
$$

As before, we introduce the following auxiliary variables in order to cast the field equations in first order in time form

$$
\begin{aligned}
\Pi_\psi &\equiv \frac{a}{\alpha}\dot\psi & \Phi_\psi &\equiv \psi' \\
\Pi_\phi &\equiv \frac{a}{\alpha}\dot\phi & \Phi_\phi &\equiv \phi',
\end{aligned}
\tag{5.12}
$$

where overdots and primes denote derivatives with respect to t and r, respectively. The two second order wave equations become four, first order equations

$$\dot{\Pi}_\psi = r^{-2} \left(\frac{r^2 \alpha}{a} \Phi_\psi \right)' \tag{5.13}$$

$$+ \frac{2\alpha\kappa \left[\psi \left(\Phi_\psi^2 - \Pi_\psi^2 - \Phi_\phi^2 + \Pi_\phi^2 \right) + 2\phi \left(\Phi_\psi \Phi_\phi - \Pi_\psi \Pi_\phi \right) \right]}{a \left(1 - \kappa \left(\psi^2 + \phi^2 \right) \right)}$$

$$\dot{\Phi}_\psi = \left(\frac{\alpha}{a} \Pi_\psi \right)' \tag{5.14}$$

$$\dot{\Pi}_\phi = r^{-2} \left(\frac{r^2 \alpha}{a} \Phi_\phi \right)' \tag{5.15}$$

$$+ \frac{2\alpha\kappa \left[\phi \left(\Phi_\phi^2 - \Pi_\phi^2 - \Phi_\psi^2 + \Pi_\psi^2 \right) + 2\psi \left(\Phi_\phi \Phi_\psi - \Pi_\phi \Pi_\psi \right) \right]}{a \left(1 - \kappa \left(\psi^2 + \phi^2 \right) \right)}$$

$$\dot{\Phi}_\phi = \left(\frac{\alpha}{a} \Pi_\phi \right)'. \tag{5.16}$$

The fields ψ and ϕ are maintained at each time step by spatially integrating their respective spatial derivatives

$$\psi(r, t) = \int_0^r \Phi_\psi(\tilde{r}, t) \, d\tilde{r} \tag{5.17}$$

$$\phi(r, t) = \int_0^r \Phi_\phi(\tilde{r}, t) \, d\tilde{r}. \tag{5.18}$$

From Eq. (2.37) in Section 2.7, the Hamiltonian constraint is

$$\frac{a'}{a} + \frac{a^2 - 1}{2r} = \frac{r \left[\Phi_\psi^2 + \Phi_\phi^2 + \Pi_\psi^2 + \Pi_\phi^2 \right]}{2 (1 - \kappa \left(\psi^2 + \phi^2 \right))^2}, \tag{5.19}$$

and from Eq. (2.30), the lapse function is

$$0 = \frac{\alpha'}{\alpha} - \frac{a'}{a} + \frac{1 - a^2}{r}. \tag{5.20}$$

Finally, from Eq. (2.44), combination of an evolution equation and a momentum constraint yields an evolution equation for a

$$\dot{a} = r\alpha \frac{\Phi_\psi \Pi_\psi + \Phi_\phi \Pi_\phi}{(1 - \kappa \left(\psi^2 + \phi^2 \right))^2}. \tag{5.21}$$

5.2 Equivalence to Other Models

To show the harmonic map's equivalence to the Brans-Dicke model studied in Chapter 3 for $\kappa > 0$, I first show that, for $\kappa = 1$, it is equivalent to the axion-dilaton system studied in [28] with the action

$$L^\tau = \frac{-1}{32\pi} \left(e^{4\Phi} a_{,\mu} a^{,\mu} + 4 \Phi_{,\mu} \Phi^{,\mu} \right), \tag{5.22}$$

where τ is defined in terms of the axion a and dilaton Φ by

$$\tau = a + ie^{-2\Phi}. \tag{5.23}$$

Letting

$$F = \frac{1 + i\tau}{1 - i\tau} \tag{5.24}$$

the Lagrangian for the harmonic map

$$L^{\mathrm{F}} = -\frac{1}{8\pi} \left[1 - \kappa \left(\psi^2 + \phi^2 \right) \right]^{-2} \left(\psi_{,\mu} \psi^{,\mu} + \phi_{,\mu} \phi^{,\mu} \right) \tag{5.25}$$

becomes in terms of the components of $\tau = \tau_1 + i\tau_2$

$$L^{\mathrm{F}}(\tau) = \frac{-1}{2\pi} \frac{\tau_{1,\mu} \tau_1^{,\mu} + \tau_{2,\mu} \tau_2^{,\mu}}{\left(\left(1 + 2\tau_2 + \tau_1^2 + \tau_2^2 \right) - \kappa \left(1 - 2\tau_2 + \tau_1^2 + \tau_2^2 \right) \right)^2}. \tag{5.26}$$

For $\kappa = 1$, this becomes

$$L^{\mathrm{F}}(\tau, \kappa = 1) = \frac{-1}{32\pi} \frac{\tau_{1,\mu} \tau_1^{,\mu} + \tau_{2,\mu} \tau_2^{,\mu}}{\tau_2^2}. \tag{5.27}$$

Because of Equation (5.23), we have the identities

$$a \equiv \tau_1 \qquad \exp(-2\Phi) \equiv \tau_2 \tag{5.28}$$

with which (5.27) becomes the axion-dilaton Lagrangian (5.22).

If we now make the transformation

$$F = \frac{1}{\sqrt{\kappa}} \frac{1 + i\tau}{1 - i\tau}, \tag{5.29}$$

for $\kappa > 0$, the harmonic map Lagrangian (5.25) then becomes

$$L^{\mathrm{F}} = -\frac{\tau_{1,\mu} \tau_1^{,\mu} + \tau_{2,\mu} \tau_2^{,\mu}}{32\pi\kappa\tau_2^2}. \tag{5.30}$$

Letting

$$\tau_1 = a\sqrt{\kappa} \qquad\qquad \tau_2 = e^{-2\Phi} \tag{5.31}$$

$$\lambda = 8\kappa \qquad\qquad \tau = a\sqrt{\kappa} + ie^{-2\Phi} \tag{5.32}$$

the above Lagrangian becomes

$$L^{\mathrm{F}} = -\frac{1}{32\pi} \left(e^{4\Phi} a_{,\mu} a^{,\mu} + \frac{8}{\lambda} 4\Phi_{,\mu} \Phi^{,\mu} \right). \tag{5.33}$$

This is identical to the Brans-Dicke Lagrangian with the trivial rescalings

$$\psi_{\mathrm{BD}} = \left(1/\sqrt{16\pi} \right) a \qquad \xi = -4\Phi. \tag{5.34}$$
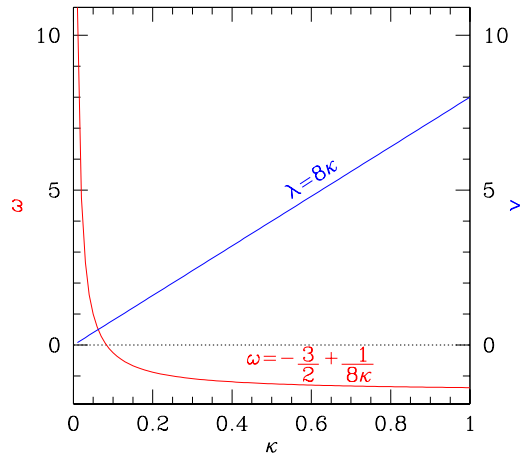
Figure 5.2: Relationship of the Brans-Dicke coupling parameters λ and ω to the harmonic map parameter κ. Note that for $\kappa \leq 0$, the equivalence shown does not hold.

The models are thus equivalent for $\kappa > 0$, where

$$\omega = -\frac{3}{2} + \frac{1}{8\kappa} \qquad \lambda = 8\kappa. \tag{5.35}$$

The relationship between the real and imaginary components of the harmonic map field $(\psi_{\mathrm{HM}}, \phi_{\mathrm{HM}})$ and the Brans-Dicke fields $(\psi_{\mathrm{BD}}, \xi)$ is then

$$\psi_{\mathrm{HM}} = \sqrt{\frac{8}{\lambda}} \left(\frac{1 - \left(2\lambda\pi\psi_{\mathrm{BD}}^2 + e^{\xi}\right)}{1 + \left(2\lambda\pi\psi_{\mathrm{BD}}^2 + e^{\xi}\right) + 2e^{\xi/2}} \right) \tag{5.36}$$

$$\phi_{\mathrm{HM}} = \frac{2\sqrt{16\pi}\psi_{\mathrm{BD}}}{1 + \left(2\lambda\pi\psi_{\mathrm{BD}}^2 + e^{\xi}\right) + 2e^{\xi/2}}. \tag{5.37}$$

The inversion of this (done with the help of Hirschmann [46] using the auxiliary fields $x = \sqrt{16\pi\kappa}\psi_{bd}$ and $y = 1 + e^{\xi/2}$) is

$$\psi_{\mathrm{BD}} = \frac{\phi_{\mathrm{HM}}}{2\sqrt{\pi} \left[\left(\sqrt{\kappa}\psi_{\mathrm{HM}} + 1\right)^2 + \kappa\phi_{\mathrm{HM}}^2 \right]} \tag{5.38}$$

$$\xi = 2\ln \left[\frac{2\left(\sqrt{\kappa}\psi_{\mathrm{HM}} + 1\right)}{\left(\sqrt{\kappa}\psi_{\mathrm{HM}} + 1\right)^2 + \kappa\phi_{\mathrm{HM}}^2} - 1 \right]. \tag{5.39}$$

5.3 Extra Charges

The very geometric nature of the harmonic map motivates one to look at conserved symmetries. The usual Noether charge associated with the global $U(1)$ symmetry of the harmonic

map action has already been computed in Equation (5.5). However, for $\kappa = 0$ the Lagrangian is also invariant under translation in the complex target space

$$F \rightarrow F + c$$

for some complex c. In the notation of Ryder [75], we have

$$\Delta x = 0 \qquad \Delta \phi = c \qquad \Delta \phi^* = c^*$$

$$\Phi = c \qquad \Phi^* = c^*$$

The associated current is then (Ryder's equation (3.25))

$$
\begin{aligned}
J^\mu &= \frac{\partial L}{\partial (\partial_\mu \phi)} (\Phi) + \frac{\partial L}{\partial (\partial_\mu \phi^*)} (\Phi*) \\
&= \frac{\partial L}{\partial (\partial_\mu \phi)} (c) + \frac{\partial L}{\partial (\partial_\mu \phi^*)} (c^*) \\
&= F^{*,\mu} c + F^{,\mu} c^*
\end{aligned}
$$

and the charge is then

$$
\begin{aligned}
Q &= \int_r r^2 \, dr \, \left(J^0 \right) \\
&= \int_r r^2 \, dr \, \left(\dot{F}^* c + \dot{F} c^* \right)
\end{aligned}
$$

which for c real gives

$$Q = \int_r r^2 \, dr \, \dot{F}_1$$

conserved. For c imaginary gives

$$Q = \int_r r^2 \, dr \, \dot{F}_2.$$

Taking the divergence of this current density

$$J^\mu{}_{;\mu} = c \Box \phi^* + c^* \Box \phi,$$

confirms that the equations of motion conserve the charge.

Hirschmann has generalized these charges for any κ [46]. In the harmonic map, analogous to pure translations in the complex plane, the model is invariant with respect to translations of the origin of the internal space. For example, when the target space is the sphere, this translation just simply rotates the image of the map on the sphere effectively picking a new origin. The placement of the origin should have no bearing on the model, and hence the model is invariant with respect to these changes.

The killing vectors associated with this symmetry, which satisfy $\nabla_a \xi_b + \nabla_b \xi_a = 0$, are

$$\begin{aligned}
\xi^\theta &= A \sin\phi - B \cos\phi \\
\xi^\phi &= \cot\left(A \cos\phi + B \sin\phi\right) - C,
\end{aligned}$$

where $\theta = 2\psi$. The fields θ and ψ are, here, angles on the hyperbolic space defined by

$$\psi = 2\tan^{-1}\left[\sqrt{|\kappa|\left(F_1^2 + F_2^2\right)}\right] \tag{5.40}$$

$$\phi = \tan^{-1}\frac{F_2}{F_1}, \tag{5.41}$$

where $F = F_1 + iF_2$. Transforming back into Cartesian coordinates in the plane ($x = F^1$ and $y = F^2$), the killing vector is

$$\begin{aligned}
\xi^x &= \frac{A|\kappa|xy - \frac{B}{2}\left(1 + |\kappa|\left(x^2 - y^2\right)\right) + \sqrt{|\kappa|}Cy}{\sqrt{|\kappa|}\left(1 - \kappa\left(\left(F^1\right)^2 + \left(F^2\right)^2\right)\right)^2} \\
\xi^y &= \frac{-B|\kappa|xy + \frac{A}{2}\left(1 - |\kappa|\left(x^2 - y^2\right)\right) - \sqrt{|\kappa|}Cy}{\sqrt{|\kappa|}\left(1 - \kappa\left(\left(F^1\right)^2 + \left(F^2\right)^2\right)\right)^2}.
\end{aligned}$$

The current can then be computed using the following equation from Misner's article in Tipler's book [65]

$$J_\mu = \xi_a \nabla_\mu F^A. \tag{5.42}$$

The resulting current is then

$$\begin{aligned}
J^\mu = {}& \frac{1}{\sqrt{|\kappa|}\left(1 - \kappa\left(\left(F^1\right)^2 + \left(F^2\right)^2\right)\right)^2} \\
& \left\{\frac{A}{2}\left[2|\kappa|F^1 F^2 \nabla^\mu F^1 + \left(1 - |\kappa|\left(\left(F^1\right)^2 - \left(F^2\right)^2\right)\right)\nabla^\mu F^2\right]\right. \\
& -\frac{B}{2}\left[-2|\kappa|F^1 F^2 \nabla^\mu F^2 + \left(1 + |\kappa|\left(\left(F^1\right)^2 - \left(F^2\right)^2\right)\right)\nabla^\mu F^1\right] \\
& \left. +C\sqrt{|\kappa|}\left[F^2 \nabla^\mu F^1 - F^1 \nabla^\mu F^2\right]\right\}.
\end{aligned}$$

The three charges are

$$\begin{aligned}
Q_3 = {}& -4\pi \int \frac{a}{\alpha\left(1 - \kappa\left(\left(F^1\right)^2 + \left(F^2\right)^2\right)\right)^2} r^2 \, dr \, \frac{A}{2}\left[\vphantom{\frac{A}{2}}\right. \\
& \left. 2|\kappa|F^1 F^2 F^1_{,t} + \left(1 - |\kappa|\left(\left(F^1\right)^2 - \left(F^2\right)^2\right)\right)F^2_{,t}\right] \\
= {}& \int \frac{a}{\alpha\left(1 - \kappa\left(\psi^2 + \phi^2\right)\right)^2} r^2 \, dr \, \left[2|\kappa|\psi\phi\psi_{,t} + \left(1 - |\kappa|\left(\psi^2 - \phi^2\right)\right)\phi_{,t}\right]
\end{aligned}$$

$$
= \int r^2 \, dr \, \frac{2|\kappa|\psi\phi\Pi_\psi + \left(1 - |\kappa| \left(\psi^2 - \phi^2\right)\right)\Pi_\phi}{\left(1 - \kappa \left(\psi^2 + \phi^2\right)\right)^2}
$$

$$
Q_2 = -4\pi \int \frac{a \, r^2 \, dr}{\alpha \left(1 - \kappa \left(\left(F^1\right)^2 + \left(F^2\right)^2\right)\right)^2} \left(\frac{-B}{2}\right) \Bigg[
$$

$$
-2|\kappa|F^1 F^2 F_{,t}^2 + \left(1 + |\kappa| \left(\left(F^1\right)^2 - \left(F^2\right)^2\right)\right) F_{,t}^1 \Bigg]
$$

$$
= \int \frac{a}{\alpha \left(1 - \kappa \left(\psi^2 + \phi^2\right)\right)^2} r^2 \, dr \, \left[-2|\kappa|\psi\phi\phi_{,t} + \left(1 + |\kappa| \left(\psi^2 - \phi^2\right)\right)\psi_{,t}\right]
$$

$$
= \int r^2 \, dr \, \frac{-2|\kappa|\psi\phi\Pi_\phi + \left(1 + |\kappa| \left(\psi^2 - \phi^2\right)\right)\Pi_\psi}{\left(1 - \kappa \left(\psi^2 + \phi^2\right)\right)^2}
$$

$$
Q_1 = -4\pi \int \frac{a}{\alpha \left(1 - \kappa \left(\left(F^1\right)^2 + \left(F^2\right)^2\right)\right)^2} r^2 \, dr \, C\sqrt{|\kappa|} \left[F^2 F_{,t}^1 - F^1 F_{,t}^2\right]
$$

$$
= \int \frac{a}{\alpha \left(1 - \kappa \left(\psi^2 + \phi^2\right)\right)^2} r^2 \, dr \, \left[\phi\psi_{,t} - \psi\phi_{,t}\right]
$$

$$
= \int r^2 \, dr \, \frac{\phi\Pi_\psi - \psi\Pi_\phi}{\left(1 - \kappa \left(\psi^2 + \phi^2\right)\right)^2}.
$$

When $\kappa = 0$, these reduce to the charges found previously for the complex scalar field. Computation of these charges for various evolutions confirm that they are conserved.

5.4 Decomposition Into Magnitude and Phase

Instead of decomposing the scalar field as $F = \psi + i\phi$, we can instead consider a decomposition into a magnitude and phase

$$
F = f e^{ih}. \tag{5.43}
$$

Using the identities

$$
\dot{F} = \left(\dot{f} + i\dot{h}f\right)e^{ih} \qquad\qquad F' = \left(f' + ih'f\right)e^{ih}
$$

$$
\Pi_f = \frac{a}{\alpha}\dot{f} \qquad\qquad \Pi_H = \frac{a}{\alpha}f\dot{h}
$$

$$
\Phi_f = f' \qquad\qquad \Phi_H = fh'
$$

$$
\Pi_F = \left(\Pi_f + i\Pi_H\right)e^{ih} \qquad\qquad \Phi_F = \left(\Phi_f + i\Phi_H\right)e^{ih}
$$

$$
\dot{h} = \frac{\alpha}{af}\Pi_H \qquad\qquad h' = \frac{1}{f}\Phi_H,
$$

the wave equation (5.8)

$$
\dot{\Pi}_F = \frac{1}{r^2}\left(\frac{r^2\alpha}{a}\Phi_F\right)_{,r} + 2\kappa\alpha a\frac{F^* F_{,\mu} F^{,\mu}}{1 - \kappa|F|^2} \tag{5.44}
$$

can be separated into real and imaginary parts

$$
\begin{aligned}
\dot{\Pi}_f - \frac{\alpha}{af}\Pi_H{}^2 &= \frac{1}{r^2}\left(\frac{r^2\alpha}{a}\Phi_f\right)_{,r} \\
&\quad -\frac{\alpha}{af}\Phi_H{}^2 + \frac{2\kappa f\alpha}{a\left(1-\kappa f^2\right)}\left[\Pi_H^2 - \Pi_f^2 + \Phi_f^2 - \Phi_H^2\right] \\
\dot{\Pi}_H + \frac{\alpha}{af}\Pi_H\Pi_f &= \frac{1}{r^2}\left(\frac{r^2\alpha}{a}\Phi_H\right)_{,r} \\
&\quad +\frac{\alpha}{af}\Phi_H\Phi_f + \frac{4\kappa f\alpha}{a\left(1-\kappa f^2\right)}\left[\Phi_f\Phi_H - \Pi_f\Pi_H\right].
\end{aligned}
$$

Grouping terms gets the final form of the equations

$$
\begin{aligned}
\dot{\Pi}_f &= \frac{1}{r^2}\left(\frac{r^2\alpha}{a}\Phi_f\right)_{,r} \\
&\quad +\frac{\alpha}{af}\left[\Pi_H{}^2 - \Phi_H{}^2\right] + \frac{2\kappa f\alpha}{a\left(1-\kappa f^2\right)}\left[\Pi_H^2 - \Pi_f^2 + \Phi_f^2 - \Phi_H^2\right] \qquad (5.45)\\
\dot{\Pi}_H &= \frac{1}{r^2}\left(\frac{r^2\alpha}{a}\Phi_H\right)_{,r} \\
&\quad +\frac{\alpha}{af}\left[\Phi_H\Phi_f - \Pi_H\Pi_f\right] + \frac{4\kappa f\alpha}{a\left(1-\kappa f^2\right)}\left[\Phi_f\Phi_H - \Pi_f\Pi_H\right]. \qquad (5.46)
\end{aligned}
$$

For initial data with zero charge, h' and $\dot{h}$ necessarily vanish and do not grow according to Equation (5.46). This simply confirms that global rotations of initial data with either the real or imaginary component vanishing behave the same in that the charge remains zero throughout the evolution. This decomposition into magnitude and phase as opposed to real and imaginary components seems much better suited for discussion of the behavior of the charge in the harmonic map. Indeed, the issue of charge is further discussed in Chapter 6.6.

5.5 Topological Aspects of the Harmonic Map: Textures

For $\kappa < 0$, the harmonic map model maps to the sphere and is equivalent to the $O(3)$ nonlinear sigma model. This model corresponds to that for a triplet scalar field where the scalar field is restricted to lie on the S^2 vacuum manifold. In other words, take a model for a three-component Higgs field Φ_a $(a = 1, 2, 3)$

$$
\mathcal{L} = \frac{-1}{2}\Phi^a_{,\mu}\Phi^{a,\mu} + \lambda\left(|\Phi|^2 - \frac{1}{|\kappa|}\right)^2 \qquad (5.47)
$$

and let $\lambda \to \infty$. In this case, the effective mass of the scalar field becomes infinite, and only the bosonic degrees of freedom are allowed. In other words, the field configuration would have to pay an infinite cost in terms of energy to leave the sphere. These bosonic degrees of freedom correspond to motion on the sphere, and hence the models are equivalent in this limit (see Ryder [75]).

With this equivalence in hand, we can examine the symmetry properties of the model. First, consider the vacuum states, or zero energy states, of the system. These vacuum states contain all field configurations where the scalar field is independent of time and radius, and hence the states are degenerate. All these states can be represented by points on the sphere because the configuration would have potential energy were it not resident on the sphere. The sphere is then seen as the representation of the vacuum manifold where all states are related by transformations in the group $SO(3)$.

This $SO(3)$ symmetry is then broken once a vacuum state is selected from the vacuum manifold. Once a state is selected, only under rotations about the ray formed between the origin and the point on the sphere is the state invariant. This symmetry is $U(1)$ or $SO(2)$. The model is then said to have a broken symmetry $SO(3)/SO(2)$.

The presence of this broken symmetry indicates that topological defects may be significant in the dynamics of the model. To see which defects are allowed by the model, we look at the various homotopy groups of the vacuum manifold, S^2. Because you cannot shrink a two-sphere over another two-sphere, the second homotopy group is nontrivial, $\pi_2(S^2) \neq I$, and the model admits monopoles. Because the third homotopy group for this vacuum manifold is nontrivial, $\pi_3(S^2) \neq I$, the model admits textures (Vilenkin and Shellard discuss homotopy groups and textures [88]). These particular textures are called Hopf textures.

Textures are unique among topological defects because the fields lie everywhere on the vacuum manifold, are generally unstable to collapse, and are nonsingular. A one dimensional texture is shown in Figure 5.3 where it is compared to a vortex.

While much of the physics literature concerns itself with the simpler textures found in $SO(4)/SO(3)$, some work with Hopf textures has been published [21, 58, 72, 85, 93]. This model is discussed further in Chapter 8. The literature on Hopf textures appears in both a physics and a mathematics context with the quandary that the physics literature is generally vague and the mathematical literature too complex [20, 80, 81, 87].

One issue that is somewhat complex is the issue of charge. With monopoles and $SO(4)/SO(3)$ textures, for example, an explicit topological charge density can be calculated locally which can then be integrated over space to obtain the conserved charge of the space-time. In the case of the Hopf texture, the situation is much more complicated, as the charge is computed by global means and lacks a local charge density.

Consider a map from compactified space, $\boldsymbol{R}^3 \cup \{\infty\} \cong S^3$, to the vacuum manifold, S^2. Now consider the pre-image of some point in the vacuum space. This pre-image is necessarily a topological circle (some closed curve) in space. Now take the pre-image of some other point on S^2. With these two pre-images, one now has two loops in real space. The Hopf

index (or charge) is then simply the linking number of these pre-images. This calculation is shown schematically in Figure 5.4.

As mentioned previously, the texture is unstable to collapse, and hence during collapse, the linking number should eventually become zero. However, for these two pre-images to become unlinked would require them to cross at some point. This implies that the pre-images of the two distinct points in the vacuum space would be the same at some instant, and therefore that the map becomes singular. Hopf texture collapse is further examined in Chapter 8.

The literature contains mention of partial Hopf textures with non-integer charge. These partial textures appear possible only when non-uniform behavior of the fields at infinity is allowed [72]. In such a situation, the pre-images of points in the vacuum space are not necessarily topological circles, and the charge can then be non-integer [76].

As an example, consider the charge of a toroidally symmetric texture described in Chapter 8 and found in [58]. Here, I show explicitly that the Hopf charge is unity. The initial data takes the form

$$\Phi(\vec{x}) = \frac{1}{\sqrt{\kappa}} \begin{pmatrix} \cos\left(2\pi a \frac{\sqrt{x^2+y^2}}{r^2+a^2}\right) \\ \sin\left(2\pi a \frac{\sqrt{x^2+y^2}}{r^2+a^2}\right) \frac{(r^2-a^2)x+2azy}{\sqrt{((r^2-a^2)^2+4a^2z^2)(x^2+y^2)}} \\ \sin\left(2\pi a \frac{\sqrt{x^2+y^2}}{r^2+a^2}\right) \frac{-(r^2-a^2)y+2azx}{\sqrt{((r^2-a^2)^2+4a^2z^2)(x^2+y^2)}} \end{pmatrix} \tag{5.48}$$

where a is the radius of the degenerate torus.

This data maps to the sphere centered at the orgin with radius $1/\sqrt{|\kappa|}$. We pick two polar points on the sphere

$$\Phi(\vec{x}) = \frac{1}{\sqrt{\kappa}} \begin{pmatrix} \pm 1 \\ 0 \\ 0 \end{pmatrix}, \tag{5.49}$$

and consider their pre-images. Letting $x^2 + y^2 = 0$ in Equation (5.48) shows that the z axis is the pre-image of the point with the positive sign in Equation (5.49).

Letting $a^2 = x^2 + y^2$ and $z = 0$ in Equation (5.48), one can see that the circle in the xy plane with radius a centered at the origin is the pre-image of the point with the negative sign in Equation (5.49).

In the compactified space these are both circles and they have linking number one. Since any two points suffice to calculate the Hopf charge, the charge for the map is unity.

If we now consider finding the charge of configurations in the spherically symmetric harmonic map model in this fashion, we see that the charge of all these configurations are
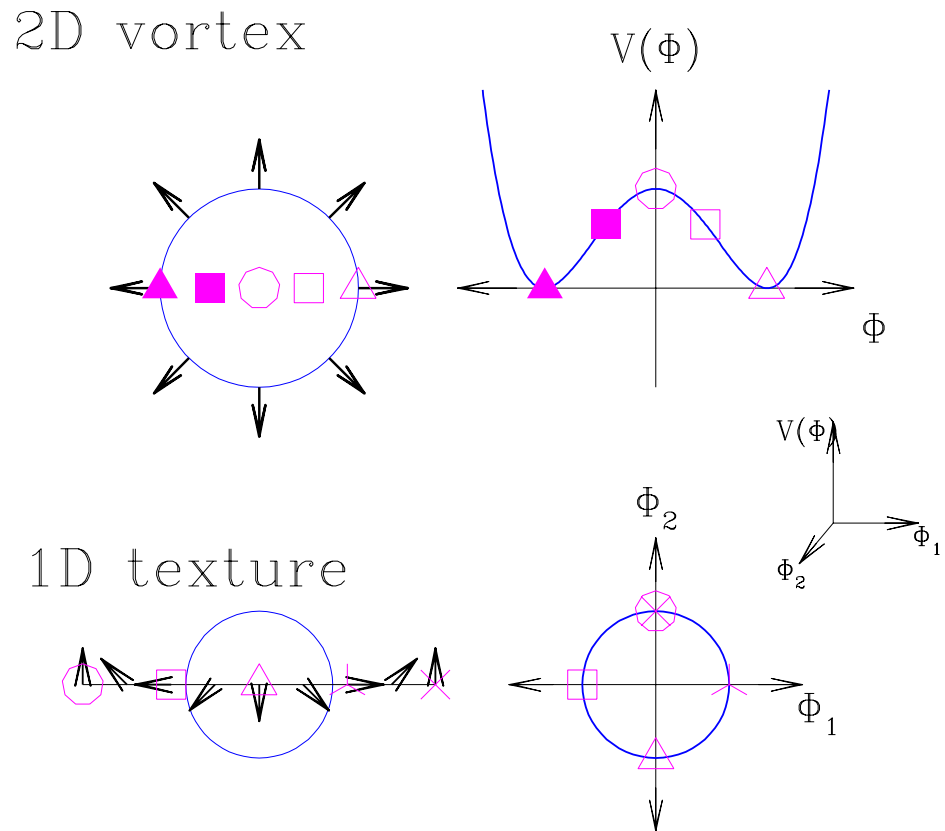
Figure 5.3: Schematic of a texture. In each case, the circle represents the vacuum manifold. In the upper picture, the arrows represent the value of the doublet field at the location where the arrow starts in the plane. They point in a direction corresponding to the vacuum manifold. To the right of each, is an orthogonal projection of the three-dimensional potential as function of the field. As you go around the origin of the plane, the doublet field traces out the circle that is the vacuum manifold. The bottom picture is essentially the unwinding of the top picture. The symbols represent where points in real space map to on the graph of the potential to the right. To picture 2 or 3 dimensional textures, simply mentally spin this picture about the origin.
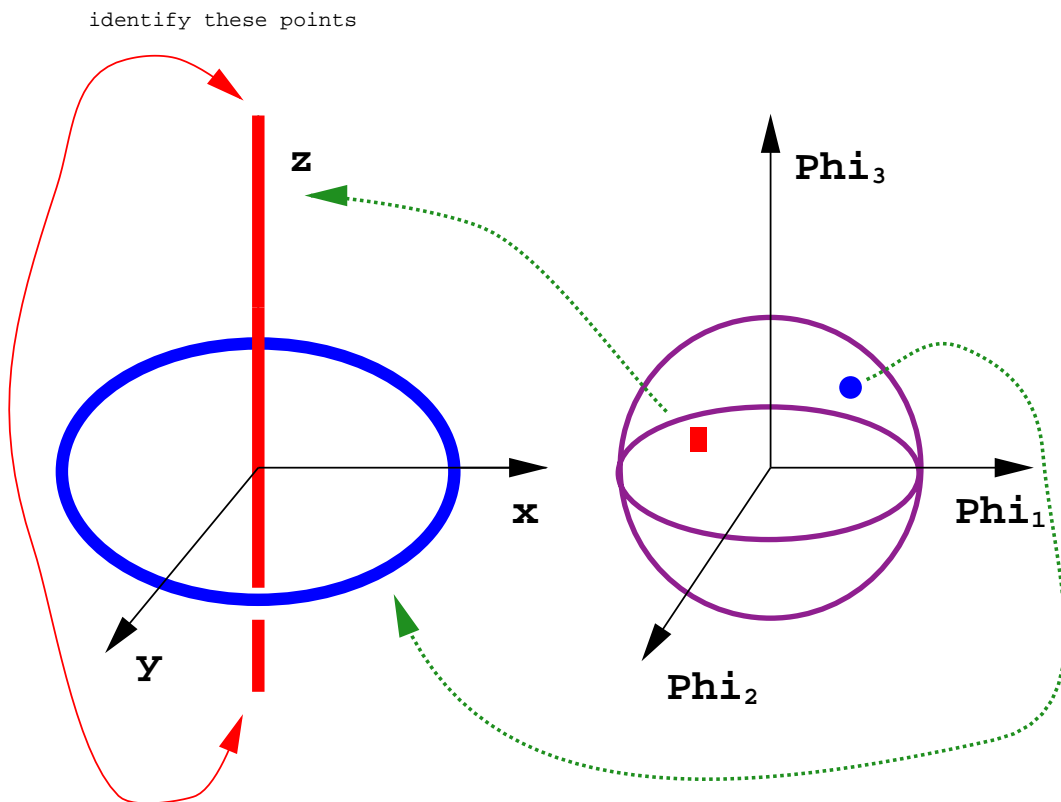
Figure 5.4: Schematic calculation of the Hopf index (charge). On the right is the vacuum manifold, S^2, with two distinct points marked by the square and circle. Given a map from real space to this vacuum manifold, the charge is the linking number of the pre-images of any two distinct points. Here, the pre-image of the point marked with a circle is itself a circle in the xy plane of real space. The pre-image of the square point is the z-axis, itself a circle after compactification $\boldsymbol{R}^3 \rightarrow \boldsymbol{R}^3 \cup \{\infty\} \cong S^3$. The linking number of these two pre-images is one.

zero [76]. Consider the image of some initial configuration which is spherically symmetric in real space. The image will have zero surface area on the sphere because the image will be just a one-dimensional curve on the sphere parameterized by r. We can then pick two points on the sphere not in the image. Since their pre-image is null, their linking number is zero.

5.6 Regularity Issues

Sanchez reviews the long history of harmonic maps in physics [77]. Parallel to these physical applications, mathematicians have studied the regularity properties of these maps. Chao-Hao showed that maps from 1+1 Minkowski space into a general dimensional Riemannian manifold are regular [18]. Struwe extends these results in his study of regularity of wave maps of $(m + 1)$ Minkowski into compact Riemannian manifolds for $m = 2, 3$ [87]. Other results can be found by Christodoulou, Shatah, and Tahvildar-Zadeh [20, 80, 81, 82].

As the geometry is quite different for $\kappa > 0$ and $\kappa < 0$, we consider the latter case first. For $\kappa < 0$ and no coupling to gravity, the energy is proportional to

$$E \propto \frac{|\nabla F|^2}{\left(1 + |\kappa||F|^2\right)^2}, \qquad (5.50)$$

as can be seen from the action (5.1). Because the denominator is always non-zero, the only way for the energy to go to infinity is when $|\nabla F| \to \infty$. Indeed this behavior is observed as shown in Figure 5.5. However, the evolutions suggest that apparently singular behavior is accompanied by $|F| \to \infty$ and that the energy is bounded and small. In fact, it appears that physically, all that is occurring is that the field is going over a pole in the internal space. The stereographic projection cannot cover the whole sphere, and hence one of the poles is a singular point of the map, albeit a coordinate singularity.

Before dismissing this singular behavior as a coordinate singularity in the internal space and hence not of physical interest, consider this theory as if we were ignorant of the geometry of the internal space. We have a nonlinear field theory which apparently develops singularities at a finite time and for $r > 0$. The energy appears bounded while $|F| \to \infty$. Are there any invariants that go to infinity? With respect to what must this quantity be invariant? The quantity $|F|$ is invariant with respect to changes in coordinates. We can change the coordinates of the internal space as described in Section 5.3, but a pole will always exist which is singular for those coordinates.

For $\kappa > 0$, the target space is now a hyperboloid instead of a sphere. The energy is proportional to

$$E \propto \frac{|\nabla F|^2}{\left(1 - |\kappa||F|^2\right)^2}, \qquad (5.51)$$
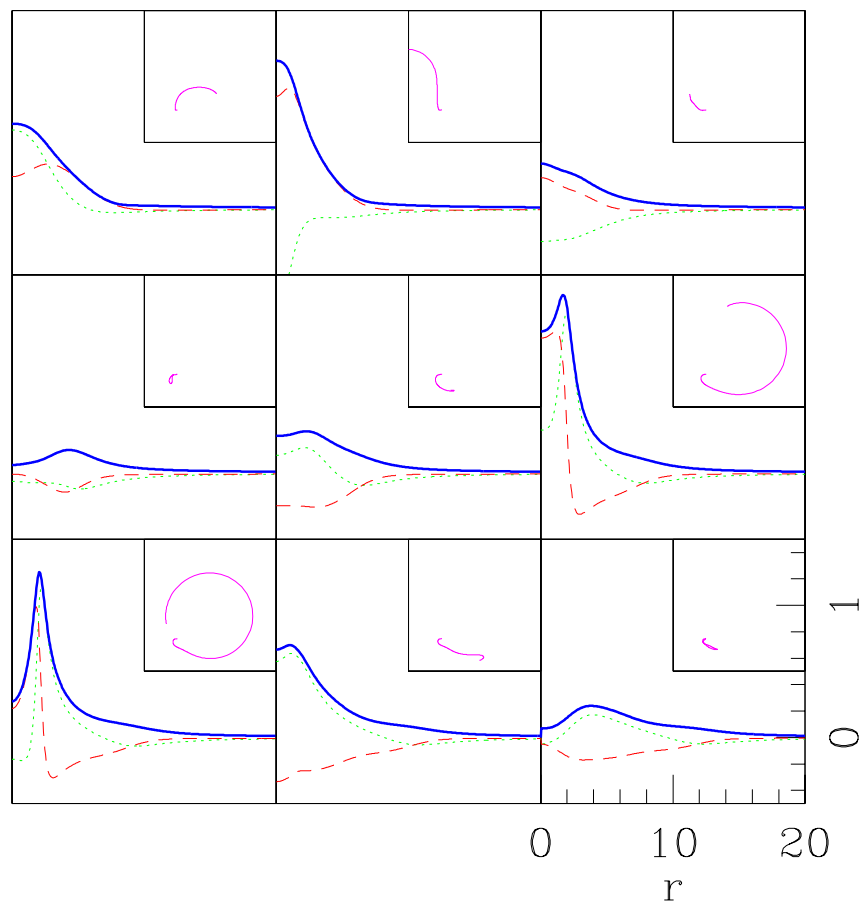
Figure 5.5: Typical evolution of flat-space harmonic map for $\kappa = -10$. The fields ψ (dashed), ϕ (dotted), and $|F|$ (bold) are shown at uniform time intervals (left-to-right, top-to-bottom). The inset boxes display the field on the complex F-plane. If the initial amplitudes were increased, this kink would grow until the code crashed.

which is singular for $|F|^2 \rightarrow 1/|\kappa|$. Geometrically this singularity corresponds to the fact that the map's image, being the projection of the hyperboloid onto the complex plane, only exists on the open disk $r \in [0..1/\sqrt{\kappa})$ in the F-plane.

In fact, the energy (5.51) can be expressed as a metric induced on the internal space (the complex plane) where the line element, dE^2, is here an infinitesimal energy instead of a length

$$dE^2 = \left(\frac{1}{1 - \kappa|F|^2} \right)^2 dF^2. \qquad (5.52)$$

Calculating the "distance" on the complex plane from the center of the disk, $|F| = 0$, to the boundary, $|F| = 1/\sqrt{\kappa}$,

$$
\begin{aligned}
E &= \int_0^{1/\sqrt{\kappa}} \left(\frac{1}{1 - \kappa|F|^2} \right) dF \\
&= \frac{1}{\sqrt{\kappa}} \text{arctanh} \left(\sqrt{\kappa} F \right) \Big|_0^{1/\sqrt{\kappa}} \\
&= \infty.
\end{aligned}
\qquad (5.53)
$$

Thus, it takes an infinite amount of energy to send the scalar field to the boundary of the disk. If the field hits the disk boundary at $r = 0$, then it seems possible that the integral (in real space) of the energy as a function of r can still remain finite. If it is possible, then the formation of a true singularity ($E \rightarrow \infty$) seems possible.

The numerical evolutions suggest that indeed, for smooth initial values of $|F|$ sufficiently large, the value of $|F|$ tends towards infinity at $r = 0$. Of course, though the evolutions suggest this, the numerical modeling of this limit encounters difficulties, and it is hard to firmly establish that indeed the continuum equations imply singularity formation from smooth initial data in finite time.

Chapter 6

Critical Phenomena in the Harmonic Map

Using the equations of motion discussed in Section 5.1, critical phenomena in the harmonic map is studied. In particular, the model reproduces the results of [54] (see Chapter 3) in the regime where the two models are equivalent, namely for $\kappa > 0$.

6.1 Previous Critical Results

From the previous studies [43] and [54], an interesting picture of critical phenomena parameterized by κ, the negative of the target curvature, emerges. Figure 6.1 shows a schematic of the stability of these critical solutions CSS and DSS.

In particular, for large κ, the CSS has only one unstable mode and is hence an intermediate attractor. Hirshmann and Eardley demonstrated this with a linear perturbation analysis [43]. The fully nonlinear evolutions of [54] confirm this stability and establish empirically that the DSS is not an intermediate attractor for $\kappa \gtrsim 0.08$. Below this threshold, the evolutions show that the DSS is an intermediate attractor while the CSS is not. This is consistent with Hirschmann and Eardley's finding that the CSS has a change of stability at $\kappa \approx 0.075$, and, for κ below this value, it has more than one unstable mode.

The evolutions and perturbation results suggest the existence of a Hopf-like bifurcation at $\kappa \approx 0.08$ whereby a fixed point (the CSS) and a limit cycle (the DSS) exchange stability. This bifurcation is drawn schematically on the right side of Figure 6.1. The CSS is represented along the horizontal axis with either a solid thick line where stable or a dashed thick line where unstable. The DSS is represented by the circle around this axis. The drawing is only a finite-dimensional representation of the infinite-dimensional phase space. Example trajectories are represented in constant κ planes by (non-bolded) curves. The arrows on these curves represent the direction of flow. For $\kappa \gtrsim 0.08$, the trajectories (i.e. critical searches) find the CSS. Below this bifurcation, critical searches find the DSS.
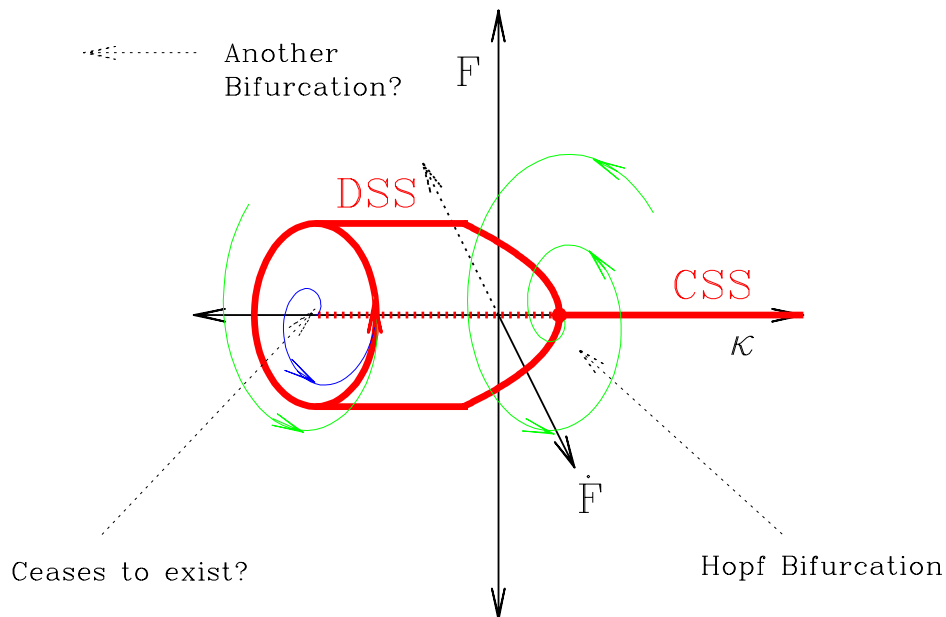
Figure 6.1: Schematic of Hopf-like bifurcation in the stability of critical solutions in the harmonic map. This picture is just a finite-dimensional representation of the infinite-dimensional phase space. The horizontal coordinate represents the κ axis, while the remaining two axes represent schematically the scalar field and its conjugate momentum. The DSS is represented by the thick circle around the κ axis and is shown where stable. The CSS is drawn along the horizontal axis with a solid line where stable and dashed otherwise. Stability here means the existence of *only* one unstable mode. Trajectories occur in planes of constant κ and are represented here by non-bolded curves with arrows denoting the direction of flow.

6.2   Extensions to Brans-Dicke

The harmonic map generalizes the Brans-Dicke model studied in Chapter 3 and [54]. Thus, the picture presented above can be extended.

For large, positive κ, the code cannot find a critical solution because of apparent singularities. That is to say that as κ is increased, the radius of the domain of the target space $1/\sqrt{\kappa}$ shrinks and approaches the initial amplitude of the scalar field necessary to produce black holes. The possibility that these numerical difficulties represent actual singularity formation is discussed in Section 5.6. This limit in which κ becomes large exists in the Brans-Dicke model where $\lambda \to \infty$ and, equivalently, $\omega \to -3/2$. Numerical problems also hindered results in that limit for that model.

However, in the region $\kappa \gtrsim 0.08$ in which we can find a critical solution, we generically find the CSS. Figure 6.2 diagrams the attracting critical solution in parameter space. The top half of which shows that the CSS is the demonstrated attractor in this regime. The horizontal axis represents whether the initial data is generic, non-special Gaussian initial data, or the special initial data called "spiral" which is discussed in Chapter 6.6. Generically, it is the left side (Gaussian) of the diagram which is of importance here.

The bifurcation discussed in the previous section sits at the boundary between CSS and DSS on the left side of the diagram at $\kappa \approx 0.08$. In this region, initial data will generically find the DSS. For $\kappa \leq 0$, the harmonic model has no correspondence to the Brans-Dicke model.

For κ in the range $0.08 \gtrsim \kappa \gtrsim -2$, generic initial data finds what appears to be the DSS. However, the results indicate a gradual transition to yet another critical solution which has discrete structure. This new critical solution is studied in the next section.

Below $\kappa \approx -0.6$, Hirschmann and Eardley were unable to find the CSS solution, let alone study its stability. It is possible it does not exist there [43]. This result hints at possibly another bifurcation which may be what we see by the appearance of this new critical solution. However, for large, negative values of κ another apparent singularity develops and restricts the region in which we can find critical solutions. This type of singularity is also discussed in Section 5.6.

Motivated to find initial data which could form small black holes and avoid the apparent singularity for negative κ, I looked for initial data which would maximize its energy content with minimizing its amplitude. I found that initial data of the form

$$F(r,t) = f(r)e^{i\omega r}, \tag{6.1}$$

extended the range of negative κ over which a critical solution could be found. I call this data spiral initial data. This form for the initial data has interesting properties as discussed
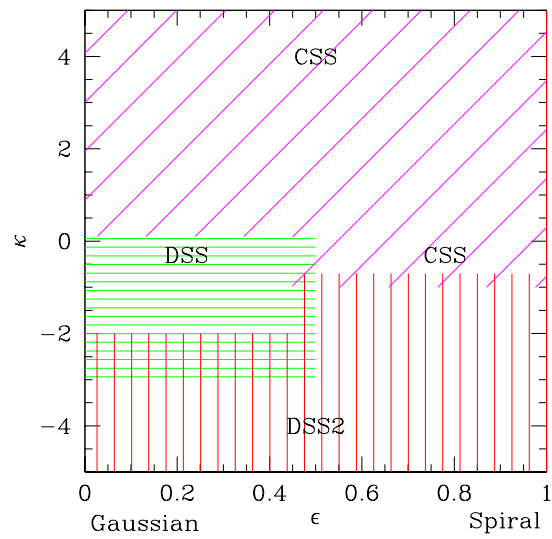
Figure 6.2: Schematic diagram of the attracting critical solutions for various regions of κ. The parameter ϵ represents a mixing of Gaussian and spiral types of initial data. Pure Gaussian initial data is represented by $\epsilon = 0$ while $\epsilon = 1$ represents strictly spiral initial data. For $\kappa \gtrsim 0.1$ the CSS is the only critical solution found. For $\kappa \approx 0.1$ a transition is observed to the DSS solution for Gaussian data, while the spiral data continues to find the CSS. For $\kappa < 0$, both types of initial data result in a critical solution different than the CSS and the DSS. The label DSS2 designates the new, discretely self-similar family of solutions found. The region of parameter space corresponding to the Brans-Dicke model as studied in Chapter 3 lies in the region $\kappa > 0$.

in Chapter 6.6. However, what concerns us here is the critical solution it finds for negative κ.

Before discussing this new critical solution, a remark concerning the bottom of Figure 6.2 is in order. One of the surprising results about the spiral initial data is that it appears incapable of finding the DSS critical solution. Hence, in the region where a new critical solution appears, the spiral initial data is transitioning from the CSS to a unique, discretely self-similar solution (called here DSS2). However, generic initial data will be transitioning from the DSS and so the unique properties of the DSS2 are *perhaps* less clearly emerging. Indeed, it is not certain that these two types of initial data are finding the same DSS2 solution in the limit $\kappa \to -\infty$, though they both appear to find solutions different than the DSS.

Studying this regime is even more difficult because for generic initial data, only the region $\kappa \geq -3$ can be studied whereas with the spiral initial data I have found critical solutions down to $\kappa = -60$.

6.3 A New Critical Solution

The new solution exhibits some form of discrete self-similarity with structure more complicated than the original DSS solution. The solution appears to combine the phase characteristics of the CSS solution (i.e. charge) along with the discrete structure in the energy density of the DSS.

We interpret the results shown in Fig. 6.3 as suggesting that the additional structure comes from period doubling. In the bottom left graph of the figure, we plot the value of the fields at the origin as a function of the logarithm of the time to collapse for a slightly subcritical solution. The graph shows a regular oscillation of some particular frequency, along with an oscillation occurring with twice that frequency every other period.

Beyond making sense of the structure of this new solution, the question of whether the spiral and Gaussian initial data find the same new solution. Figure 6.4 addresses this question by displaying the critical solutions found for the same value of $\kappa = -3$ with both the Gaussian and spiral initial data.

Though both graphs make clear features different than both the CSS and DSS have developed, it is not at all clear that they are approaching the same solution. It is unfortunate that we can not find critical solutions for even more negative κ with the Gaussian initial data. Perhaps with a better understanding of the singular behavior, this situation can be rectified.

As somewhat of a summary and to facilitate comparison, the three critical solutions are shown in Figure 6.5.
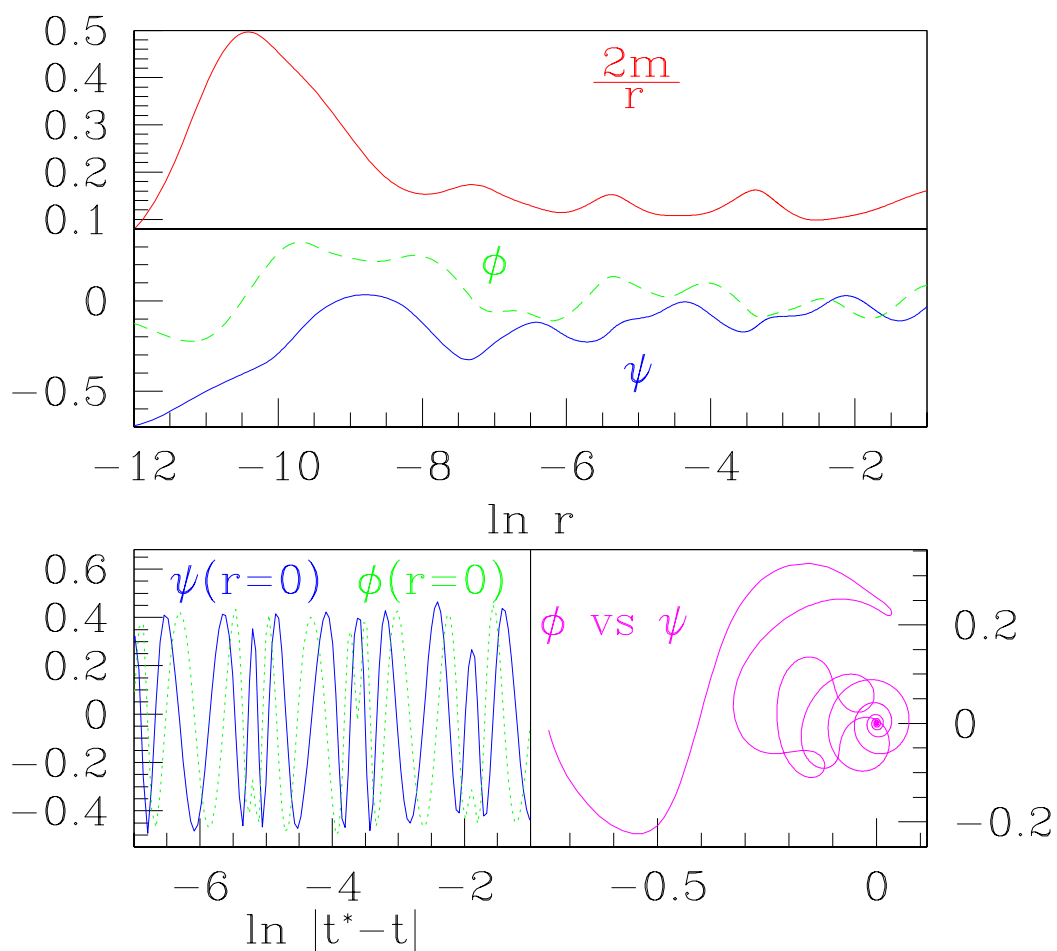
Figure 6.3: Features of the new critical solution (DSS2) for $\kappa = -5$. The nature of the bottom two graphs suggests a possible period doubling. The bottom left graph shows the values of the real and imaginary parts of the scalar field at the origin with respect to the logarithm of the time to collapse. The bottom right shows the fields in the projected tangent plane ϕ versus ψ.
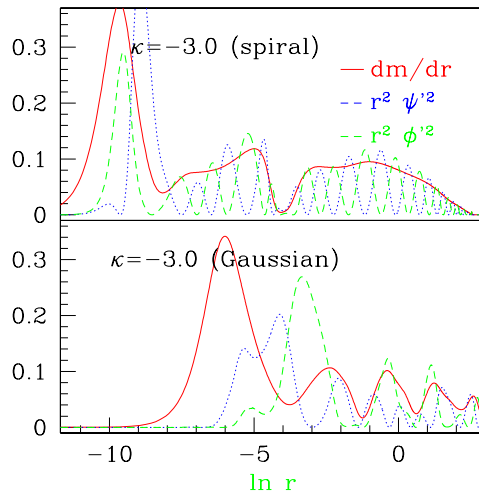
Figure 6.4: Comparison of critical solutions obtained at $\kappa = -3$ for both the spiral and the Gaussian initial data. Because of strange behavior of the Gaussian data at smaller κ, we have been unable to obtain critical solutions less than $\kappa < -3$. However, from the similarities of the above critical solutions, it appears that the spiral and Gaussian converge to this new solution.

As part of an effort to study the possibility of period doubling, I plot the values of the real and imaginary parts of the scalar field at the origin as a function of time. Figure 6.6 displays the values renormalized by $\sqrt{|\kappa|}$ while Figure 6.7 shows them unnormalized. Figure 6.8 shows the rescaled values plotted versus a rescaled log time. Finally, Figure 6.9 shows the similar values for Gaussian initial data. Fourier analysis of the waveform should shed more light on this structure, but so far it has revealed little.

6.4 Mass Scaling

In Fig. 6.10, the power-law fits for various κ are shown. In each frame except that for $\kappa = -15$, the fit obtained with spiral initial data and that for Gaussian initial data are shown. In the fit for Gaussian initial data, the sinusoidal oscillations about a linear fit found for the DSS are only slightly apparent [48]. However, oscillations for the spiral initial data are clearly apparent with their amplitude increasing with decreasing κ. These oscillations are occurring where the critical solution is transitioning from the CSS to the DSS2, not where the DSS is the critical solution.

In Fig. 6.11, the relationship between γ and κ is displayed for the two types of initial data. Finding the critical solution with much precision for large negative κ has been difficult
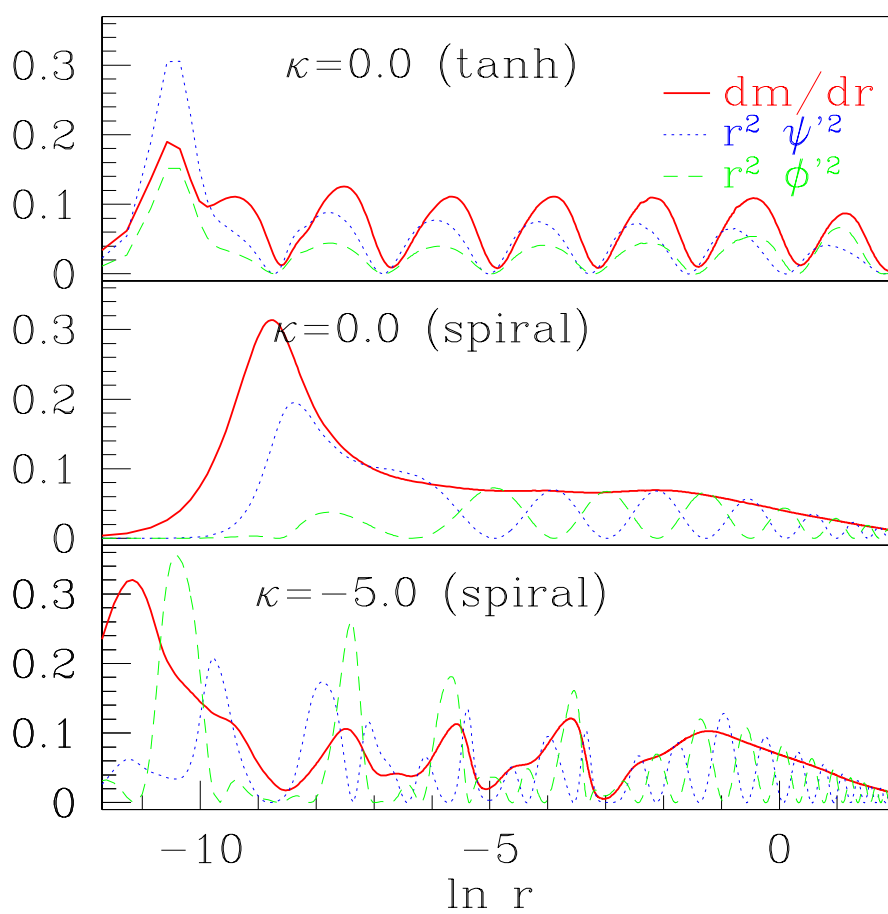
Figure 6.5: Examples of the three different critical solutions: CSS, DSS, and DSS2. The top frame graphs the original DSS obtained for $\kappa = 0$. The fields demonstrate 'echoing' in $\ln r$. The middle frame shows the CSS solution obtained with spiral initial data with $\kappa = 0$. The 'echoing' here appears as a phase oscillation in the complex field.
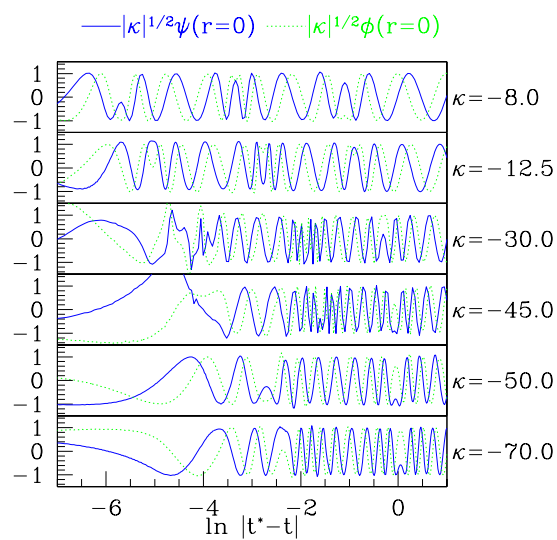
Figure 6.6: Values of the fields at the origin $\psi(r = 0)$ and $\phi(r = 0)$ for spiral initial data rescaled by $\sqrt{|\kappa|}$.
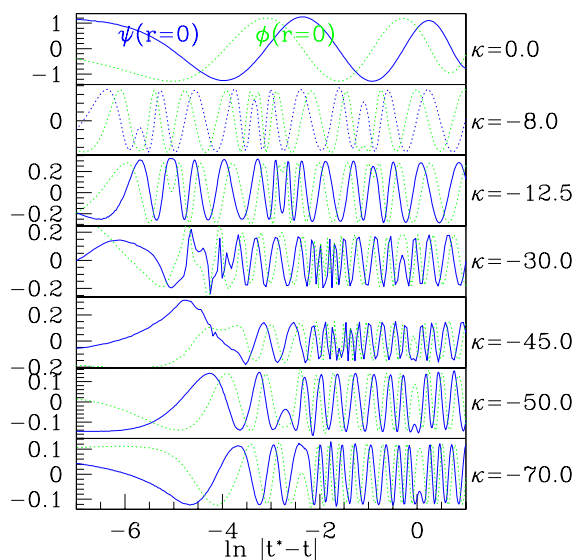
Figure 6.7: Values of the fields at the origin $\psi(r = 0)$ and $\phi(r = 0)$ for spiral initial data.
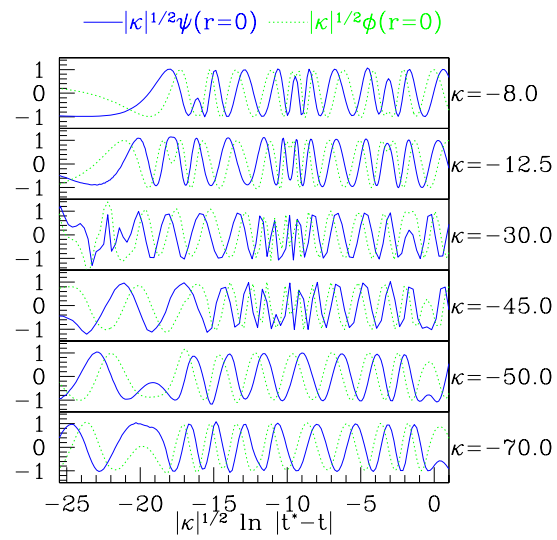
Figure 6.8: Values of the fields at the origin $\psi(r = 0)$ and $\phi(r = 0)$ for spiral initial data rescaled by $\sqrt{|\kappa|}$ with log time rescaled similarly.
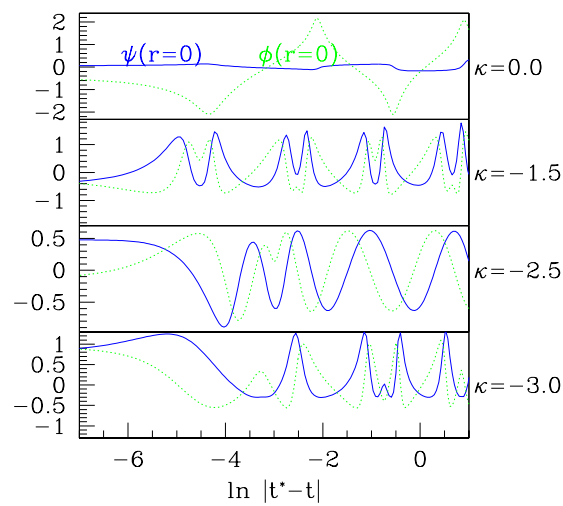
Figure 6.9: Values of the fields at the origin $\psi(r = 0)$ and $\phi(r = 0)$ for Gaussian initial data.
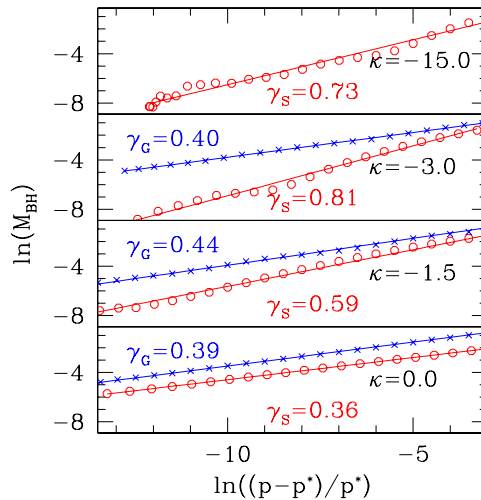
Figure 6.10: Demonstration of mass scaling. Both the masses for spiral initial data (open circles) and Gaussian initial data are shown (crosses). The straight lines denote the linear fits. Oscillations about the linear fit for the spiral initial data appear larger than that for the Gaussian data.

and presumably has resulted in a lack of accuracy in the critical exponents.

6.5 Charge Scaling

Only preliminary results are available for charge scaling in the harmonic map at this time. The issue of charge scaling about the DSS for the complex scalar field (i.e. $\kappa = 0$) has been addressed in the case that the $U(1)$ gauge field is present. The work of [38] predicted a charge scaling exponent $\eta_{\mathrm{DSS}} = 0.88$ which was also independently predicted and observed in [47].

Here, no gauge field is present, but the $U(1)$ charge (5.5) is still present. Implementation details concerning computing the charge integral up to the radius of the black hole formed have made the uncertainty concerning the charge scaling significantly greater than that for the black hole mass scaling. Figure 6.12 displays the charge scaling observed with data which finds the DSS critical solution. The computed values are roughly $\eta_{\mathrm{DSS}} \approx 0.91$, which, though different from $\eta_{\mathrm{DSS}} = 0.88$, is likely consistent within uncertainty with the previous results.

Because spiral initial data finds the CSS for $\kappa = 0$, the charge scaling about the CSS can be computed. In this case, the critical solution has charge and also has multiple unstable modes (for $\kappa = 0$). Results from such a calculation are shown in Figure 6.13. A value of η_{CSS} in the range of $0.66 \leq \eta_{\mathrm{CSS}} \leq 0.74$ is consistent with the data.
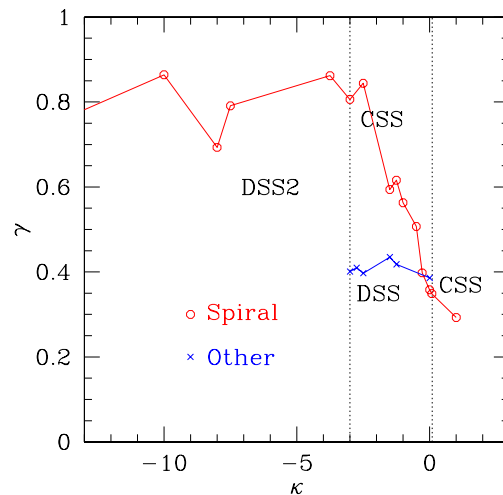
Figure 6.11: Mass scaling exponents γ versus κ. The open circles represent data obtained with spiral initial data, while the crosses denote values obtained with non-spiral initial data. The dashed lines are drawn for the approximate values of κ at which transitions in the critical solutions are observed.

With further work, the charge scaling exponents for various κ can be computed.

6.6   Finding Multiply Unstable Critical Solutions

Here the issue of universality is examined. Universality comes about because of the presence of only one unstable (relevant) mode about the critical solution. The single unstable mode sends nearby trajectories in phase space away from the critical solution. The trajectories either disperse or form black holes. This mode is then appropriately called the black hole mode. Though the critical solution is unstable, the process of tuning progressively limits the influence of the mode, delaying its growth. Modulo this unstable mode, the critical solution is then an attractor and therefore called an intermediate attractor.

When a critical solution has more than one unstable mode it ceases to be an intermediate attractor. Tuning a one-parameter family of initial data still tunes the black hole mode, but the trajectory will still generically be sent away from such a critical solution by the presence of the other unstable modes.

Because for $\kappa = 0$ the model is identical to the free complex scalar field, the attracting critical solution is known to be the DSS. Hirschmann and Eardley have shown the CSS to have a pair of conjugate unstable modes in addition to the black hole mode for κ near zero [43]. However, their analysis shows that as κ is increased above $\kappa \approx 0.075$ a bifurcation
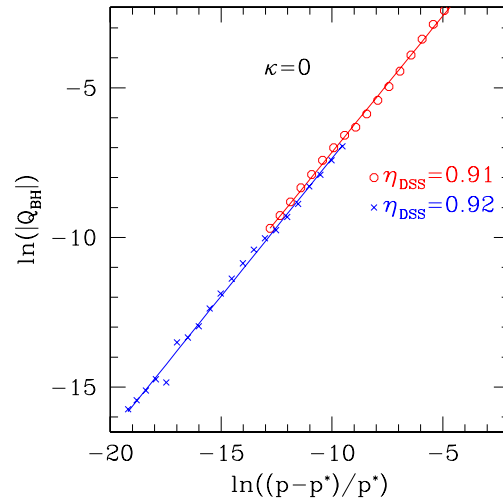
Figure 6.12: Charge scaling observed at $\kappa = 0$ for data which finds the DSS. Two different families were used. The value $\eta_{\mathrm{DSS}} \approx 0.91$ differs from the predicted and observed value $\eta_{\mathrm{DSS}} = 0.88$ in [47], which is likely completely attributable to a large uncertainty in the calculations shown here.
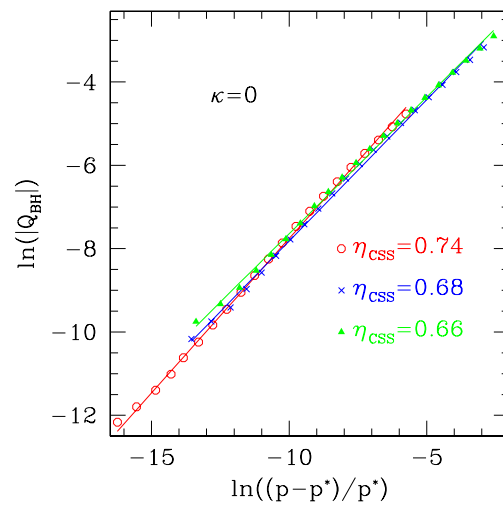
Figure 6.13: Charge scaling observed at $\kappa = 0$ for spiral initial data which finds the CSS. The charge scaling exponent is computed to be in the range $0.66 \leq \eta_{\mathrm{CSS}} \leq 0.74$.

occurs and the extra unstable modes become stable. Hence, in this region, it should be an attracting critical solution, while below this range of κ, the DSS is the critical solution. The evolutions of [54] confirm this change in stability and give evidence that the DSS is not the attractor above $\kappa \approx 0.1$. The harmonic map then has both the CSS and DSS as attracting critical solutions in distinct regions of parameter space.

A remarkable family of initial data (called *spiral* initial data here) is presented which finds the CSS critical solution in the region of parameter space for which the DSS is the demonstrated attractor. In this article, the reasons why this family can find a multiply unstable critical solution are studied. It is argued that the spiral initial data is quite special in that its saturation of a charge bound disallows the growth of the extra unstable modes.

Generally the type of the initial data does not affect the obtained critical solution because of universality, and hence a common choice has been a Gaussian pulse in each of the components

$$
\begin{aligned}
\psi(r, t = 0) &= A_\psi \, e^{-(r-R_\psi)^2/d_\psi^2} \\
\phi(r, t = 0) &= A_\phi \, e^{-(r-R_\phi)^2/d_\phi^2},
\end{aligned}
\tag{6.2}
$$

where $A_\psi, A_\phi, R_\psi, R_\phi, d_\psi, d_\phi$ are arbitrary real constants. For what follows, the choice of either ingoing or time-symmetric initial data does not affect the critical solution found. However, instead of a decomposition into real and imaginary parts, the complex field can be expressed by a magnitude and phase

$$
F(r, t = 0) = f(r, t = 0) \, e^{ih(r, t=0)}
\tag{6.3}
$$

for arbitrary real functions $f(r, t)$ and $h(r, t)$.

The family which is of interest here is most easily expressed in this form where the phase is linear in r

$$
F(r, t = 0) = f(r)e^{i\omega r}
\tag{6.4}
$$

and where ω is an arbitrary real constant. This data represents a generalized spiral in the complex plane and is called *spiral* initial data here. So that the fields are regular and compact, $f(r)$ is constructed such that $f(r \to 0) = 0$ and $f(r_{\max}) = 0$. The constant $r_{\max}$ represents the size of the numerical grid. Also, for reasons that should become clear later, $f(r)$ is constructed so that it varies much more slowly in r than the exponential term. Generally, f is either Gaussian or takes a step-function-like form

$$
f(r) = \frac{1}{4}\Big[1 + \tanh\left(r - r_{\text{low}}\right)\Big]\Big[1 - \tanh\left(r - r_{\text{high}}\right)\Big]
\tag{6.5}
$$

for arbitrary constants $r_{\text{low}} < r_{\text{high}}$.

Spiral initial data is remarkable because critical searches conducted with this data find the CSS critical solution for $\kappa \approx 0$. Figure 6.14 displays the critical solution obtained with various initial data for values of κ for which the DSS is the attractor. These results show that the spiral data is quite special in the space of initial configurations.

Perturbations of this data are made according to

$$
\begin{aligned}
\psi(r, t = 0) &= f(r) \ (A + \Delta A) \ \cos(\omega r + \Delta \varphi) \\
\phi(r, t = 0) &= f(r) \ A \ \sin(\omega r),
\end{aligned}
\tag{6.6}
$$

and the critical solutions obtained are shown in Figs. 6.15 and 6.16. The figures show the last subcritical solution obtained by a critical search at a time just before it decides to disperse. The graphs then represent the outgoing record of the collapse of the self-similar regime towards $\ln r \to \infty$. Large r then represents early time, and the graphs show that as the perturbation is increased, the self-similar pulse gradually develops a discrete oscillation. This development represents the funneling of the solution away from the CSS and toward the DSS.

These results make clear that changing the relative phase of the two fields or their relative amplitudes causes the critical solution to be attracted to the DSS. Perturbations of the relative frequency produces similar results.

While Figures 6.15 and 6.16 show that only initial data completely out of phase finds the CSS, the spiral data can be further perturbed via

$$
F(r, t = 0) = f(r) \exp\left(i\omega r^{p}\right)
\tag{6.7}
$$

for $p \neq 1$ and still be considered $\pi/2$ radians out of phase. However, as shown in Fig. 6.17, for $p \neq 1$ the CSS is not the critical solution. The initial data for these configurations are shown in Fig. 6.18.

Before discussing these results, it is interesting to consider initial data which consists of the superposition of two different frequencies ω_1 and ω_2

$$
F(r, t = 0) = f_1(r)e^{i\omega_1 r} + f_2(r)e^{i\omega_2 r}.
\tag{6.8}
$$

Both the initial data and the critical solution are shown in Fig. 6.19. This example of the superposition of two frequencies finds the CSS as shown in the figure, however, not all examples of this family do. Families with $f_1 = f_2$ and comparable frequencies resulted in critical solutions which appeared CSS.

As mentioned previously, initial data which is otherwise spiral but has $f(r)$ varying on scales comparable to ω is driven away from the CSS critical solution in much the same way that the perturbations shown in Figures 6.15 and 6.16 drive the solution away from the CSS.
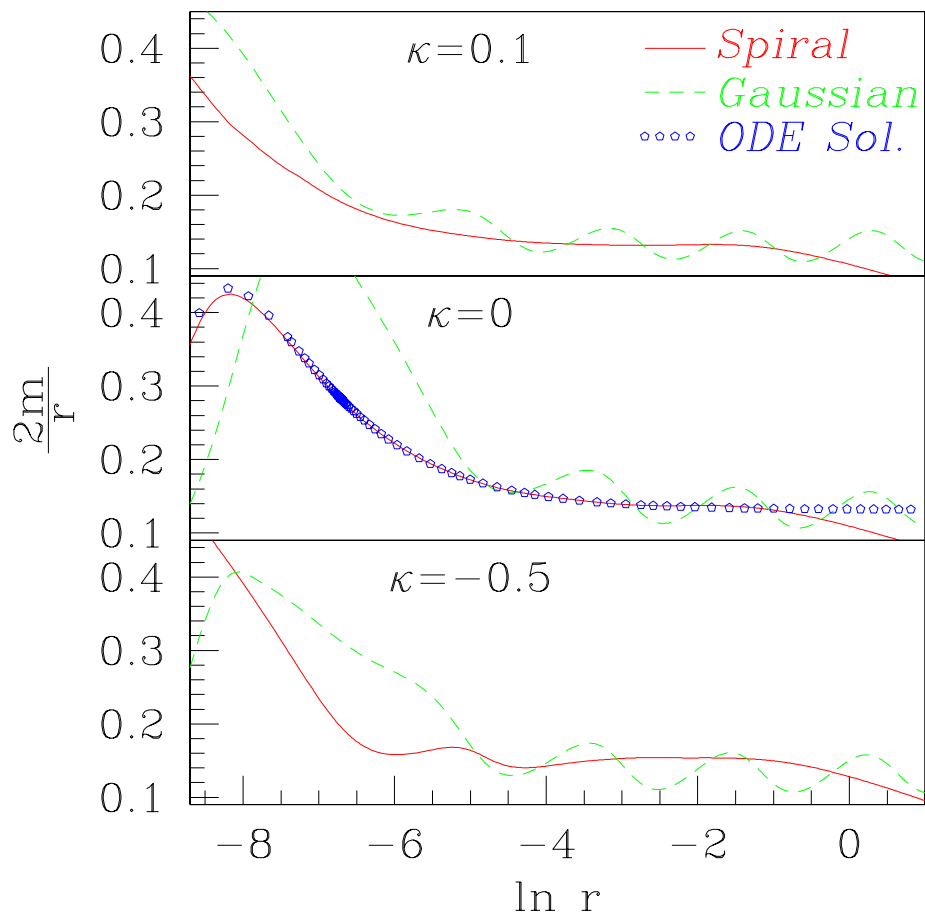
Figure 6.14: Critical solutions for both Gaussian (dashed, Eq. 6.2) and spiral (solid, Eq. 6.3) initial data for $\kappa = 0.1, 0.0, 0.5$. The solution shown with open circles is that found by Hirschmann and Eardley with the assumption of continuous self-similarity [5].
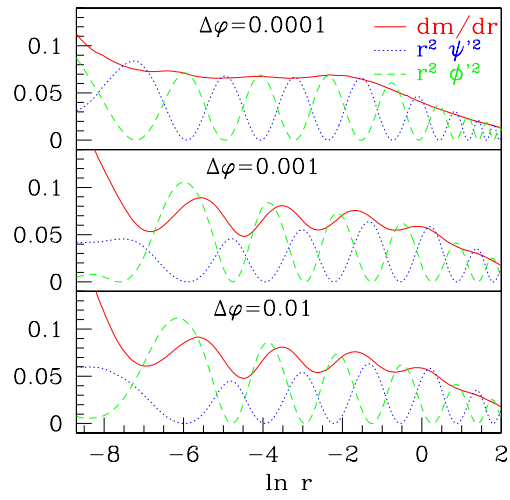
Figure 6.15: Perturbations of phase for the spiral initial data for $\kappa = 0$. Even for small changes in the relative phase of ψ and ϕ, the critical solution is driven toward the DSS.
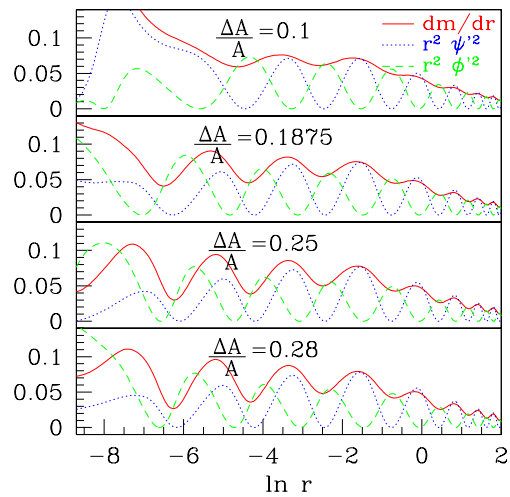
Figure 6.16: Perturbations of relative amplitude for the spiral initial data for $\kappa = 0$. Again, the solution is driven toward the DSS.
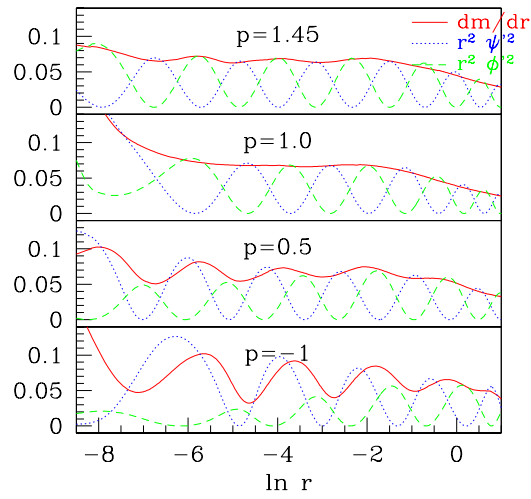
Figure 6.17: Critical solutions ($\kappa = 0$) obtained for the spiral data for various values of p [Eq. (6.7)]. The initial data for these critical solutions are shown in Figure 6.18.
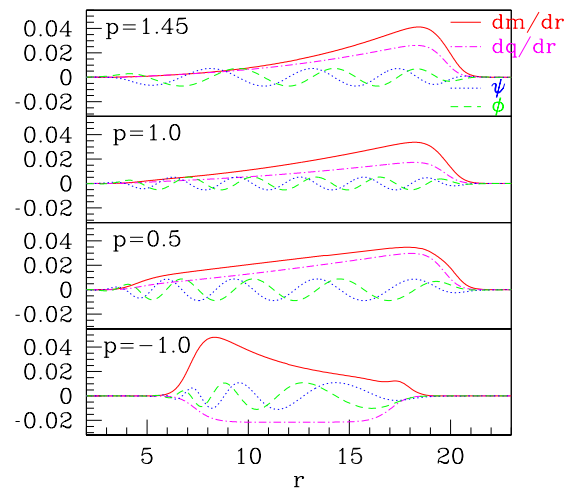
Figure 6.18: Initial data for the critical solutions displayed in Figure 6.17. Here, $\alpha = 1.58, 1.95, 1.17, -2.24$ for $p = 1.45, 1, 0.5, -1.0$, respectively.
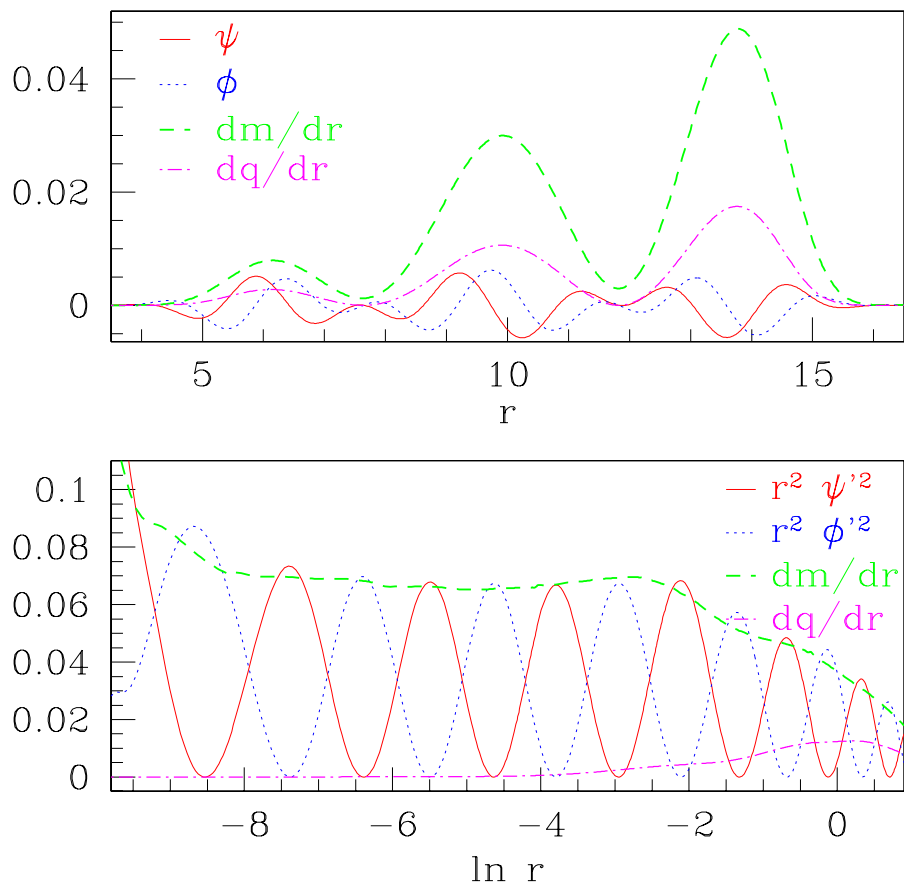
Figure 6.19: Critical solution obtained for initial data consisting of two frequencies $\omega_1 = 2.1$ and $\omega_2 = 3.6$ [Eq. (6.8)]. The top frame shows the initial data. The bottom frame displays the critical solution.

Also, many examples of initial data of the form (6.8) are similarly driven away from the CSS. Experimentally, the strongest indicator of initial data which will find the CSS is when the energy density is everywhere proportional to the charge density. That this proportionality indicates the specialness of spiral initial data is discussed in Section 6.7.2.

6.7 Tuning Two Modes

Surprisingly enough, in this case a discussion of the DSS critical solution in the region $\kappa \gtrsim 0.1$ is simpler than the discussion of the CSS. In this region of parameter space, it is the DSS which has multiple unstable modes, and it is relatively easy to understand the families of initial data which find the DSS. Hence, the discussion of these special families is presented first, followed by a discussion of the specialness of the spiral data.

6.7.1 The DSS

In the harmonic map model, for $\kappa \gtrsim 0.1$ the CSS is the attracting critical solution. Numerical evolutions of various families of initial data generically find the CSS, and do not find the DSS. Gundlach showed that the DSS has only one unstable mode for $\kappa = 0$, but the stability analysis of the DSS has not been done for general κ [37]. However, evolutions of this model, as well as results in the equivalent region of the model in [54], clearly indicate that for $\kappa \gtrsim 0.1$ the DSS has more than one unstable mode.

However, there are non-generic families that do find the DSS in this regime despite the presence of these extra unstable modes. Consideration of this phenomenon is helpful in understanding the CSS occurring for $\kappa = 0$.

One description of initial data that finds the DSS in this regime is mentioned in [54]. In that work it was found that when one component of the field was initially vanishing, it remained zero. The model here, being equivalent to that one for $\kappa > 0$, retains this feature as shown in the equations of motion for the two components of the scalar field in Equation (5.10). Because the CSS is necessarily complex (it has charge), initial data with one field initially vanishing is unable to find the CSS as its critical solution. Thus, families of initial data of the form

$$
\begin{aligned}
F(r) &= f(r) \\
\psi(r) &= f(r) \\
\phi(r) &= 0
\end{aligned}
\tag{6.9}
$$

for arbitrary $f(r)$ will only find the DSS.

However, a more general set of families can be found with this principle in mind. Consider initial data of the form

$$
\begin{aligned}
F(r) &= e^{iC}\, f(r) \\
\psi(r) &= \cos{(C)}\, f(r) \\
\phi(r) &= \sin{(C)}\, f(r)
\end{aligned}
\tag{6.10}
$$

for arbitrary constant C. This data corresponds to a global rotation of Eq. (6.9) by an angle C in the complex plane. Because the Lagrangian is invariant with respect to this rotation, the critical solution must be the same as the initial data described by Equation (6.9).

A more physical understanding of this can be gained by examining the issue of charge. For both sets of initial data (6.9,6.10), the charge is zero. In fact, all components of the current density, Equation (5.4), vanish

$$
j_\mu = 0.
\tag{6.11}
$$

The divergence of this current is zero, so the current density will not grow if initially vanishing. In other words, the system with no charge is in a symmetric state with respect to charge, and this symmetry would have to be broken were the charge to become positive or negative.

Because the CSS can have either positive or negative charge, these sets of initial data are precisely balanced between trajectories that would take them to the CSS with positive charge and those that would take them to the negatively charged CSS (since the model is independent of which field is considered the imaginary component and which the real component of the complex scalar field, the sign of the charge of the CSS is arbitrary). It is this balance that enables them to *see* the DSS as a critical solution with only one unstable mode when in fact it has more than one. The initial data has already tuned one of the extra unstable modes (or an unstable conjugate pair of modes).

With the knowledge that the extra unstable mode corresponds to a charged mode, a two-parameter search can now be conducted. Determination of an appropriately parameterized initial data family is somewhat more subtle than that for the one parameter data. With a one parameter search, a parameterization needs to be smooth and monotonic in the mass of the initial data near the critical point because the excitation of the black hole mode is characterized by the mass contained. Here, that mode must also be tuned, but the unstable charged modes must be tuned as well. Hence, the second parameter must be locally monotonic in charge near the critical point.

A two parameter search with the data

$$
\begin{aligned}
f(R) &= e^{-(r-R)^2/D^2} \\
\psi(r) &= p\, f(R_\psi) \\
\phi(r) &= p\, f(R_\psi - \delta + 10p)
\end{aligned}
\tag{6.12}
$$

finds the DSS. Here, $f(R)$ is a Gaussian pulse centered on some radius R, and R_ψ and D are arbitrary constants. The parameters p and δ are used to tune both the mass and the charge of the initial data. For δ fixed, p effectively tunes the initial energy content. With p fixed and with $\delta \approx 10p$, increasing δ increases the charge from some negative value up to some positive value. Setting $\delta = 10p$ turns the family back into one with zero charge.

With this data, some value for δ near the value $10p$ is chosen, and the black hole critical solution is bracketed sufficiently closely so that the sign of the initial charge of the critical solution is known. A different δ is chosen so that the sign of the charge of the critical solution is found to be the opposite sign. These two values of δ then bracket a critical value δ^* for which the critical solution $(p = p^*)$ has zero charge. In this manner, the DSS is found.

The difference between this two-parameter tuning and using initial data with zero charge is simply the order in which the tuning occurs. In the latter, the initial data is already tuned to have zero charge. The remaining task is then to tune the mass. However in the former, the charge is being tuned first to arrive at a one-parameter family that in general has charge. It is only at the critical value of p that this one-parameter family (found from the δ search) that the solution has zero charge.

In Figure 6.20 a series of critical solutions for $\kappa = 1$ with initial data of the form (6.12) are shown. For each case, $|p - p^*|$ is of order machine precision. The critical solution gets closer to the DSS in the limit $(\delta - \delta^*)/\delta^* \to 0$. Interestingly, while the critical solutions of the perturbed spiral data in Figure 6.16 appeared initially to be headed toward the CSS only to be funneled to the DSS, these solutions do the opposite. They begin initially as DSS solutions but eventually head to the CSS. As they get closer to the critical solution δ^*, the DSS lasts for a progressively longer time. This similarity is consistent with the spiral being tuned to the unstable modes of the CSS.

6.7.2 The CSS

Initial data of the form Equation (6.10) will always find the DSS, because, having no charge, a direction must be picked toward either positive or negative charge to break the symmetry. In the case of finding the multiply-unstable CSS, the spiral data maximizes the charge of the initial data for a given energy, and so it appears that a symmetry must be broken to disperse all the charge and arrive at the DSS.

To find a bound on the charge, consider the norm of the vector

$$\left[F^a F^a F^c_{,\mu} \pm \frac{\left(1 - \kappa|F|^2\right)^2}{2} \epsilon_{cd} F^d j_\mu \right] \tag{6.13}$$

at the initial time for time-symmetric initial data. Because at the initial time all the time components vanish, the norm is positive definite. This is similar to a trick employed by
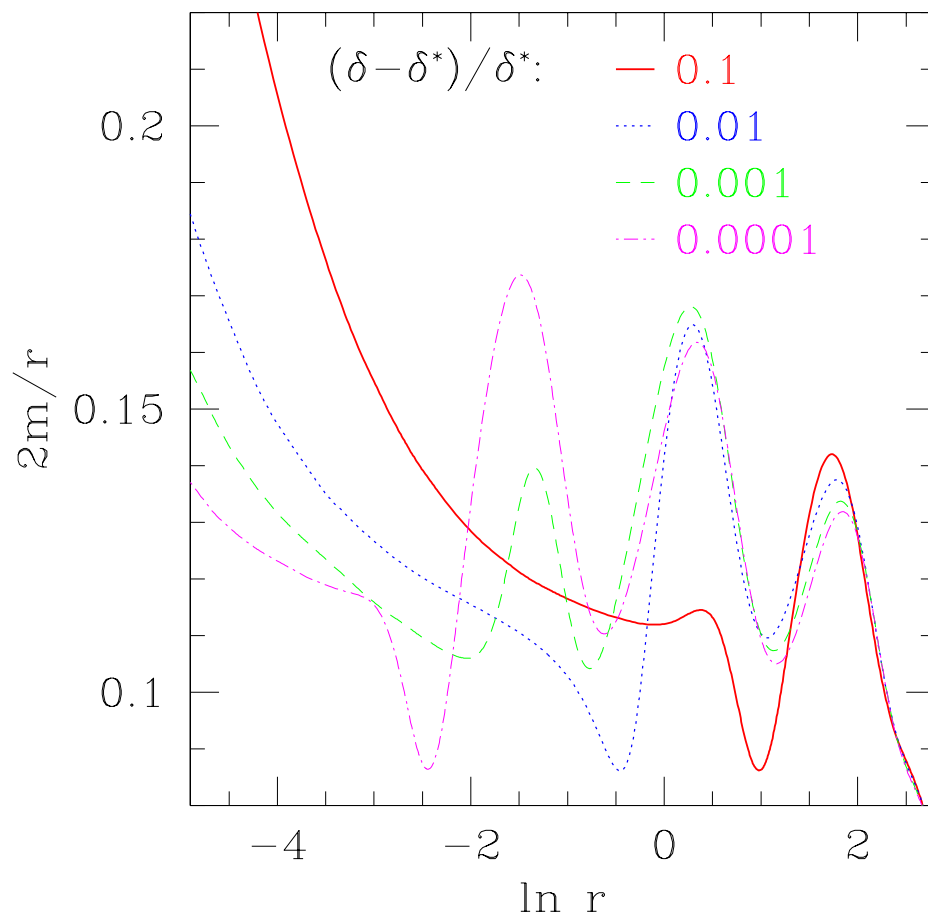
Figure 6.20: Critical solutions with $\kappa = 1$ for various levels of charge tuning $(\delta - \delta^*)/\delta^*$. The initial data is of the form found in Eq (6.12). The field $2m/r$ is shown for $(\delta - \delta^*)/\delta^*$ equal to $0.1, 0.01, 0.001, 0.0001$. As δ approaches δ^* the solution appears discretely self-similar longer but eventually becomes the CSS.

Belavin and Polyakov [8] and described in Rajaraman [71]. Computing

$$\left[F^a F^a F^c_{,\mu} \pm \frac{\left(1 - \kappa |F|^2\right)^2}{2} \epsilon_{cd} F^d j_\mu \right]$$

$$\times \left[F^a F^a F^{c,\mu} \pm \frac{\left(1 - \kappa |F|^2\right)^2}{2} \epsilon_{ce} F^e j^\mu \right] \;\; \geq \;\; 0 \tag{6.14}$$

$$|F|^2 F_{,\mu} F^{*,\mu} \geq \frac{\left(1 - \kappa |F|^2\right)^4}{4} j_\mu j^\mu. \tag{6.15}$$

This inequality (6.15) can be expressed in terms of the energy density for time-symmetric initial data

$$T_{00} = \frac{\alpha^2 F_{,\mu} F^{*,\mu}}{8\pi \left(1 - \kappa |F|^2\right)^2}. \tag{6.16}$$

The bound is then

$$\frac{32\pi |F|^2}{\left(1 - \kappa |F|^2\right)^2} T_{00} \geq \alpha^2 j_\mu j^\mu \tag{6.17}$$

which, for $\kappa = 0$, is simply

$$32\pi |F|^2 T_{00} \geq \alpha^2 j_\mu j^\mu. \tag{6.18}$$

Hence there is an upper limit to the square of the charge density for a given energy density.

Letting the initial data be of the general form (6.3), the condition to saturate this bound for $\kappa = 0$ is

$$\begin{aligned} |F|^2 F_{,\mu} F^{*,\mu} &= \frac{1}{4} j^\mu j_\mu \\ (f')^2 + f^2 (h')^2 &= f^2 (h')^2 \\ (f')^2 &= 0. \end{aligned} \tag{6.19}$$

Saturation therefore occurs when all energy occurs in the phase rotation, h'. Physically, this is apparent by looking at the behavior of F in the complex plane. Because f' vanishes, as F is traced out for various r, the magnitude f does not change; only the phase is changing so the path is a circle on the plane. This tracing then maximizes the area covered for a given energy. The area covered is proportional to the charge, so the charge is maximized.

This analysis applies only for $\kappa = 0$ with time-symmetric initial data, though presumably similar arguments would hold for the generalization to other values of κ and ingoing initial data.

At this point, it is interesting to compare the family (6.10) to the spiral initial data. These two families are, in some sense, complimentary. Pick some r, and imagine that point in the complex plane. To construct data of the form (6.10), determine the field values for all other r by requiring these points to fall on the radial line between this initial point and the origin. In this fashion, the initial data will have some global phase, constant in r, equal

to some value C. However beginning once again from that initial point in the plane, the restriction of Equation (6.19) says that to construct spiral initial data, as r is increased the curve in the plane must lie everywhere *perpendicular* to the radial direction.

Another condition restricting the spiral data appears to be that the charge density must be independent of r. Just as seen with families that find the multiply unstable DSS where the charge density must be everywhere zero independent of r, here the charge density must be everywhere a maximum and independent of r.

In order for the charge density to be independent of r, the rate at which the data covers the plane, $\omega = h'$, must be constant in r. Initial data which would otherwise be spiral but with $h' \neq 0$ are shown in Figure 6.18 with their respective critical solutions shown in Figure 6.17. These results indicate that only for $p = 1$ in Equation (6.7) is the CSS found.

Another perspective on the constraints of the spiral data is afforded by examining the ratio of the charge density to the energy density

$$\frac{j_\mu}{F_{,\mu} F^{*,\mu}} = \frac{2a^2 f^2 h'}{\left(f'\right)^2 + f^2 \left(h'\right)^2} = \frac{2a^2}{h'}. \tag{6.20}$$

That this ratio is approximately independent of r for the conditions $f' = 0$ and $h'' = 0$ appears to indicate that tuning the mass of the initial data also tunes the charge. In other words, with the charge to mass ratio everywhere the same, the critical search cannot find a solution which disperses all the charge.

Construction of smooth, compact, and regular initial data consistent with the restrictions

$$f'|_{t=0} = 0 \qquad h''|_{t=0} = 0 \tag{6.21}$$

is quite difficult. Regularity at the origin requires either $f(r)|_{r=0} = 0$ or $f'|_{r=0} = 0 = h'|_{r=0}$.

Satisfying the former along with strict observance of (6.21) leads to the trivial solution $F(r, t = 0) = 0$. Instead, as mentioned earlier, initial data is used where f vanishes at the origin, but is then "turned on" at some larger r. The condition $f' = 0$ is then not satisfied everywhere, but for $f' \ll \omega$ the CSS is still found.

Satisfying the latter condition along with $h'' = 0$ at the initial time also leads to a trivial solution $F(r, t = 0) = C$, for some complex constant C. Again, ω can be "turned on" at some larger r, but this can only be done in a smooth way if $h''(r, t = 0)$ is not everywhere zero.

The difficulty in constructing non-trivial, regular, initial data which is strictly spiral has hampered the analysis. While initial data of the form (6.10) has the symmetry $\phi(r) = \tan(C) \psi(r)$ which holds at all times, it is not clear if there is such a preserved symmetry here. The approximate symmetry $\phi(r) = \tan(\omega r) \psi(r)$ holds at the initial time for the spiral

data but does not appear to hold throughout the evolution. Also, the bound (6.19) is shown only for time-symmetric initial data but ingoing spiral data also finds the CSS. However, the evolutions consistently show that initial data which has the ratio of charge density to energy density independent of r will find the CSS as its critical solution.

Because both the CSS and DSS can both be found where they have multiple unstable modes, it seems possible that other suitably tuned families in other models might find other, previously unknown multiply unstable critical solutions.

Chapter 7

Axisymmetric Scalar Electrodynamics: A Primer

The modeling of a charged scalar field in axisymmetry represents a nonlinear, and hence nontrivial, dynamical system. It is nevertheless still quite tractable and much simpler than a gravitational collapse model. Presumably, difficulties encountered with this model will also have to be solved with a gravitational code. Thus, it serves as a warm-up to a fully gravitational code, as discussed in Chapter 9.

This work is done in conjunction with Hirschmann. He derived many of the equations and found suitable, regularized fields. Two excellent books that cover these equations are [17, 75]. I initially implemented these equations in RNPL [62, 63], and we both worked to stabilize and debug the code. In addition to an axisymmetric code, a code assuming cylindrical symmetry (a one-dimensional subset of the axisymmetric assumption) is also tested for comparison to the axisymmetric results. This chapter concludes with tests I performed that demonstrate that the code converges, conserves energy, and is stable for a long period of time.

As this model served as an exercise in axisymmetry, little effort was extended in finding interesting dynamics in the model. However, possible future work might be guided by the work of Morris [66].

7.1   Equations of Motion

The action for a complex scalar field ϕ coupled to a $U(1)$ gauge field A_μ takes the form

$$
\begin{aligned}
S &= \int d^4x \ \mathcal{L} \\
&= \int d^4x \ \left[-\left(D_\mu \phi\right)\left(D^\mu \phi\right)^* - \frac{1}{4}F_{\mu\nu}F^{\mu\nu} - a|\phi|^2 - b|\phi|^4 - c|\phi|^6 \right]
\end{aligned}
$$

where $\mathcal{L}$ is the Lagrangian, and a, b, and c are arbitrary constants which determine the potential. The derivative operator D_μ and field strength tensor $F_{\mu\nu}$ are of the usual form

$$
\begin{aligned}
D_\mu &= \nabla_\mu - ieA_\mu & (7.1) \\
F_{\mu\nu} &= \nabla_\mu A_\nu - \nabla_\nu A_\mu. & (7.2)
\end{aligned}
$$

The real and imaginary parts of the complex scalar field are ϕ_1 and ϕ_2

$$\phi = \phi_1 + i\phi_2. \tag{7.3}$$

Variations of the Lagrangian produce the field equations

$$\frac{\partial \mathcal{L}}{\partial \phi} - \nabla_\mu \left\{ \frac{\partial \mathcal{L}}{\partial (\nabla_\mu \phi)} \right\} = 0. \tag{7.4}$$

Using the fact that

$$
\begin{aligned}
\frac{\partial}{\partial \phi^*} \left[-a|\phi|^2 - b|\phi|^4 - c|\phi|^6 \right] &= \frac{\partial}{\partial \phi^*} \left[-a\left(\phi\phi^*\right) - b\left(\phi\phi^*\right)^2 - c\left(\phi\phi^*\right)^3 \right] \\
&= -a\phi - 2b\phi\left(\phi\phi^*\right) - 3c\phi\left(\phi\phi^*\right)^2,
\end{aligned}
$$

the equation of motion for ϕ is

$$\Box\phi = 2ieA^\mu \phi_{,\mu} + e^2 \phi A_\mu A^\mu + ie\phi A^\mu{}_{;\mu} + a\phi + 2b\phi\left(\phi\phi^*\right) + 3c\phi\left(\phi\phi^*\right)^2. \tag{7.5}$$

The equation of motion for the gauge field is

$$F^{\lambda\mu}{}_{;\lambda} = ie\left[\phi^*\phi^{;\mu} - \phi\phi^{*;\mu}\right] + 2e^2\phi\phi^* A^\mu, \tag{7.6}$$

from which the $U(1)$ current is simply

$$j^\mu = ie\left[\phi^*\phi^{;\mu} - \phi\phi^{*;\mu}\right] + 2e^2\phi\phi^* A^\mu, \tag{7.7}$$

with $j^\mu{}_{;\mu} = 0$. The associated Noether charge for this current is then

$$
\begin{aligned}
Q &= \int j^t \, d^3x \\
&= 4\pi e \int \left[\left(\phi_2 \dot{\phi}_1 - \phi_1 \dot{\phi}_2 \right) + e\left(\phi_1^2 + \phi_2^2\right) A_t \right] \rho \, d\rho \, dz. \tag{7.8}
\end{aligned}
$$

Using the usual cylindrical coordinates (t, ρ, z, φ), the flat space metric is

$$1 = g_{rr} = g_{zz} = -g_{tt} = \frac{1}{\rho^2} g_{\varphi\varphi}. \tag{7.9}$$

The only nonzero connection coefficients are

$$\Gamma^\varphi{}_{\rho\varphi} = \frac{1}{\rho} \quad , \quad \Gamma^r{}_{\varphi\varphi} = -\rho. \tag{7.10}$$

With this metric, the D'alembertian becomes

$$\Box\phi = -\phi_{,tt} + \frac{1}{\rho}\left(\rho\phi_{,\rho}\right)_{,\rho} + \phi_{,zz} + \frac{1}{\rho^2}\phi_{,\varphi\varphi}. \tag{7.11}$$

Choosing the Lorentz gauge

$$A^\mu{}_{;\mu} = 0 \tag{7.12}$$

implies

$$
\begin{aligned}
F_{\mu\nu}{}^{;\mu} &= \nabla^\mu \left(\nabla_\mu A_\nu - \nabla_\nu A_\mu \right) \\
&= \nabla^\mu \nabla_\mu A_\nu
\end{aligned}
$$

and Equation (7.6) becomes a wave equation for A_μ.

The full set of field equations is then

$$
\begin{aligned}
\phi_{1,tt} &= \frac{1}{r}\phi_{1,r} + \phi_{1,rr} + \phi_{1,zz} \\
&\quad +2e\left(-A_t\phi_{2,t} + A_r\phi_{2,r} + A_z\phi_{2,z}\right) - e^2\phi_1\left(-A_t{}^2 + A_r{}^2 + A_z{}^2 + \frac{1}{r^2}A_\varphi{}^2\right) \\
&\quad +a\phi_1 + 2b\phi_1\left(\phi_1^2 + \phi_2^2\right) + 3c\phi_1\left(\phi_1^2 + \phi_2^2\right)^2 \\
\phi_{2,tt} &= \frac{1}{r}\phi_{2,r} + \phi_{2,rr} + \phi_{2,zz} \\
&\quad -2e\left(-A_t\phi_{1,t} + A_r\phi_{1,r} + A_z\phi_{1,z}\right) - e^2\phi_2\left(-A_t{}^2 + A_r{}^2 + A_z{}^2 + \frac{1}{r^2}A_\varphi{}^2\right) \\
&\quad +a\phi_2 + 2b\phi_2\left(\phi_1^2 + \phi_2^2\right) + 3c\phi_2\left(\phi_1^2 + \phi_2^2\right)^2 \\
A_{t,tt} &= \frac{1}{r}A_{t,r} + A_{t,rr} + A_{t,zz} \\
&\quad +2e\left(\phi_1\phi_{2,t} - \phi_2\phi_{1,t}\right) - 2e^2(\phi_1{}^2 + \phi_2{}^2)A_t \\
A_{r,tt} &= \frac{1}{r}A_{r,r} + A_{r,rr} + A_{r,zz} - \frac{1}{r^2}A_r \\
&\quad +2e\left(\phi_1\phi_{2,r} - \phi_2\phi_{1,r}\right) - 2e^2(\phi_1{}^2 + \phi_2{}^2)A_r \\
A_{z,tt} &= \frac{1}{r}A_{z,r} + A_{z,rr} + A_{z,zz} \\
&\quad +2e\left(\phi_1\phi_{2,z} - \phi_2\phi_{1,z}\right) - 2e^2(\phi_1{}^2 + \phi_2{}^2)A_z \\
A_{\varphi,tt} &= -\frac{1}{r}A_{\varphi,r} + A_{\varphi,rr} + A_{\varphi,zz} \\
&\quad -2e^2(\phi_1{}^2 + \phi_2{}^2)A_\varphi .
\end{aligned}
$$

The gauge condition specifies that

$$
A_{t,t} = A_{r,r} + A_{z,z} + \frac{1}{r}A_r, \tag{7.13}
$$

which can either be used to update the component A_t or used as a check that the evolution is proceeding correctly.

To make these equations first order, we introduce the auxiliary fields

$$
\Pi_x = \frac{\partial}{\partial t}\phi_x \tag{7.14}
$$

$$
\Omega_x = \frac{\partial}{\partial \rho}\phi_x \tag{7.15}
$$

$$
\Lambda_x = \frac{\partial}{\partial z}\phi_x, \tag{7.16}
$$

where x runs over $1, 2$. Similarly for the gauge fields, we define

$$
B_x = \frac{\partial}{\partial t}A_x \tag{7.17}
$$

$$C_x = \frac{\partial}{\partial \rho} A_x \tag{7.18}$$

$$D_x = \frac{\partial}{\partial z} A_x, \tag{7.19}$$

where x now runs over $1 \ldots 4$.

Regularized fields $\tilde{A}_\rho$ and $\tilde{A}_\phi$ are introduced which have better behavior near the origin than the original components A_ρ and A_ϕ. The new quantities with tildes are now

$$\tilde{A}_\rho = \frac{A_\rho}{\rho} \tag{7.20}$$

$$\tilde{B}_2 = \frac{B_2}{\rho} \tag{7.21}$$

$$\tilde{C}_2 = \frac{C_2 - \tilde{A}_\rho}{\rho} \tag{7.22}$$

$$\tilde{D}_2 = \frac{D_2}{\rho} \tag{7.23}$$

$$\tilde{A}_\phi = \frac{A_\phi}{\rho^2} \tag{7.24}$$

$$\tilde{B}_4 = \frac{B_4}{\rho^2} \tag{7.25}$$

$$\tilde{C}_4 = \frac{C_4}{\rho^2} - \frac{2A_\phi}{\rho} \tag{7.26}$$

$$\tilde{D}_4 = \frac{D_4}{\rho^2}. \tag{7.27}$$

In terms of these first order, auxiliary, regularized fields, the full set of equations of motion is

$$
\begin{aligned}
\phi_{1,t} &= \Pi_1 & \Omega_{1,t} &= \Pi_{1,r} & \Lambda_{1,t} &= \Pi_{1,z} \\
\phi_{2,t} &= \Pi_2 & \Omega_{2,t} &= \Pi_{2,r} & \Lambda_{2,t} &= \Pi_{2,z} \\
A_{t,t} &= B_1 & \tilde{A}_{r,t} &= \tilde{B}_2 & A_{z,t} &= B_3 & \tilde{A}_{\varphi,t} &= \tilde{B}_4 \\
C_{1,t} &= B_{1,r} & \tilde{C}_{2,t} &= \tilde{B}_{2,r} & C_{3,t} &= B_{3,r} & \tilde{C}_{4,t} &= \tilde{B}_{4,r} \\
D_{1,t} &= B_{1,z} & \tilde{D}_{2,t} &= \tilde{B}_{2,z} & D_{3,t} &= B_{3,z} & \tilde{D}_{4,t} &= \tilde{B}_{4,z}
\end{aligned}
$$

$$
\begin{aligned}
\Pi_{1,t} =\ & 2(r\Omega_1)_{,(r^2)} + \Lambda_{1,z} \\
& + 2e\left(-A_t\Pi_2 + r\tilde{A}_r\Omega_2 + A_z\Lambda_2\right) \\
& - e^2\phi_1\left(-A_t{}^2 + r^2\tilde{A}_r{}^2 + A_z{}^2 + r^2\tilde{A}_\varphi{}^2\right) \\
& + a\phi_1 + 2b\phi_1\left(\phi_1^2 + \phi_2^2\right) + 3c\phi_1\left(\phi_1^2 + \phi_2^2\right)^2 \\
\Pi_{2,t} =\ & 2(r\Omega_2)_{,(r^2)} + \Lambda_{2,z} \\
& - 2e\left(-A_t\Pi_1 + r\tilde{A}_r\Omega_1 + A_z\Lambda_1\right) \\
& - e^2\phi_2\left(-A_t{}^2 + r^2\tilde{A}_r{}^2 + A_z{}^2 + r^2\tilde{A}_\varphi{}^2\right)
\end{aligned}
$$

$$+a\phi_2 + 2b\phi_2\left(\phi_1^2 + \phi_2^2\right) + 3c\phi_2\left(\phi_1^2 + \phi_2^2\right)^2$$

$$
\begin{aligned}
B_{1,t} &= 2(rC_1)_{,(r^2)} + D_{1,z} \\
&\quad + 2e\left(\phi_1\Pi_2 - \phi_2\Pi_1\right) - 2e^2(\phi_1{}^2 + \phi_2{}^2)A_t \\
\tilde{B}_{2,t} &= 6\tilde{A}_{r,(r^2)} + \tilde{C}_{2,r} + \tilde{D}_{2,z} \\
&\quad + 4e\left(\phi_1\phi_{2,(r^2)} - \phi_2\phi_{1,(r^2)}\right) - 2e^2(\phi_1{}^2 + \phi_2{}^2)\tilde{A}_r \\
B_{3,t} &= 2(rC_3)_{,(r^2)} + D_{3,z} \\
&\quad + 2e\left(\phi_1\Lambda_2 - \phi_2\Lambda_1\right) - 2e^2(\phi_1{}^2 + \phi_2{}^2)A_z \\
\tilde{B}_{4,t} &= 6(\tilde{A}_\varphi)_{,(r^2)} + \tilde{C}_{4,r} + \tilde{D}_{4,z} \\
&\quad - 2e^2(\phi_1{}^2 + \phi_2{}^2)\tilde{A}_\varphi.
\end{aligned}
$$

The gauge condition becomes

$$B_1 = 2\tilde{A}_r + r\tilde{C}_2 + D_3.$$

The physical fields in terms of these variables are found from the identities

$$
\begin{aligned}
E_i &= F_{i0} & (7.28) \\
|\vec{B}|^2 &= \frac{1}{2}F_{\alpha\beta}F^{\alpha\beta} + |\vec{E}|^2. & (7.29)
\end{aligned}
$$

In terms of the fields here, they become

$$
\begin{aligned}
E_\rho &= C_1 - B_2 = C_1 - \rho\tilde{B}_2 \\
E_z &= D_1 - B_3 \\
E_\phi &= -B_4 = -\rho^2\tilde{B}_4 & (7.30) \\
B_\rho &= \frac{1}{\rho}\left(-D_4\right) = -\rho\tilde{D}_4 \\
B_z &= \frac{1}{\rho}\left(C_4\right) = \rho\tilde{C}_4 + 2\tilde{A}_\phi \\
B_\phi &= \rho\left(D_2 - C_3\right) = \rho^2\tilde{D}_2 - \rho C_3.
\end{aligned}
$$

The stress energy tensor can be constructed from the Lagrangian. Expanding the Lagrangian

$$
\begin{aligned}
\mathcal{L} &= -\left(D_\mu\phi\right)\left(D^\mu\phi\right)^* - \frac{1}{4}F_{\mu\nu}F^{\mu\nu} - a|\phi|^2 - b|\phi|^4 - c|\phi|^6 \\
&= -\left(D_\mu\phi\right)\left(D_\nu\phi\right)^* g^{\mu\nu} - \frac{1}{4}F_{\mu\nu}F_{\alpha\beta}g^{\mu\alpha}g^{\nu\beta} - a|\phi|^2 - b|\phi|^4 - c|\phi|^6 \\
&= -\left(\phi_{,\mu} - ieA_\mu\phi\right)\left(\phi^*_{,\nu} + ieA_\nu\phi^*\right)g^{\mu\nu} - \frac{1}{4}F_{\mu\nu}F_{\alpha\beta}g^{\mu\alpha}g^{\nu\beta} - a|\phi|^2 - b|\phi|^4 - c|\phi|^6 \\
&= \left[-\phi_{,\mu}\phi^*_{,\nu} + ie\left(A_\mu\phi\phi^*_{,\nu} - A_\nu\phi^*\phi_{,\mu}\right) - e^2 A_\mu A_\nu\phi\phi^*\right]g^{\mu\nu} - \frac{1}{4}F_{\mu\nu}F_{\alpha\beta}g^{\mu\alpha}g^{\nu\beta} \\
&\quad -a|\phi|^2 - b|\phi|^4 - c|\phi|^6.
\end{aligned}
$$

Computing

$$
\begin{aligned}
\frac{\partial}{\partial g^{\rho\sigma}} \left[F_{\mu\nu} F_{\alpha\beta} g^{\mu\alpha} g^{\nu\beta} \right] &= F_{\mu\nu} F_{\alpha\beta} \frac{\partial \left[g^{\mu\alpha} g^{\nu\beta} \right]}{\partial g^{\rho\sigma}} \\
&= F_{\mu\nu} F_{\alpha\beta} \left[g^{\mu\alpha} \delta_\rho^\nu \delta_\sigma^\beta + g^{\nu\beta} \delta_\rho^\mu \delta^\alpha \sigma \right] \\
&= F_{\mu\rho} F^\mu{}_\sigma + F_{\rho\nu} F_\sigma{}^\nu \\
&= F_{\rho\mu} F_\sigma{}^\mu + F_{\rho\nu} F_\sigma{}^\nu \\
&= 2 F_{\rho\mu} F_\sigma{}^\mu,
\end{aligned}
$$

we then have

$$
\begin{aligned}
\frac{\partial L}{\partial g^{\mu\nu}} &= \left[-\phi_{,\mu} \phi_{,\nu}^* + ie \left(A_\mu \phi \phi_{,\nu}^* - A_\nu \phi^* \phi_{,\mu} \right) - e^2 A_\mu A_\nu \phi \phi^* \right] \\
&\quad - \frac{1}{2} F_{\mu\alpha} F_{\nu\beta} g^{\alpha\beta} \\
-2 \frac{\partial L}{\partial g^{\mu\nu}} &= 2 \phi_{,\mu} \phi_{,\nu}^* - 2ie \left(A_\mu \phi \phi_{,\nu}^* - A_\nu \phi^* \phi_{,\mu} \right) + 2 e^2 A_\mu A_\nu \phi \phi^* \\
&\quad + F_{\mu\alpha} F_{\nu\beta} g^{\alpha\beta}.
\end{aligned}
$$

The stress energy then is

$$
\begin{aligned}
T_{\mu\nu} &= -2 \frac{\partial L}{\partial g^{\mu\nu}} + g_{\mu\nu} L \\
&= 2 \phi_{,\mu} \phi_{,\nu}^* - 2ie \left(A_\mu \phi \phi_{,\nu}^* - A_\nu \phi^* \phi_{,\mu} \right) + 2 e^2 A_\mu A_\nu \phi \phi^* \\
&\quad + F_{\mu\alpha} F_{\nu\beta} g^{\alpha\beta} \\
&\quad + \left[-\phi_{,\sigma} \phi^{*,\sigma} + ie \left(A_\sigma \phi \phi^{*,\sigma} - A_\sigma \phi^* \phi^{,\sigma} \right) - e^2 A_\sigma A^\sigma \phi \phi^* \right] g_{\mu\nu} \\
&\quad - \frac{1}{4} F_{\rho\sigma} F^{\rho\sigma} g_{\mu\nu} - g_{\mu\nu} \left[a|\phi|^2 + b|\phi|^4 + c|\phi|^6 \right].
\end{aligned}
$$

In these fields, this is then

$$
\begin{aligned}
T_{00} &= \Pi_1^2 + \Pi_2^2 + \Omega_1^2 + \Omega_2^2 + \Lambda_1^2 + \Lambda_2^2 \\
&\quad + 2e \left(A_t \left(\phi_2 \Pi_1 - \phi_1 \Pi_2 \right) + A_r \left(\phi_2 \Omega_1 - \phi_1 \Omega_2 \right) + A_z \left(\phi_2 \Lambda_1 - \phi_1 \Lambda_2 \right) \right) \\
&\quad + e^2 \left(A_t^2 + A_r^2 + A_z^2 + \frac{A_\varphi^2}{\rho^2} \right) \left(\phi_1^2 + \phi_2^2 \right) \\
&\quad + \frac{1}{2} \left(|\vec{B}|^2 + |\vec{E}|^2 \right) + a \left(\phi_1{}^2 + \phi_2{}^2 \right) + b \left(\phi_1{}^2 + \phi_2{}^2 \right)^2 + c \left(\phi_1{}^2 + \phi_2{}^2 \right)^3.
\end{aligned}
$$

We can decompose this into constituent energy densities (scalar field, coupling, electromagnet, potential, and total) as follows

$$
\begin{aligned}
E_s &= \Pi_1^2 + \Pi_2^2 + \Omega_1^2 + \Omega_2^2 + \Lambda_1^2 + \Lambda_2^2 \\
E_{co} &= 2e \left[A_t \left(\phi_2 \Pi_1 - \phi_1 \Pi_2 \right) + A_r \left(\phi_2 \Omega_1 - \phi_1 \Omega_2 \right) + A_z \left(\phi_2 \Lambda_1 - \phi_1 \Lambda_2 \right) \right]
\end{aligned}
$$

$$+e^2 \left(A_t^2 + A_r^2 + A_z^2 + \frac{A_\varphi^2}{\rho^2} \right) (\phi_1^2 + \phi_2^2)$$

$$E_{em} = \frac{1}{2} \left(|\vec{B}|^2 + |\vec{E}|^2 \right)$$

$$E_v = a \left(\phi_1{}^2 + \phi_2{}^2 \right) + b \left(\phi_1{}^2 + \phi_2{}^2 \right)^2 + c \left(\phi_1{}^2 + \phi_2{}^2 \right)^3$$

$$E_t = E_s + E_{co} + E_{em} + E_v.$$

The energy associated with any of these E_x, is then

$$E = \int \rho \, d\rho \, dz \, E_x. \tag{7.31}$$

We compute the total charge Q, where the charge density ρ_c is (ρ is just a coordinate)

$$\rho_c = 2e \left(\phi_2 \Pi_1 - \phi_1 \Pi_2 \right) + 2e^2 \left(\phi_1^2 + \phi_2^2 \right) A_t, \tag{7.32}$$

such that the total charge on the grid is the integral

$$Q = \int_0^{\rho_{max}} \int_{z_{min}}^{z_{max}} \rho \, d\rho \, dz \left[2e \left(\phi_2 \Pi_1 - \phi_1 \Pi_2 \right) + 2e^2 \left(\phi_1^2 + \phi_2^2 \right) A_t \right]. \tag{7.33}$$

7.2 Initial Data

The constraint on the initial data

$$\vec{\nabla} \cdot \vec{E} = \rho_c \tag{7.34}$$

(The usual factor of 4π is absent because of the convention used. Because the current density j^μ has been defined as $\nabla_\lambda F^{\lambda\mu}$ instead of $\nabla_\lambda F^{\lambda\mu}/(4\pi)$, the differential form of Gauss' law lacks the 4π.) yields

$$\vec{\nabla} \cdot \vec{E} = \rho_c$$

$$\frac{1}{\rho} \left(\rho E_\rho \right)_{,\rho} + \frac{1}{\rho} \left(E_\phi \right)_{,\phi} + \left(E_z \right)_{,z} = \rho_c$$

$$\frac{1}{\rho} \left(\rho C_1 - \rho B_2 \right)_{,\rho} + \left(D_1 - B_3 \right)_{,z} = \rho_c$$

$$\frac{1}{\rho} \left(\rho C_1 - \rho^2 \tilde{B}_2 \right)_{,\rho} + \left(D_1 - B_3 \right)_{,z} = \rho_c.$$

This constraint, as well as the choice of gauge

$$\nabla_\mu A^\mu = 0, \tag{7.35}$$

must be satisfied at the initial time. In our variables, these constraints take the form is

$$B_1 = \rho \tilde{C}_2 + D_3 + 2\tilde{A}_\rho \tag{7.36}$$

$$\frac{1}{\rho} \left(\rho C_1 - \rho^2 \tilde{B}_2 \right)_{,\rho} + \left(D_1 - B_3 \right)_{,z} = \rho_c. \tag{7.37}$$

To satisfy the gauge constraint, we can use Equation (7.36) itself to set B_1 after arbitrarily specifying A_ρ and A_z which fix the right hand side of the Equation (7.36. However, Equation (7.37) is a differential equation which must be solved and it is not immediately clear how to satisfy this equation in general. Solving this equation is analogous to having to solve $\nabla^2 \Phi = -\rho_c$ if we were in the Coulomb gauge. In the next section, a method is detailed which solves this problem.

7.3   York Procedure

In this section I use a procedure outlined by York in [96] to satisfy Equation (7.34). Beginning with the constraint

$$\vec{\nabla} \cdot \vec{E} = \rho_c, \tag{7.38}$$

assume the form for the electric field

$$\vec{E} = \vec{E}^T + \vec{\nabla} U(\rho, z) \tag{7.39}$$

so that

$$\vec{\nabla} \cdot \vec{E}^T = 0 \tag{7.40}$$

and the constraint is then

$$\nabla^2 U(\rho, z) = \rho_c. \tag{7.41}$$

The problem is now reduced to specifying $\vec{E}^T$ such that it is transverse, and solving for U. Because $\vec{E}^T$ represents freely specifiable initial radiation, we are free to set it to zero. Once we solve for U, we can then reconstruct $\vec{E}$ using

$$\vec{E} = \vec{\nabla} U. \tag{7.42}$$

Reconstructing $\vec{E}$, we have

$$E_z = U_{,z} \tag{7.43}$$

$$E_\rho = U_{,\rho} \tag{7.44}$$

$$E_\varphi = \frac{1}{\rho} U_{,\varphi} = 0. \tag{7.45}$$

Using identities (7.30), we can express all this in terms of the variables we are using

$$E_z = D_1 - B_3 = U_{,z} \tag{7.46}$$

$$E_\rho = C_1 - \rho \tilde{B}_2 = U_{,\rho} \tag{7.47}$$

$$E_\varphi = -\rho^2 \tilde{B}_4 = 0. \tag{7.48}$$

Finally, we have initial data which solves the constraints

$$B_1 = \rho \tilde{C}_2 + D_3 + 2\tilde{A}_\rho \tag{7.49}$$

$$B_2 = \frac{1}{\rho} (C_1 - U_{,\rho}) \tag{7.50}$$

$$B_3 = D_1 - U_{,z} \tag{7.51}$$

$$B_4 = 0, \tag{7.52}$$

where $U(\rho, z)$ satisfies

$$\nabla^2 U(\rho, z) = \frac{1}{\rho} (\rho U_{,\rho})_{,\rho} + U_{,zz} = \rho_c. \tag{7.53}$$

I have implemented a solver to find the solution U for general initial data using both a LCS and FAS multigrid solver as described by [12]. The solver has a fixed outer boundary condition on U, and implements a quadratic fit at the axis as described in Section 7.6.

7.4 Tests in Cylindrical Symmetry

Here I present evidence that a one-dimensional version of this code works. The code assumes vanishing z derivatives in the equations of motion and hence restricts the two-dimensional grid (ρ, z) to a one-dimensional ρ grid. As demonstration that the code correctly models a scalar field coupled to electromagnetism, I pick initial data such that

$$\begin{aligned}
\phi_1 &\neq 0 & \dot{\phi}_1 &= 0 \\
\phi_2 &\neq 0 & \dot{\phi}_2 &= 0 \\
A_t &\neq 0 & \dot{A}_t &= 0 \\
A_\rho &\neq 0 & \dot{A}_\rho &= 0 \\
A_z &\neq 0 & \dot{A}_z &= 0 \\
A_\varphi &\neq 0 & \dot{A}_\varphi &= 0.
\end{aligned} \tag{7.54}$$

With charge $e = 0.2$, the model is fully coupled and hopefully testing the code for this initial data is representative.

I run the model with Courant factor $\lambda = 1/5$ with some dissipation ($\epsilon = 0.5$) (see Section 2.8 for a description of Courant factor and dissipation). All fields initially have amplitudes within a factor of two of each other and, with $e = 0.2$, the behavior of the fields remains smooth throughout the evolution. With $\rho_{\max} = 20$, and with a final run time of $t_{\max} = 80$, the evolution runs four crossing-times. The fields are initialized to Gaussian pulses whose radii are in the interval [4..8]. Hence, axis effects are expected to be significant around $4 \leq t \leq 8$ when the pulses first hit the axis. Likewise, outer boundary effects should first appear when $t \approx 14$ and then again at $t \approx 26$.
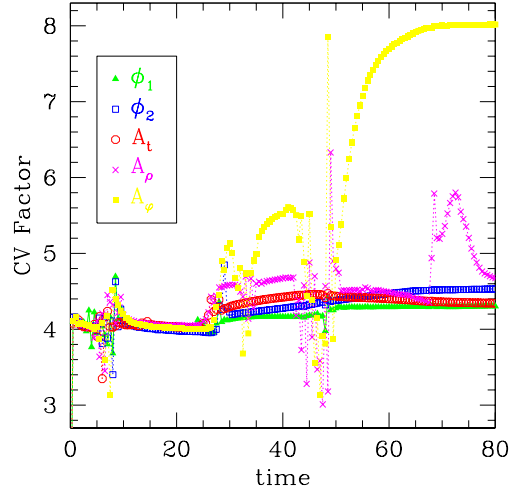
Figure 7.1: Convergence factors for the fundamental fields with $e = 0.2$ in cylindrical symmetry. A convergence factor of 4 indicates second order convergence in the grid spacing.

To evaluate the code's performance, I produce evolutions with resolutions $N_\rho = 513$, $N_\rho = 1024$, and $N_\rho = 2025$, where N_ρ is the number of grid points on the spatial grid.

Comparing these evolutions, I obtain the convergence factors displayed in Figure 7.1 (again, see Section 2.8 for a definition of convergence factor). Clearly at early times ($t < 4$) before the pulse hits the origin, the convergence factor is the expected value 4 for a code convergent to second order in the grid spacing. At later times, boundary effects come into play, and at that time it is expected that the Richardson expansion used to obtain the convergence factor may not hold. However, the code is still convergent in this regime.

Another worthwhile exercise in testing the code is to examine how well the constants of the motion are conserved. As the grid covers only a finite domain, conservation of the computed quantity is only expected when the fields have not propagated to the outer boundary.

The charge is examined first (see Fig. 7.2). Here I display the value of the integral of the charge density at the outermost grid point. This measures the amount of charge in the domain. Before the fields hit the outer boundary ($t < 20$), the total charge is well conserved. Further, as the resolution is increased, the total charge *converges to conservation*. By the phrase "converges to conservation", I mean that the variations of the quantity as a function of time decrease as the resolution is increased.

In Figure 7.4, I show the enclosed energy as a function of time. Again, the energy is roughly conserved until the fields hit the boundary. At that time, the energy decreases
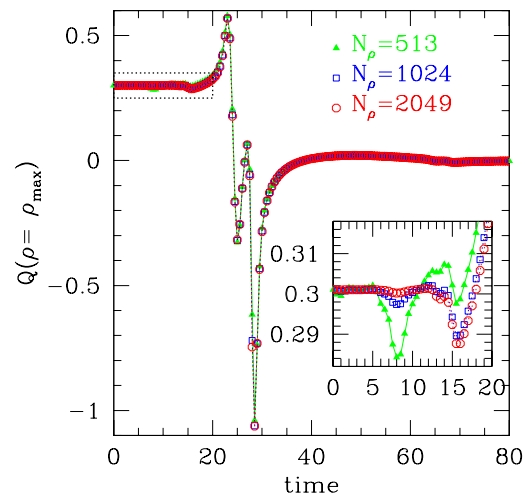
Figure 7.2: Total charge contained in grid as a function of time in cylindrical symmetry. Three resolutions are noted. The inset box displays the charge for the first crossing time and demonstrates that as the resolution is increased charge is better conserved. The prominent collapse of the charge beginning at $t \approx 20$ represents the fields hitting the outer boundary and charge transferred off the grid. The wild fluctuation of the total charge initially upward and then downward occurs as energy, and presumably charge, are encountering the outer-boundary. Hence the integral of the charge density meant to be taken "at infinity" outside any sources is now being taken within the region of maximum charge density and cannot be expected to be well behaved.
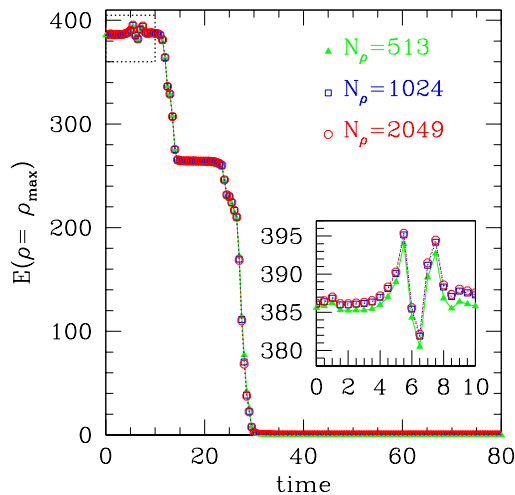
Figure 7.3: Incorrect total energy in grid as a function of time in cylindrical symmetry. The quantity is roughly conserved, however, as the inset boxes show, it converges to a non-conserved quantity. The correct computation appears in the next figure.

steadily until all the energy leaves the grid. It is interesting to examine Figure 7.3. Here, I plot the energy before a certain bug in the code was fixed. Though the energy appears conserved to within 2%, the inset box shows that the code is not converging to conservation (as noticed by Choptuik [27]). Figure 7.4 clearly shows the problem to be rectified.

As mentioned previously, this model has two constraints. Being a free evolution, these constraints are solved at the initial slice and are expected to be obeyed throughout the evolution to second order in the grid spacing [23].

In Fig. 7.5, the $l2$ norm of the residual of the gauge constraint is displayed as a function of time. As the pulse evolves through the origin, the norm grows and then subsides as the pulse travels outward. In this regime, as expected, this norm converges to zero with resolution. At $t \approx 25$, the pulse is leaving the domain, and the residual of the constraint grows independent of the grid spacing. These same features are evident in Fig. 7.6 where the norm of the $\vec{\nabla} \cdot \vec{E}$ constraint residual is displayed.

In the next graph, Fig. 7.7, I examine the possibility of using the gauge constraint to evolve A_t. Qualitatively, convergence and energy and charge conservation remain quite similar. However, the constrained evolution appears unstable as demonstrated by the increasing norm of the residual. Likewise, the norm of the scalar field grows at late time after the initial pulse has left the grid. The norm of the residual for the free evolution is observed to decay quickly at late times, providing evidence for stability.
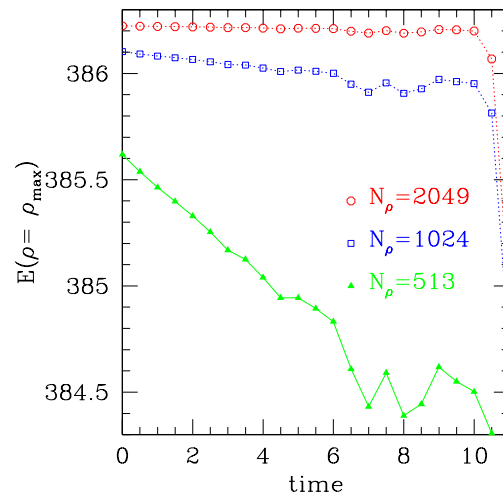
Figure 7.4: Corrected total energy in grid as a function of time in cylindrical symmetry. It converges to conservation.
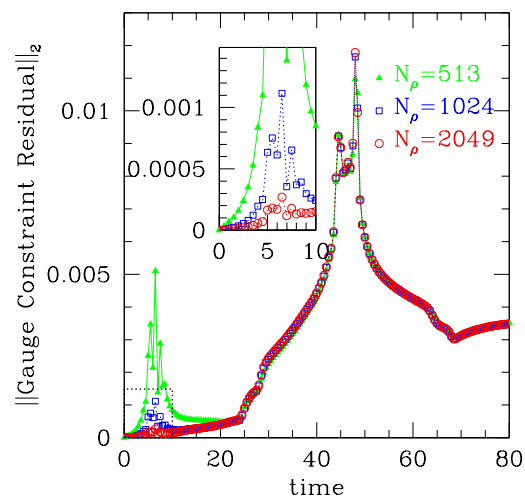

Figure 7.5: Norm of the gauge constraint residual with time in cylindrical symmetry. Before the fields hit the boundary, this error is convergent with resolution. Afterwards, the error is independent of the grid spacing with the possibility of an instability.
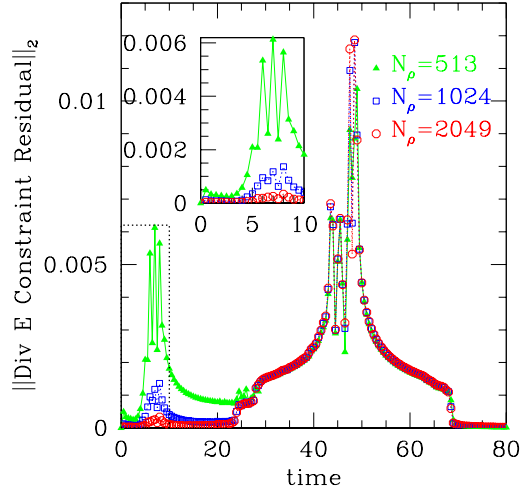
Figure 7.6: Norm of the $\vec{\nabla} \cdot \vec{E}$ constraint with time in cylindrical symmetry. Similar to the gauge constraint, before the fields hit the outer boundary, convergence to zero is apparent.

7.5 Tests in Axisymmetry

Being two-dimensional, tests of the axisymmetric code necessarily require more resources and time. Tests similar to those presented above are computed here for comparable initial data (i.e. Equations (7.54) hold again at the initial time). Again, the Courant factor is $\lambda = 0.2$, the charge $e = 0.2$, and the level of dissipation is $\epsilon = 0.5$.

The components of the scalar field are initialized to spherically symmetric Gaussian pulses

$$\Theta(\rho, z) = A e^{-\left(\rho^2 + z^2 - R_0\right)^2 / \Delta^2} \tag{7.55}$$

with R_0 either 5 and 7 and constants A and Δ arbitrary. The grid is rectangular with bounds $(0, -20) \to (\rho, z) \to (20, 20)$. Hence, the fields hit the origin at $t \approx 6$, and first hit the outer boundary at $t \approx 14$.

Figures 7.8 and 7.9 show the convergence factors computed at low and high resolutions, respectively. That these graphs show a tendency toward the value 4 with increasing resolution indicates the code to be second-order convergent. Both figures show that the convergence factors decrease for early times, though the higher resolution graph remains closer to 4. The behavior of the convergence factor appears to generally behave this well with the possible explanation that until a sufficient resolution is reached, the solution is insufficiently smooth to extract much useful information from the Richardson extrapolation. As the resolution is increased, behavior at the axis increases significantly making it more reasonable to compare runs at different (but still high) resolutions.
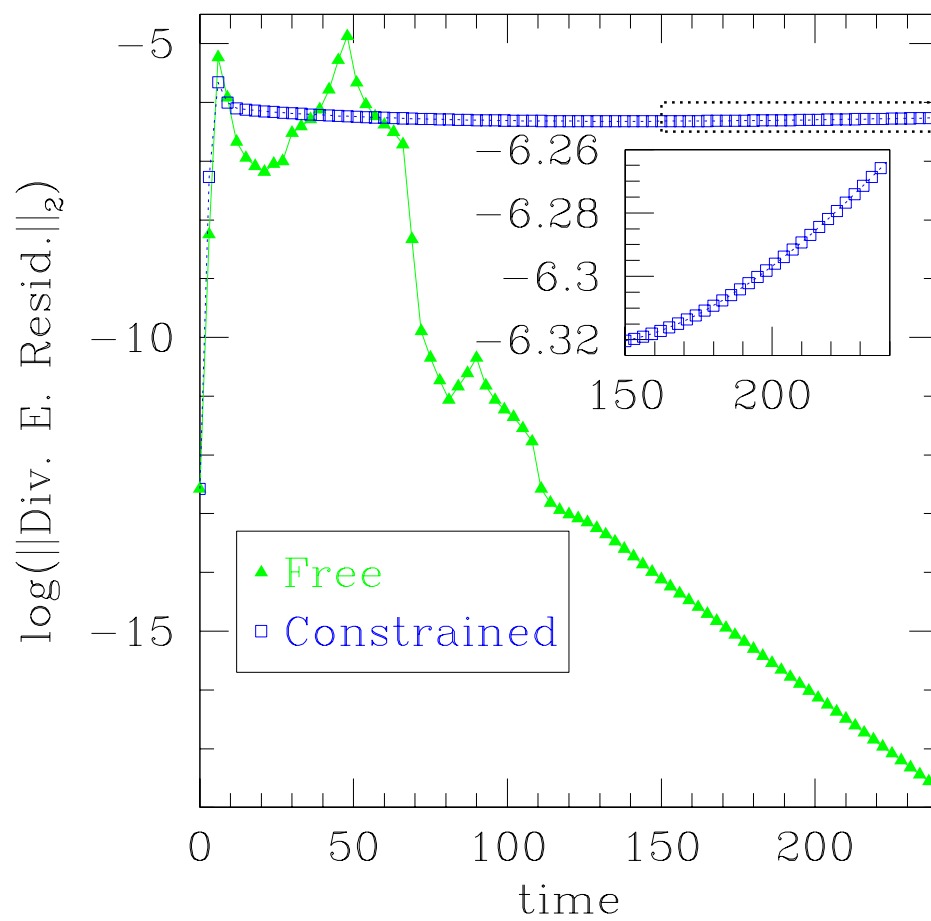
Figure 7.7: Test for stability with $N_\rho = 513$ in cylindrical symmetry. The triangles denote the log of the norm of the residual of the $\vec{\nabla} \cdot \vec{E}$ constraint for the free evolution. The squares denote the same quantity calculated from an evolution with the same parameters but where A_t is updated using the gauge constraint.
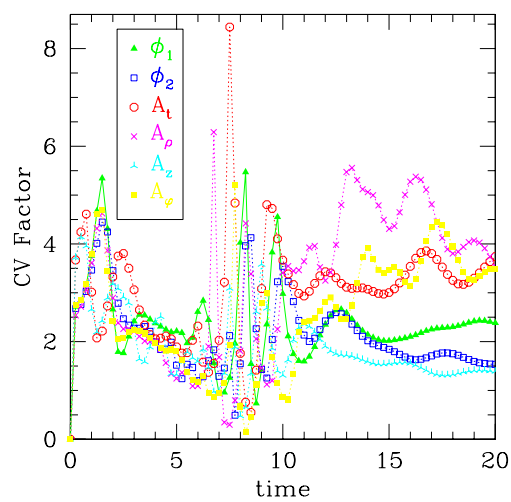
Figure 7.8: Convergence factors for the fundamental fields with $e = 0.2$ in axisymmetry.
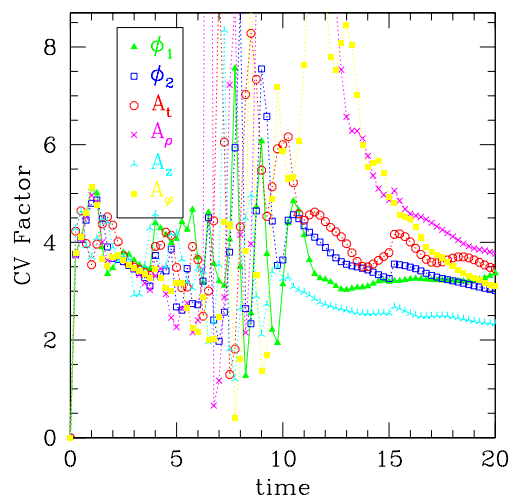
Figure 7.9: Convergence factors of the fundamental fields for higher resolution than Figure 7.8 with $e = 0.2$ in axisymmetry.

Figure 7.10 displays the total charge as a function of time for various resolutions. For times before the fields have hit the outer boundary, the code converges to conservation of charge.

Figures 7.11 and 7.12 display the total energy versus time for the code before and after the previously mentioned bug was fixed. The corrected energy output converges to conservation for times $t < 15$.

Examining the constraints, Figure 7.13 shows the $l2$ norm of the residual of the evolution equation for A_t for the case that the evolution uses the gauge constraint to solve for A_t. The norm appropriately decreases for increasing resolution.

The norm of the $\vec{\nabla} \cdot \vec{E}$ constraint is plotted in Figure 7.14. Once again, the code appears consistent with the constraints.

Finally, it appears the issue of stability of the free versus constrained evolution remains the same as in cylindrical symmetry. Similar to Figure 7.7, the Figure 7.15 indicates similar results for the norm of the constraint. Hence, it seems the constrained evolution is, in fact, unstable, while the free evolution is stable.

7.6 Comparison of FAS and LCS Schemes in Multigrid for Axisymmetry

Here I compare a *linear correction scheme* (LCS) multigrid method with a *full approximation storage scheme* (FAS) to solve Equation (7.34) [12, 13].

Given a problem with linear operator L (L with no superscripts represents a differential equation to be solved, whereas L^h represents an operator which acts on field to produce a new field and will generally only appear on the right hand side of an equation):

$$Lu(\rho, z) = f(\rho, z), \qquad (7.56)$$

the Linear Correction Scheme (LCS) solves this problem on a given grid of grid spacing h and given any initial guess u_0^h by solving a problem on a coarser grid with grid spacing $2h$.

Specifically, it solves the equation

$$Lv^{2h} = I_h^{2h} f^h - I_h^{2h} L^h u^h \qquad (7.57)$$

and then corrects u_0^h via

$$u_{i+1}^h = u_i^h + I_{2h}^h v^{2h}. \qquad (7.58)$$

These two equations define the LCS scheme. The FAS scheme is sometimes necessitated because the differential operator L is not generally linear. We can think of the FAS
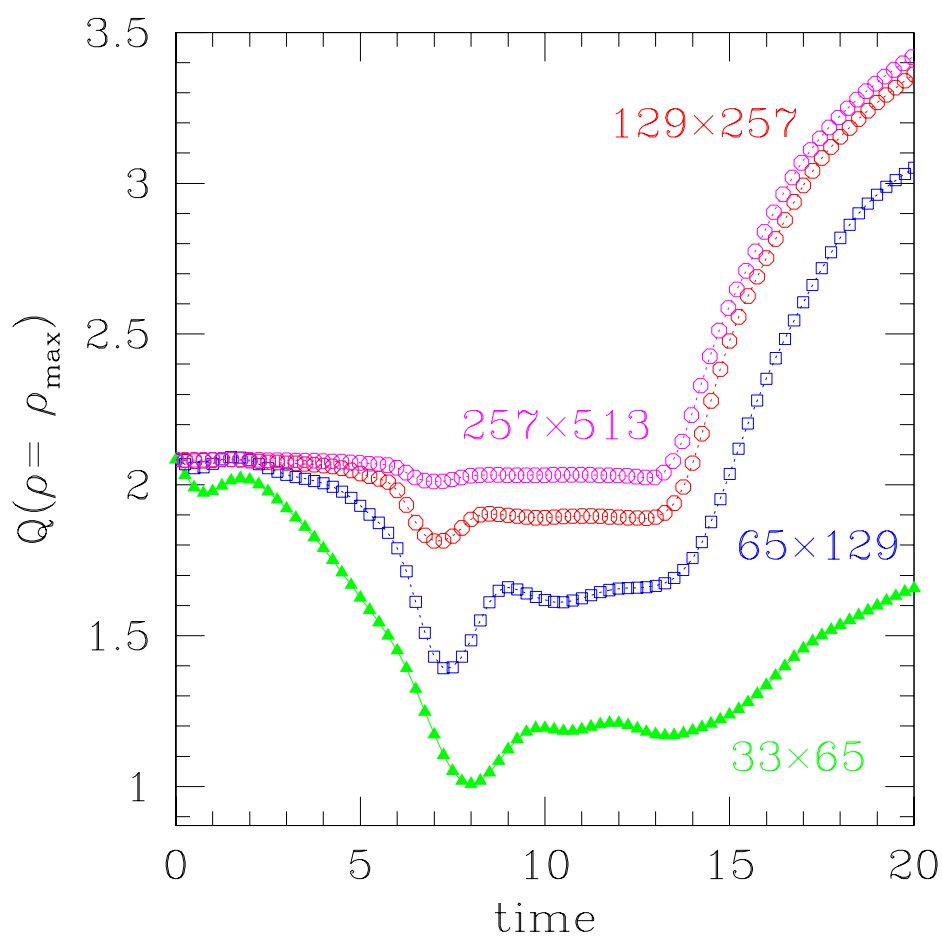
Figure 7.10: Total charge on grid as a function of time in axisymmetry. The rise of the total charge at $t \approx 15$ corresponds to the time at which the fields hit the outer boundary. Comparing to the corresponding figure for cylindrical symmetry, Fig. 7.2, this effect seems transitory as the charge leaves the grid. In other words, were the evolution to proceed longer, the charge would decrease to zero after the fields leave the grid.
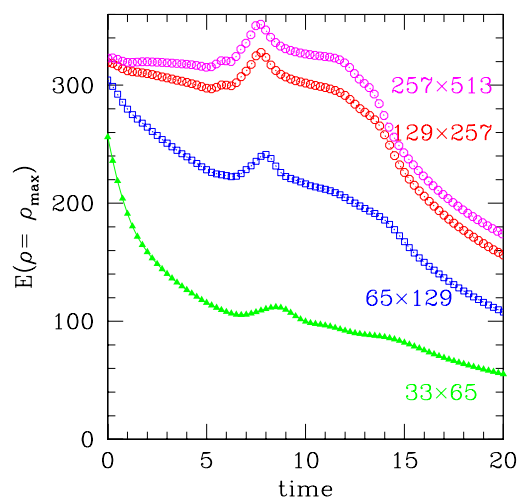
Figure 7.11: Total energy of the axisymmetric code before the code was fixed.
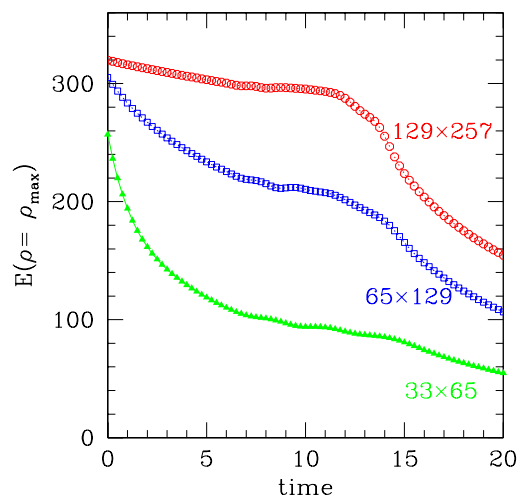
Figure 7.12: Total energy for the corrected code. The energy converges to conservation. For $t > 15$, energy is leaving the grid as would be expected.
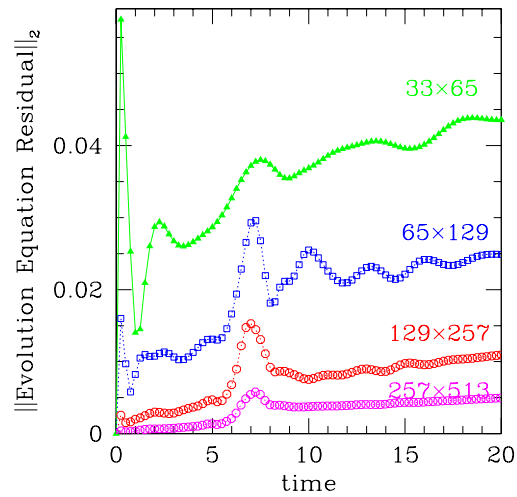
Figure 7.13: Norm of the evolution equation residual for A_t for the axisymmetric code. Here, the code is using the gauge constraint to evolve A_t, so this residual indicates how well the evolution is obeying the evolution equation. Because the norm decreases with increasing resolution, the code appears consistent with the evolution equation.
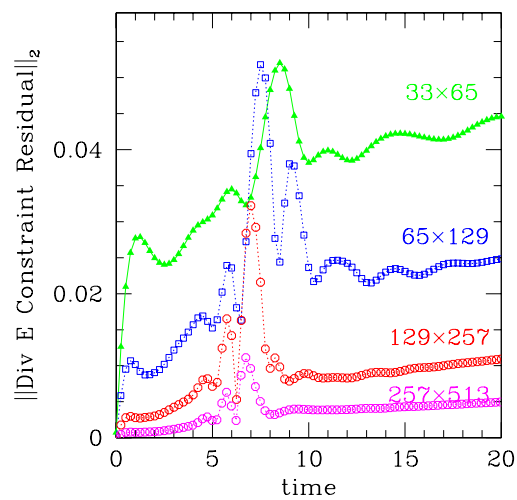
Figure 7.14: The norm of the $\vec{\nabla} \cdot \vec{E}$ constraint for the axisymmetric code. Because the norm decreases with increasing resolution, the evolution appears consistent with the constraint.
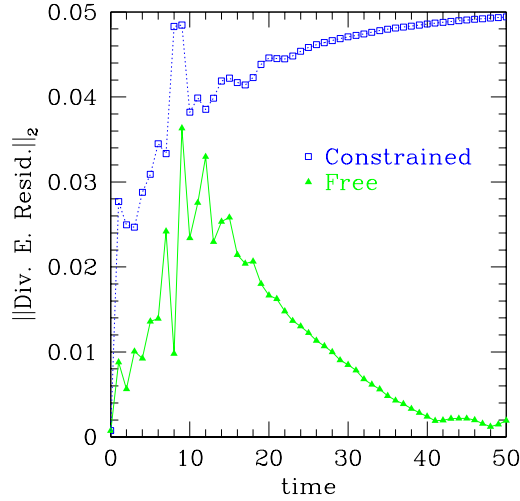
Figure 7.15: Comparison of the norm of the constraint for the free and the constrained cases. The constrained case represents when the code uses the gauge constraint to evolve A_t while free indicates that only evolution equations are used. As with the cylindrical code, the free code appears stable while the constrained code appears unstable. Compare to Figure 7.7.

scheme as a generalization of the LCS scheme. Once again we look for a correction such that we satisfy

$$L\left(u^h + v^h\right) = f^h, \tag{7.59}$$

but because L is not linear we can not separate the term on the left side. Instead, we subtract $L^h u^h$ from (7.59) to get

$$L\left(u^h + v^h\right) - L^h u^h = f^h - L^h u^h, \tag{7.60}$$

where the left side is now the effective correction on the fine grid. The right side of this is smooth after a few relaxation sweeps, and so we can transfer the left side to a coarse grid

$$Lu^{2h} - L^{2h} I_h^{2h} u^h = I_h^{2h} \left(f^h - L^h u^h\right), \tag{7.61}$$

where the coarse grid u^{2h} is just

$$u^{2h} = I_h^{2h} u^h + v^{2h}. \tag{7.62}$$

The FAS equations then are

$$Lu^{2h} = \left(I_h^{2h} f^h - I_h^{2h} L^h u_i^h\right) + L^{2h} I_h^{2h} u_i^h \tag{7.63}$$

and

$$u_{i+1}^h = u_i^h + I_{2h}^h \left(u^{2h} - I_h^{2h} u_i^h\right). \tag{7.64}$$

In the case that L is linear, these equations are the same. However, in practical application of these methods, implementation of non-homogeneous boundary conditions requires careful attention. For the case of axisymmetry, I enforce a quadratic fit at the axis on the field u via the operator Q

$$Q^h u^h \Rightarrow u^h(\rho = 0, z) = \frac{4}{3} u^h(d\rho, z) - \frac{1}{3} u^h(2d\rho, z) \tag{7.65}$$

and hence it only acts on the inner boundary of its argument. In any given relaxation sweep, this quadratic fit is applied after the sweep. Another operator which I will use is

$$D^h u^h \rightarrow u^h(\rho = 0, z) = u^h(\rho = \rho_{\max}, z) = u^h(\rho, z = z_{\min}) = u^h(\rho, z = z_{\max}) = 0 \tag{7.66}$$

which simply forces the field to be zero everywhere on the boundary.

Solving Poisson's equation

$$\nabla u = f \tag{7.67}$$

where f is some charge density, we look for an appropriate FAS scheme which will yield the same results as the LCS scheme. I find that the equations

$$Lu^{2h} = I_h^{2h} \left(D^h \left[f^h - L^h u_i^h \right] \right) + L^{2h} Q^{2h} I_h^{2h} u_i^h \tag{7.68}$$

and

$$u_{i+1}^h = u_i^h + I_{2h}^h \left(u^{2h} - Q^{2h} I_h^{2h} u_i^h \right), \tag{7.69}$$

where u^{2h} is initialized to

$$u^{2h} = Q^{2h} I_h^{2h} u^h \tag{7.70}$$

recovers the same result as the LCS scheme. The placement of the quadratic fit operators is the only distinction of this scheme worthy of discussion.

That this FAS scheme recovers the results of the LCS scheme can be seen by comparing the two scheme's equations, Equation (7.57) and Equation (7.68). Subtracting $L^{2h} Q^{2h} I_h^{2h} u_i^h$ from each side of Equation (7.68), we have

$$
\begin{aligned}
Lu^{2h} - L^{2h} Q^{2h} I_h^{2h} u_i^h &= I_h^{2h} \left(D^h \left[f^h - L^h u_i^h \right] \right) \\
L \left(u^{2h} - Q^{2h} I_h^{2h} u_i^h \right) &= I_h^{2h} \left(D^h \left[f^h - L^h u_i^h \right] \right).
\end{aligned} \tag{7.71}
$$

From this, we see that the "effective" correction on the coarse grid, namely $u^{2h} - Q^{2h} I_h^{2h} u_i^h$, will now explicitly satisfy a quadratic fit after any relaxation sweep over u^{2h} because of the imposition of the operator Q^{2h} on the restriction of u^h. The difference between two functions satisfying a quadratic fit also satisfies a quadratic fit. This is just what is accomplished in the LCS scheme by relaxing just the correction v^{2h}.

Further, it should be clear that the term on which L^{2h} acts in Equation 7.68 must be identical to the term used to compute the correction in Equation (7.69) and the initialization

in Equation (7.70). That no quadratic operator should act on the first term on the righthand side of Equation (7.68) can be seen by again comparing to the LCS scheme where no such operator occurs in the corresponding term. Likewise, no quadratic fit operator acts on the correction in Equation (7.69).

A couple of limits help show the validity of this scheme. Call the initialization of the coarse grid solution $u_0^{2h} = Q^{2h} I_h^{2h} u^h$, and consider the case $u_i^h(\rho, z) = 0$. Then we have

$$Lu^{2h} = I_h^{2h} D^h f^h \tag{7.72}$$

and

$$u_{i+1}^h = I_{2h}^h u^{2h} \tag{7.73}$$

This is clearly equivalent to the LCS scheme.

Now consider the case where u_i^h is the exact solution to the finite difference equation.

$$Lu^{2h} = L^{2h} \left(Q^{2h} I_h^{2h} u_i^h \right) \tag{7.74}$$

so that

$$u_{i+1}^{2h} = u_i^{2h}. \tag{7.75}$$

In that case, the correction is zero and we get the correct result

$$u_{i+1}^h = u_i^h. \tag{7.76}$$

An example of the implementation of this scheme in pseudo-code would likely be helpful.

```
Initialize fine grid solution u^M            → e.g. u^M(ρ, z) = 0
Allocate grids and storage m = M, 1, −1      → h, 2h, 4h, . . .
Loop m = M, 2, −1                            → loop down
        Relax u^m preswp times
        Initialize f^{m−1} = I_m^{m−1} (D^m [f^m − L^m u_i^m]) + L^{m−1} Q^{m−1} I_m^{m−1} u_i^m
        Initialize u^{m−1} = Q^{m−1} I_m^{m−1} u^m
End Loop Down


Solve Coarsest Grid Lu^1 = f^1


Loop m = 2, M, 1                                   → loop up to fine grid
        Update u^m = u^m + I_{m−1}^m (u^{m−1} − Q^{m−1} I_m^{m−1} u_i^m)
```

```
        Relax u^m pstswp times
End Loop Up
```

Chapter 8

Monopole Pair Nucleation

This work modeling texture collapse in flat space was done with Hirschmann [56].

8.1 Introduction

An outstanding cosmological problem is explaining the homogeneity and isotropy of the universe on large scales while allowing for sufficient inhomogeneity and anisotropy on small scales to account for the existence of galaxies, stars, and, of course, us. Several mechanisms for this have been suggested. One of these is the inflationary scenario. An alternative which has also received considerable attention is the idea that the production of topological defects via phase transitions in the early universe provided the density fluctuations which eventually led to galaxy formation and the like.

In general, defects result because of a spontaneously broken symmetry. If one begins with a set of fields, Φ^a, which possess a global symmetry G and interact via a potential $V(\Phi)$ which breaks G down to a subgroup H, the vacuum manifold is described by the quotient space G/H. Defects will arise in theories for which the vacuum manifold allows nontrivial homotopy groups $\pi_n(G/H)$ characterized by an integer n. For a given homotopy group $\pi_n(\mathcal{M})$, the homotopy groups serve to differentiate mappings from the n-dimensional sphere S^n into the manifold $\mathcal{M}$ [88].

For different values of n, one gets different types of defects. Domain walls arise for $n = 0$, global strings for $n = 1$, monopoles for $n = 2$, and textures for $n = 3$. At very early times, the universe is at a very high temperature so that, in general, the effective potential has a unique, symmetric vacuum state which does not allow defects. However, as the universe expands, it cools and passes through a symmetry breaking phase transition allowing for the possible formation of these defects. The vacuum manifold is no longer one state, but instead the degenerate vacuum states form a nontrivial manifold. The presence of these defects can then serve as gravitational seeds for structure formation, and hence the importance of understanding their dynamics.

Here, we will be interested in a particular texture model and its dynamics. As with all texture models in three spatial dimensions, the scalar field configuration is unstable and will tend to shrink or collapse. An interesting conjecture has recently been put forth on the collapse of various texture models. Sornborger *et al* [85] suggest that the nature of the various collapses can be categorized by whether the particular texture model allows more than one type of defect. In particular, models for which only π_3 is nontrivial (such as $SO(4)/SO(3)$) collapse in a similar (and, from their results, nearly indistinguishable) manner. On the other hand, models for which homotopy groups π_3 and π_2 are both nontrivial (such as $SO(3)/SO(2)$) should collapse in a qualitatively different manner, namely via the production of defects characterized by the other (non-π_3) nontrivial homotopy group. These authors provide numerical evidence for their conjecture, having evolved several texture models from similar initial conditions and examined the collapse process/products.

The results in [85] would appear to be in agreement with interesting experimental evidence in nematic liquid crystals. Chuang *et al* [21] induce phase transitions in a nematic liquid crystal described by a $SO(3)/SO(2)$ broken symmetry and produce textures. These textures, they claim, decay via the production of a monopole-antimonopole pair. However, later numerical work by Rhie and Bennett [72] with this model suggests that such pair production did not occur. Later still, Luo [58] suggests that the reason for the absence of pair production in the numerical simulations of Rhie and Bennett is that the initial configuration of their simulations does not correspond to that seen in the laboratory experiments of Chuang. Instead, he presents different initial data suggesting that this data should indeed nucleate monopoles.

In the following, I analyze the dynamics of collapsing Hopf textures, those textures occurring from the breaking of $SO(3)$ to $SO(2)$. The results verify aspects of all these earlier results and clarify the general picture. In the first section, I present the model, the evolution equations, and discuss the numerical approach. In subsequent sections, I consider the evolutions of a variety of initial data. These include a single monopole and a monopole-antimonopole pair which are evolved to demonstrate that the code can evolve these objects and to allow the identification of their presence or absence in later evolutions of texture collapse.

8.2   The Equations and Numerical Approach

The model we consider is described by the Lagrangian

$$\mathcal{L} = -\frac{1}{2}\Phi^a_{,\mu}\Phi^{a,\mu} - V(\mathbf{\Phi}) \tag{8.1}$$

where the potential $V(\mathbf{\Phi})$ is

$$V(\mathbf{\Phi}) = \gamma\left(\Phi^a\Phi^a - v^2\right)^2 \tag{8.2}$$

and Φ^a is a set of three scalar fields. The scalar fields thus transform under the global symmetry group $SO(3)$ with the potential breaking this down to $SO(2)$. The resulting vacuum manifold is $SO(3)/SO(2) = S^2$ for which the second and third homotopy groups are nontrivial. Thus this model allows both textures and global monopoles. The equations of motion are

$$\partial_\mu \partial^\mu \Phi^a = 4\gamma \Phi^a \left(\Phi^b \Phi^b - v^2 \right). \tag{8.3}$$

A trivial rescaling invariance $\Phi^a \to c\Phi^a$ allows us to set $\nu = 1$, leaving the model with one free, dimensionless parameter γ.

Following [85] we split the total energy density into three parts: the kinetic, gradient and potential energy densities defined as

$$\rho_k = \frac{1}{2} \left(\dot{\Phi}^a \dot{\Phi}^a \right), \tag{8.4}$$

$$\rho_g = \frac{1}{2} \left(\nabla \Phi^a \nabla \Phi^a \right), \tag{8.5}$$

$$\rho_v = \gamma \left(\Phi^a \Phi^a - 1 \right), \tag{8.6}$$

and the total energy density is

$$\rho_T = \rho_k + \rho_g + \rho_v. \tag{8.7}$$

This model also has a conserved topological charge. The monopole current associated with the charge density is

$$k_\mu = \frac{1}{8\pi} \epsilon_{\mu\nu\rho\sigma} \, \epsilon_{abc} \, \phi_\nu^a \, \phi_\rho^b \, \phi_\sigma^c, \tag{8.8}$$

where $\epsilon_{\mu\nu\rho\sigma}$ and ϵ_{abc} are purely antisymmetric tensors ("Levi-Civita" tensors) of rank 4 and 3 respectively. The conserved monopole charge is

$$Q = \int k_0 \, d^3x = \frac{1}{8\pi} \int d^3x \left(\epsilon_{ijk} \, \epsilon_{abc} \, \phi_{,i}^a \, \phi_{,j}^b \, \phi_{,k}^c \right), \tag{8.9}$$

the integral of the charge density k_0 [71].

Given appropriate initial conditions, these equations are now straightforward to integrate in Cartesian coordinates. Some particular initial data that has been suggested for texture collapse is

$$\Phi(\vec{x}) = \begin{pmatrix} \cos^2(\chi) + \left(2z^2/r^2 - 1\right) \sin^2(\chi) \\ 2\left(xz \sin^2(\chi)/r^2 + y \cos(\chi) \sin(\chi)/r\right) \\ 2\left(yz \sin^2(\chi)/r^2 - x \cos(\chi) \sin(\chi)/r\right) \end{pmatrix}, \tag{8.10}$$

where $r = \sqrt{x^2 + y^2 + z^2}$ is the usual spherical radial coordinate and where the boundary conditions on the radial function $\chi(r)$ are $\chi(r = 0) = 0$ and $\chi(r \to \infty) = \pi$. We will also consider another suggested form for the initial data which has toroidal symmetry.

It is worth noting that for this initial data, the initial total energy density is axisymmetric. For the particular case in which $\chi(r) = 2 \tan^{-1}(r)$, the initial energy is actually

spherically symmetric. In addition, one may expect this axisymmetry to be maintained during the evolution. We attempt to take advantage of this observation and cast the equations and this initial data into a manifestly axisymmetric form. In cylindrical coordinates (ρ, z, φ), we define new quantities

$$
\begin{aligned}
\Phi^+ &= \cos\varphi\, \Phi^2 + \sin\varphi\, \Phi^3 & (8.11)\\
\Phi^- &= \sin\varphi\, \Phi^2 - \cos\varphi\, \Phi^3 & (8.12)
\end{aligned}
$$

which, for the above initial data, can be seen to be manifestly axisymmetric. It is now a simple matter to get the equations of motion for $\Phi^\pm$. Using the equations of motion for Φ^a from Eq.(8.3) we find the equations for $\Phi^\pm$ to be

$$
\begin{aligned}
-\Phi^+_{,tt} &+ \frac{1}{\rho}\left(\rho\Phi^+_{,\rho}\right)_{,\rho} - \frac{1}{\rho^2}\Phi^+ + \Phi^+_{,zz} + \frac{2}{\rho^2}\Phi^-_{,\varphi} + \frac{1}{\rho^2}\Phi^+_{,\varphi\varphi} \\
&= 4\gamma\Phi^+\left(\Phi^b\Phi^b - v^2\right) & (8.13)\\
-\Phi^-_{,tt} &+ \frac{1}{\rho}\left(\rho\Phi^-_{,\rho}\right)_{,\rho} - \frac{1}{\rho^2}\Phi^- + \Phi^-_{,zz} - \frac{2}{\rho^2}\Phi^+_{,\varphi} + \frac{1}{\rho^2}\Phi^-_{,\varphi\varphi} \\
&= 4\gamma\Phi^-\left(\Phi^b\Phi^b - v^2\right) & (8.14)
\end{aligned}
$$

with

$$
\Phi^b\Phi^b = \Phi^1\Phi^1 + \Phi^+\Phi^+ + \Phi^-\Phi^-. \qquad (8.15)
$$

Since the evolution will remain axisymmetric, we can discard the terms which have derivatives with respect to φ.

This simplification of the problem from 3D to 2D results in enormous gains from a computational perspective and allows us significant improvement in our potential resolution of dynamic features in the evolution. However, in our code development and tests, we found it very useful to also have a 3D code with which to compare our 2D results and results of earlier investigators.

For those reasons, we have implemented both a 3D code and a 2D axisymmetric code using a second order Crank-Nicholson finite difference scheme implemented with RNPL [63]. Out-going radiation conditions based on approximate spherical propagation as $r \to \infty$ are imposed

$$
r\Phi^a = f(t - r), \qquad (8.16)
$$

for some function f. This condition is very effective in limiting reflection from the boundaries. We have verified that these codes are fully convergent and that they are stable for many crossing times.

8.3 Single Monopole

As stated in the introduction, we want to evolve a collapsing Hopf texture and examine the possible nucleation of monopole-antimonopole pairs. However, in order to understand the behavior of any nucleated monopoles modeled by these codes, we first examine the evolution of initial data explicitly containing a monopole. Using the standard hedgehog ansatz, we can represent a monopole of unit charge at the origin by

$$\Phi\left(\vec{x}\right) = \frac{f\left(r\right)}{r} \begin{pmatrix} x \\ y \\ z \end{pmatrix}, \tag{8.17}$$

where $f\left(r = 0\right) = 0$ and $f\left(r \to \infty\right) = 1$. Instead of solving for $f\left(r\right)$ such that the monopole is static, we choose

$$f(r) = \frac{1}{2}\left[1 + \tanh\left(\frac{r - R}{\beta}\right)\right] \tag{8.18}$$

for arbitrary constants R and β, and evolve the configuration.

The results are shown in Figure 8.1. The energy is initially conserved, but quickly energy leaves the grid because the monopole is settling into its static state by radiating away excess potential energy. The charge remains approximately one, showing the monopole is stable for γ sufficiently nonzero. The graph shows that for $\gamma \approx 0$, the charge smoothly transitions to zero.

It is important to note that the decrease in energy shown in Figure 8.1 does not represent failure of the code to conserve energy. Instead, this energy is being radiated away as the monopole settles down to the static case. The radiated energy comes from the large core region of the monopole. This core region is larger than that for a static monopole and hence has significantly more potential energy. This potential energy is not trapped. The evolution proceeds to decrease the potential energy as would be expected. However, not all the potential energy can leave because of the topological aspects of the monopole. Somewhere in the core the fields Φ^a must all vanish, and hence the potential will be non-zero there. To decrease the potential energy trapped in the monopole as much as possible, the fields would vanish at the center of the core and immediately go to their vacuum value. However, this would introduce a large amount of gradient energy. A static monopole is then reached when the potential energy reduction is balanced with the increase in gradient energy acquired by the shrinking monopole.

The static monopole can be found explicitly by assuming the ansatz (8.17), substituting this ansatz into the equations of motion (8.3), and solving numerically the ODE

$$\tilde{f}'' + \frac{2\tilde{f}}{r} - \frac{2\tilde{f}}{r^2} = 4\gamma\tilde{f}\left(\tilde{f}^2 - 1\right), \tag{8.19}$$
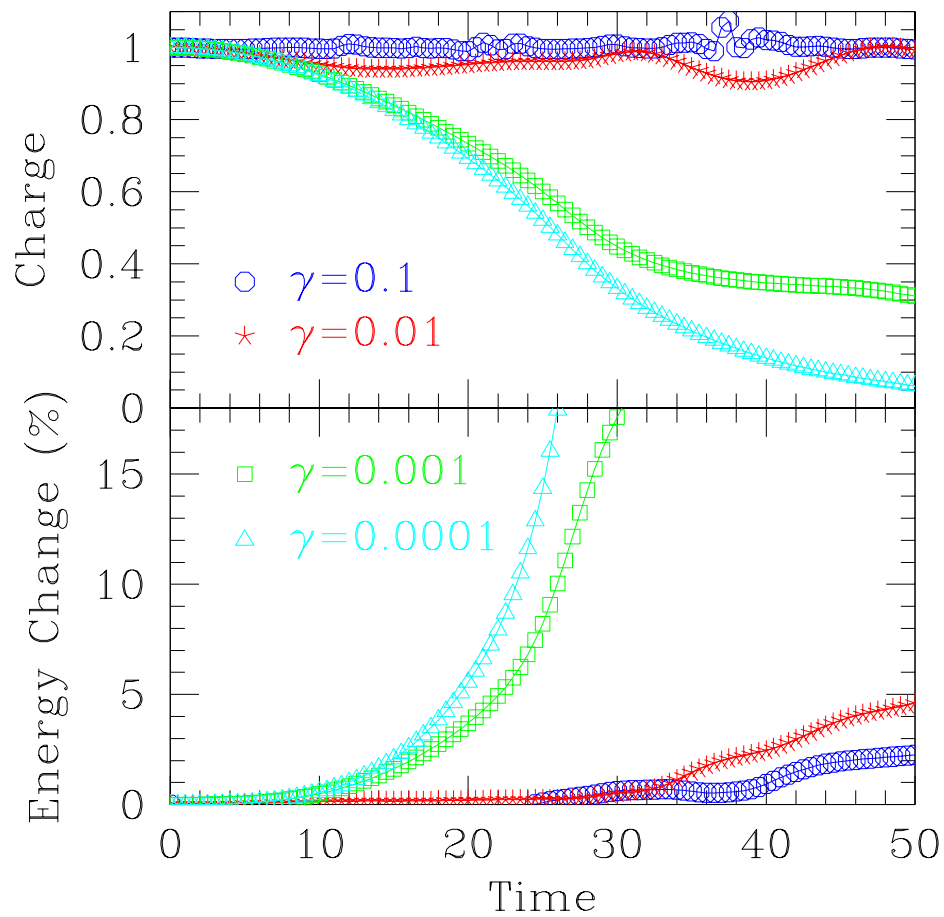
Figure 8.1: Changes in energy and charge as a function of time for a single monopole. Energy is seen to be conserved for early times, but the monopole is shedding potential energy as it settles toward the static monopole. The charge is plotted, and for $\gamma \geq 0.01$ is seen to be conserved at unity. The oscillation of the charge is presumably due to the irregularity of the static monopole getting "smoothed" by the code repeatedly. These evolutions were run on a 257x513 grid.
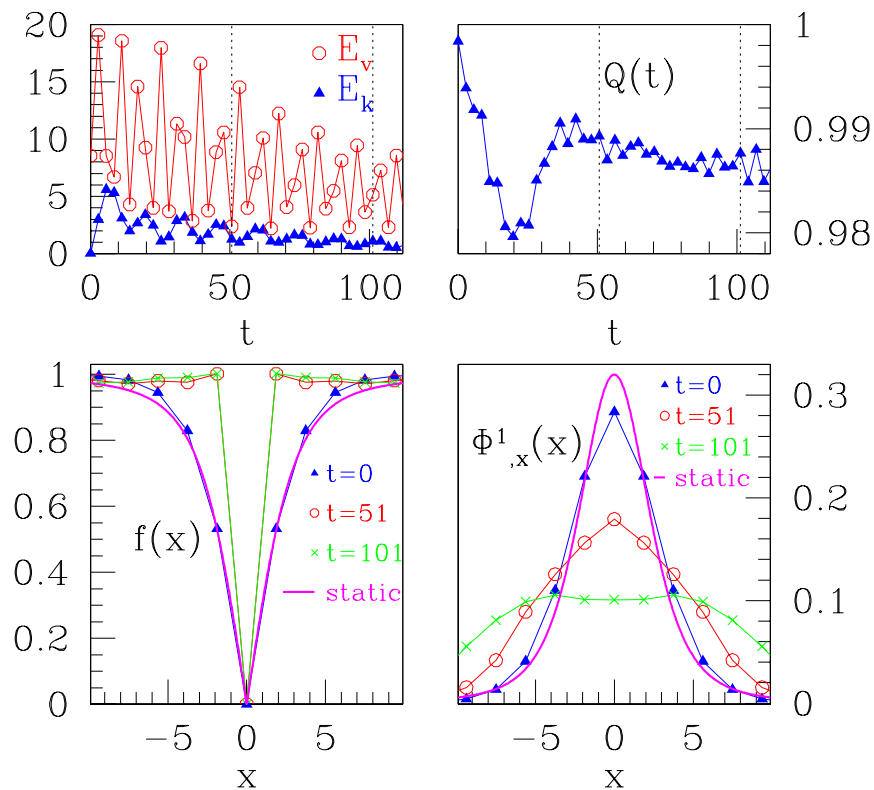
Figure 8.2: Long term behavior of a single monopole in the 3d code. A single monopole is evolved which is close to the static solution. The monopole sits at the origin of the coordinates. The upper left graph shows the potential and kinetic energies versus time. This shows that the monopole is settling down to a state with zero kinetic energy. The upper right graph shows the total charge which oscillates near unity and settles down. The bottom left graph shows the effective $f = |\Phi|$ versus the coordinate x (f is spherically symmetric and so the choice of x is arbitrary) for various times. The bottom right graph shows the field $\Phi^1{}_{,x}$ versus x at the same times as f is shown next to it. For both the bottom graphs, the static fields as obtained from solving an ODE are shown in heavy lines. The bottom right graph shows the field becoming smooth during the evolution which results in the effective f becoming as shown in the graph.

letting $\tilde{f}(r)$ describe the static monopole. Doing so, you find that $\tilde{f}(r)$ goes as r near $r = 0$ and $\tilde{f}'(r)$ goes as a constant (see Fig. 8.2). Now consider one of the fields, say Φ^1, near $r = 0$. This field looks like $|x|$ near $x = 0$, and hence its derivative is not smooth at all. The code though, being numerical, is forced to assume some level of smoothness dependent on the spatial resolution. Thus, as shown in the bottom right graph of Fig. 8.2, the derivative $\Phi^1{}_{,x}$ becomes smooth in time. The effective $f = |\Phi|$ therefore does not settle down to the static $\tilde{f}$, as shown in the lower left of Fig. 8.2.

These simulations have been done with time symmetric initial data. However, we have also implemented a Galilean boost of the monopole by giving it an initial velocity in some direction along an axis. The monopole is seen traversing the numerical domain. That we can evolve a monopole for many crossing times and also boost it while retaining its particle nature, provides further evidence that the global monopole is stable to perturbations as discussed in [9, 34, 73].

8.4   Monopole-Antimonopole Pair

An anti-monopole is just a reflection of the monopole ansatz. Thus, it takes the form

$$\Phi\left(\vec{x}\right) = \frac{f(r)}{r} \begin{pmatrix} x \\ y \\ -z \end{pmatrix}. \tag{8.20}$$

We can then translate the monopole up and the antimonopole down some distance L to get the solution for a monopole-antimonopole pair located on the z axis

$$\Phi\left(\vec{x}\right) = \frac{f^{\pm}}{x^2 + y^2 + \left(|z| - L\right)^2} \begin{pmatrix} x \\ y \\ |z| - L \end{pmatrix}, \tag{8.21}$$

where $f^{\pm}$ is

$$f^{\pm} = \frac{1}{2}\left[1 + \tanh\left(\frac{\sqrt{x^2 + y^2 + \left(|z| - L\right)^2} - R}{\beta}\right)\right]. \tag{8.22}$$

At $z = 0$, $\Phi_3 \to L$ from positive and negative z, and, though not differentialable at $z = 0$, it is continuous. This non-smoothness gets smoothed quickly by the numerical evolution and does not appear to affect the evolution of the pair significantly.

We evolve this pair configuration for $L = 15$ and show the resulting charge in Figure 8.3. The total charge of the spacetime remains essentially zero throughout the evolution, so we display only the charge occurring in the half of the space which initially holds the monopole. Hence, we compute the half-space charge

$$Q_{1/2} = \int_x \int_y \int_{z=0}^{z_{\max}} k^0 \, dx \, dy \, dz. \tag{8.23}$$
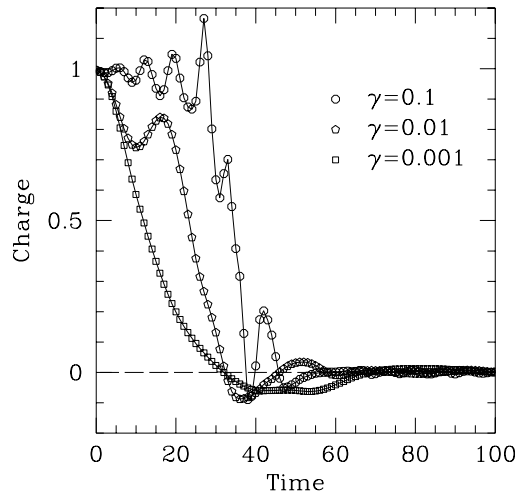
Figure 8.3: Integrated charge density of only half the space containing the monopole in a monopole-antimonopole pair. The monopoles are separated an initial distance of 30 on a 257x513 grid. For small γ, the charge simply disperses, while for larger γ a well defined annihilation occurs releasing a large amount of bosonic radiation. The charge for the other half space is simply the reflection of the graph about zero (the dashed line).

The oscillations in this quantity just prior to annihilation appear for all resolutions tried, and appear to result for similar reasons as with the single monopole.

In Figure 8.4, the results of varying the parameter L in the configuration of pair are shown. The graph of the half-space charge shows that the lifetime of the pair is clearly proportional to the initial separation. The bottom graph displays the position on the z axis of the maximum charge density as a function of time. The graph shows that the monopoles appear stationary until some time dependent on the initial separation when they "become aware" of the other monopole. The monopoles then move together and annihilate.

8.5   "Spherically Symmetric" Texture

With a good idea of what the signature of a monopole-antimonopole pair might be, we now evolve the initial data given in Eq.(8.10) with

$$\chi(r) = \frac{\pi}{2} \left(1 + \tanh\left(\frac{r - R}{\beta}\right) \right). \tag{8.24}$$

Though the precise shape of this function does not significantly affect the results, the function $\chi(r)$ used here differs from that of [85] because the function shown there is not smooth.

We find that as the texture collapses, the energies evolve as described in [85]. The
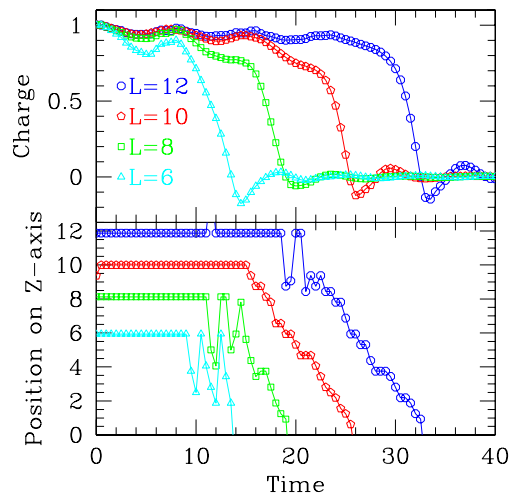
Figure 8.4: Integrated charge density of only half the space containing the monopole in a monopole-antimonopole pair for various separations L. These were run on a grid 65x129. Changes to R and β change these graphs very little (here $R = 1.5$ and $\beta = 1.0$).

kinetic and gradient energies evolve towards equipartition while the potential energy remains small.

However, our results in both the 2D axisymmetric and the 3D codes do not bear out the claim that a monopole-antimonopole pair is formed [85]. Comparing Fig. 8.6 with Fig. 8.3 reveals that the half space charge is very different and suggests that no pair is nucleated in the collapse. Fig. 8.6 suggests simply that the monopole charge density is separating, but the duration of the peak in the charge density is independent of γ and the constant R. Further, the charge does not asymptote to ± 1 giving further evidence that no monopoles are forming.

The charge density is also plotted for variations of R and β in Fig. 8.7. The figure suggests that this data does not produce pairs.

One measure, given in [85] and [72], for determining if a pair is present is that the potential energy density should be sharply peaked at the location of a monopole or antimonopole. We do see some peaking in the potential (and total) energy density for a brief period on the axis of symmetry, but this quickly diminishes and merely propagates off the grid with the remainder of the outgoing radiation.

Thus we confirm earlier results of Rhie and Bennett [72] that pair production does not occur with this initial data.
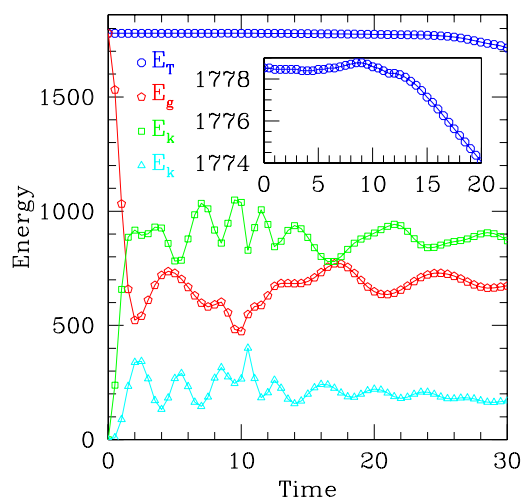
Figure 8.5: The energy components for the "spherically symmetric" texture as a function of time. Here, $\gamma = 0.1$, $R = 10$, and $\beta = 3.5$ with outer boundary ± 40. This run was on a two-dimensional grid of size 513x1025. The inset shows the total energy as a function of time. The total energy is conserved to less than one percent until gradient energy reaches the outer boundary.
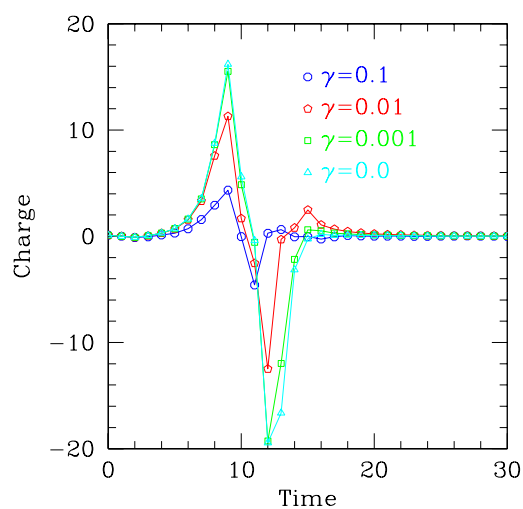
Figure 8.6: The charge integrated over half the space as a function of time. Initial data is the spherically symmetric texture with $R = 10$ and $\beta = 3.0$ with outer boundary ± 40. Run on a three-dimensional grid of size 129x129x129.

Figure 8.7: Half-space charge for the "spherically symmetric" texture for different values of R and β. The top graph shows the results from variations of β with $R = 13$. The bottom shows the results of variations of R with $\beta = 3.5$. Here, $\gamma = 0.1$ on a 513x1025 grid.

8.6   Toroidally Symmetric Texture

The initial data suggested by [58] is toroidally symmetric. It is given by

$$\Phi^1 \quad = \quad \cos\theta(\eta) \tag{8.25}$$

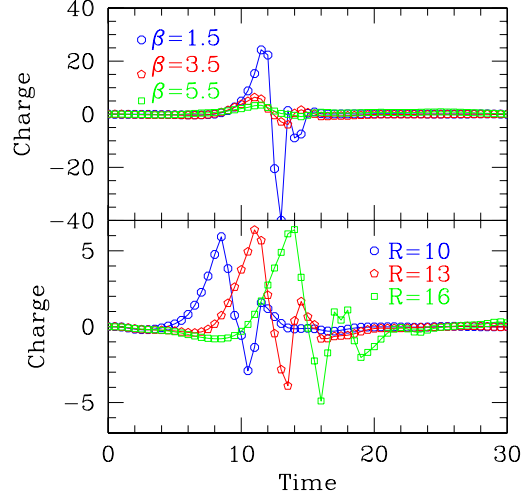$$\Phi^2 + i\Phi^3 \quad = \quad \sin\theta(\eta)e^{i(\beta-\varphi)} \tag{8.26}$$

where, in terms of Cartesian coordinates, the toroidal coordinates (η, β, φ) are defined as

$$\tanh\eta \quad = \quad \frac{2a\sqrt{x^2 + y^2}}{x^2 + y^2 + z^2 + a^2} \tag{8.27}$$

$$\tan\beta \quad = \quad \frac{2az}{x^2 + y^2 + z^2 - a^2} \tag{8.28}$$

$$\tan\varphi \quad = \quad \frac{y}{x}. \tag{8.29}$$

The parameter a is the value of the so-called degenerate tori in this coordinate system. The function $\theta(\eta)$ has boundary conditions $\theta(0) = 0$ (on the axis of symmetry *and* $r \to \infty$) and $\theta(\infty) = \pi$ (the degenerate torus). Thus a simple choice for θ is $\theta(\eta) = \pi\tanh(\eta)$. Hence, we can write the initial data as

$$\Phi(\vec{x}) = \frac{1}{\sqrt{\kappa}} \begin{pmatrix} \cos\left(2\pi a \frac{\sqrt{x^2+y^2}}{r^2+a^2}\right) \\ \sin\left(2\pi a \frac{\sqrt{x^2+y^2}}{r^2+a^2}\right) \frac{(r^2-a^2)x+2azy}{\sqrt{\left((r^2-a^2)^2+4a^2z^2\right)(x^2+y^2)}} \\ \sin\left(2\pi a \frac{\sqrt{x^2+y^2}}{r^2+a^2}\right) \frac{-(r^2-a^2)y+2azx}{\sqrt{\left((r^2-a^2)^2+4a^2z^2\right)(x^2+y^2)}} \end{pmatrix} . \tag{8.30}$$
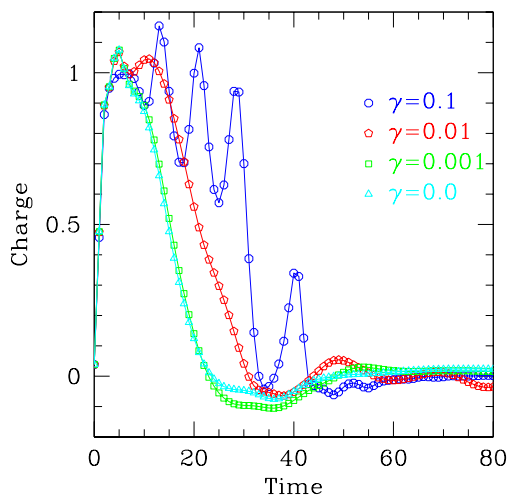
Figure 8.8: The charge integrated over half the space as a function of time. The initial data is the toroidally symmetric texture with $a = 10.01$ and with outer boundary ± 40. Run on a three-dimensional grid of size 129x129x129.

The evolutions of the toroidally symmetric texture generically display the creation of a monopole-antimonopole pair for any values of a tried. Figure 8.8 shows the half-space charge for a typical run. These results are strikingly similar to those shown for the explicit pair evolved in Figure 8.3. The charge begins at zero, quickly reaches a value of ± 1, and remains there until collapse. As γ is decreased, the behavior fundamentally changes in the same manner as that for the explicit pair. Hence, this charge separation appears intimately connected with the potential as would be expected for pair production. This connection is quite a contrast from the nearly γ-independent results of the "spherically symmetric" charge (Figure 8.6).

Even more convincing evidence for the production of a monopole pair resides in actual movies made from the evolutions. Looking at either the potential energy density or total energy density, two peaks representing the monopoles occur along the axis of symmetry. The peaks leave the center of the grid, travel outward on the axis, and eventually switch direction and annihilate.

8.7   Tests of the Spherically Symmetric Texture in 3D

Using the "spherically symmetric" texture initial data (8.10), evolutions with 33^3, 65^3, and 129^3 were compared. Figure 8.9 demonstrates that the total topological charge remained essentially zero during the evolution as it should. Boundary effects presumably account for

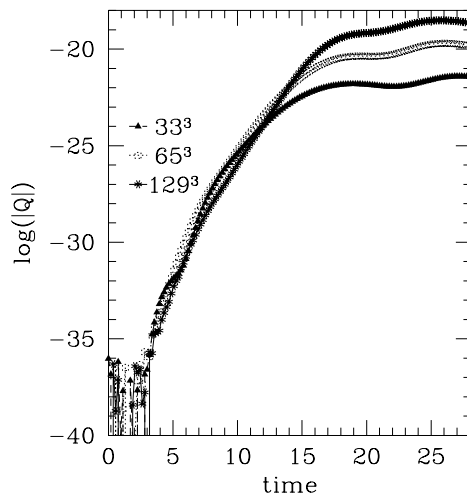the growth, though the total integral remains quite small.

Figure 8.9: Demonstration of conservation of charge. The log of the monopole charge is shown, demonstrating that it remains essentially zero for all resolutions. At about time 15, energy is leaving the grid and presumably this radiation carries with it some of the charge. Since the only the integral of the topological charge over all of space remains zero, this presumably accounts for the growth of the charge.

Figure 8.10 demonstrates that the total energy converges to conservation. That is as the energy is increased, the energy lost decreases to zero.

The half-space charge also converges as shown Figure 8.10. Here, the topological charge is integrated over only half the space along the axis of symmetry of the initial data in an effort to look for monopole formation.

The convergence factor was only computed at one early time at which time it was about 3. At such coarse resolutions, the convergence factor has been empirically observed to deviate from 4 for second order codes because of the failure of the assumptions of the Richardson expansion which forms the basis of the analysis (see Section 2.8).

8.8 Comparison of Axisymmetric and 3d Codes

Another test of the 3d code is afforded by comparison with an equivalent (for axisymmetric initial data), axisymmetric collapse code. Here, equivalent initial data is run, and the half-space charges are compared for various values of γ. Figure 8.12 shows that the agreement is quite good. That the results agree for both codes indicate the problem is being solved
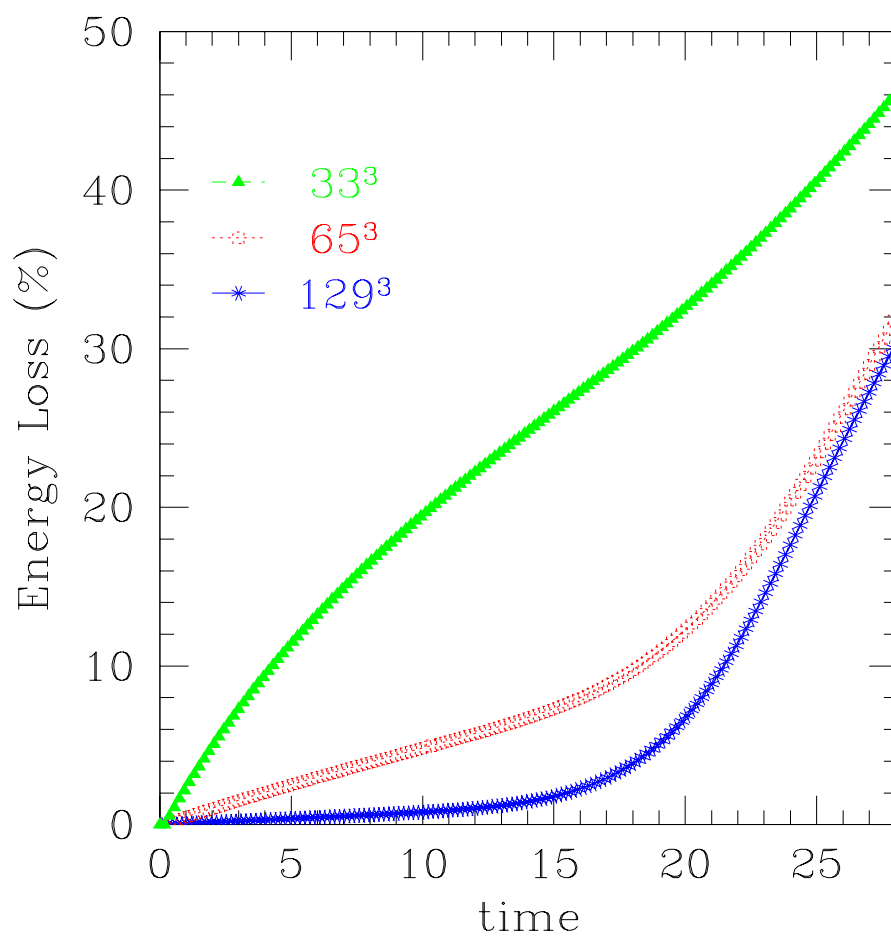
Figure 8.10: Demonstration that with increasing resolution, the energy approaches total conservation of energy. Changes in energy with respect to the initial energies are shown where the initial energies are 14.8, 16.8, and 17.3 with increasing resolution. The outer boundary receives non-vanishing derivatives from the collapse around a time of 15, and at that time energy conservation is not expected. At the finest grid, energy is conserved until that time to roughly 2%.
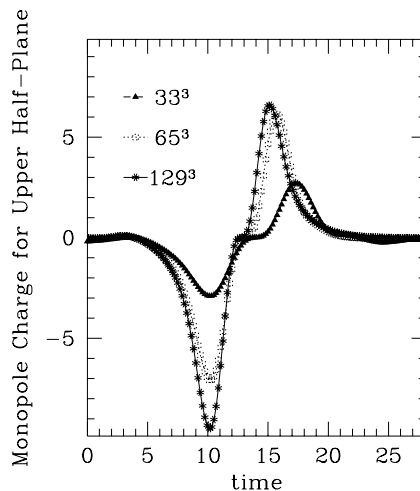
Figure 8.11: The monopole charge integrated only over the space $x > 0$ showing the possible charge separation. The charge appears to converge with increasing resolution. This does not appear to indicate the formation of a monopole-antimonopole pair as the spikes appear right after each other and also appear for $\gamma = 0$.

correctly. The results from the 3d code are from a 129^3 run while those from the axisymmetric code are on a 512×1024 grid.

Figure 8.13 shows the total energy in the numerical domain. Agreement here is not as good as that seen for the charge in Figure 8.12. It seems possible that the integral is quite dependent on a the dissipation properties of the differencing as well as behavior near the axis.

8.9 Discussion

The study of topological defects is important for studies of structure formation in cosmology, studies of superconductivity, liquid crystals, and superfluidity in condensed matter, and studies of regularity in topology.

Our code clarifys some of the conditions under which a Hopf texture nucleates a monopole-antimonopole pair. Specifically, our results confirm those of Rhie and Bennett [72] and Luo [58] that the "spherically symmetric" texture does *not* produce monopole pairs. This finding is in contradiction of that found in [85].

We conjecture that the reason monopole production was claimed in [85] is that the collapse of a "spherically symmetric" texture does produce massive radiation in shells which are peaked along the axis. By examining an isosurface of the potential energy, apparent balls

Figure 8.12: Comparison of the half-space charge for toroidal initial data in both the axisymmetric (open circles) and 3d codes (cro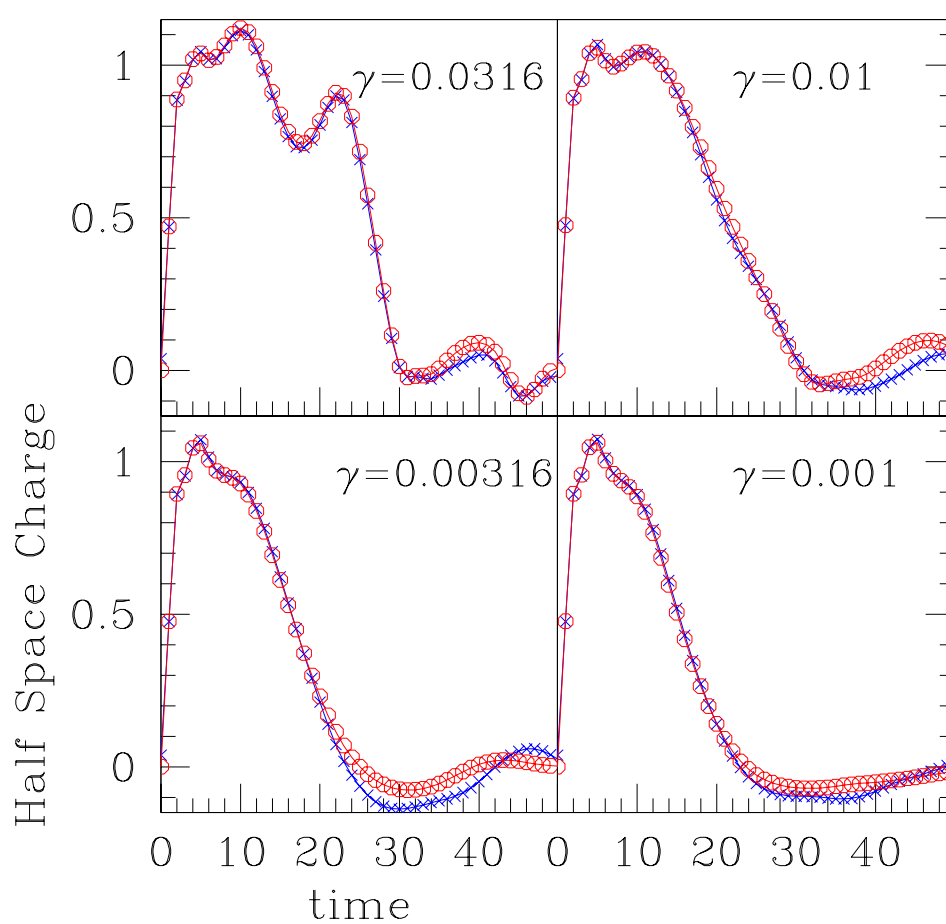sses) for various values of γ. The graph shows remarkable agreement between the axisymmetric code results and the 3d results indicating the problem is being solved correctly.
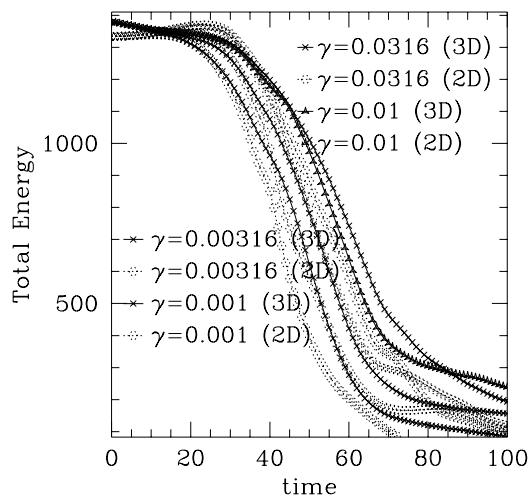
Figure 8.13: Comparison of the total energy for toroidal initial data in both the axisymmetric and 3d codes for the same runs as shown in Figure 8.12.

are seen radiating along the axis of symmetry. However, our evolutions suggest that observing isosurfaces can be deceiving. Indeed, by examining the charge density, no localization is observed.

A comparison of the two types of textures is shown in Fig. 8.14. Here, the potential energy density and charge density are at a time during the collapse of the texture which could most easily be taken for monopole formation. The energy density for the spherically symmetric texture has two peaks on the axis, however these can be seen as just part of a spherical shell of massive energy radiating away. A full time evolution makes this point more clearly by showing these pulses move out and new ones replacing them.

Contrast this with what is observed for the toroidally symmetric texture. Here, we observe two peaks along the axis which move out along the axis for some time, and then change direction. These peaks are well localized near the axis and do not appear as part of a shell of outgoing energy.

The charge densities can likewise be contrasted. For the "spherically symmetric" texture, it might appear that a monopole (the positive peak) and an antimonopole (the negative peak) exist in the graph. However, the time evolution of this field shows continual oscillation of the peaks going positive and then negative. The peaks *do not* move outwards from each other as would be expected for two monopoles.

For the toroidally symmetric texture, two opposite sign peaks are observed which *do* move apart from each other and then change direction. Their movement is in step with

the potential energy peaks, indicating that the energy is specifically associated with the trap energy of a monopole.

Figure 8.14: Comparison of the "spherically symmetric" texture with the toroidally symmetric texture showing the potential energy density and charge density as functions of ρ and z. Above, the half space charge for $z > 0$ is shown as a function of time for each type of initial data where the vertical dashed line denotes the time at which the densities are shown below. In the middle, the potential energy densities for an axisymmetric run are shown where the $\rho = 0$ axis is facing the reader. The times for the slices were chosen when monopole formation seemed most plausible for the initial data. For the "spherically symmetric" data, the time was $t = 25$ while for the toroidally symmetric the time was $t = 24$. On the bottom are shown the charge densities. Note that all scales for comparable graphs are identical.
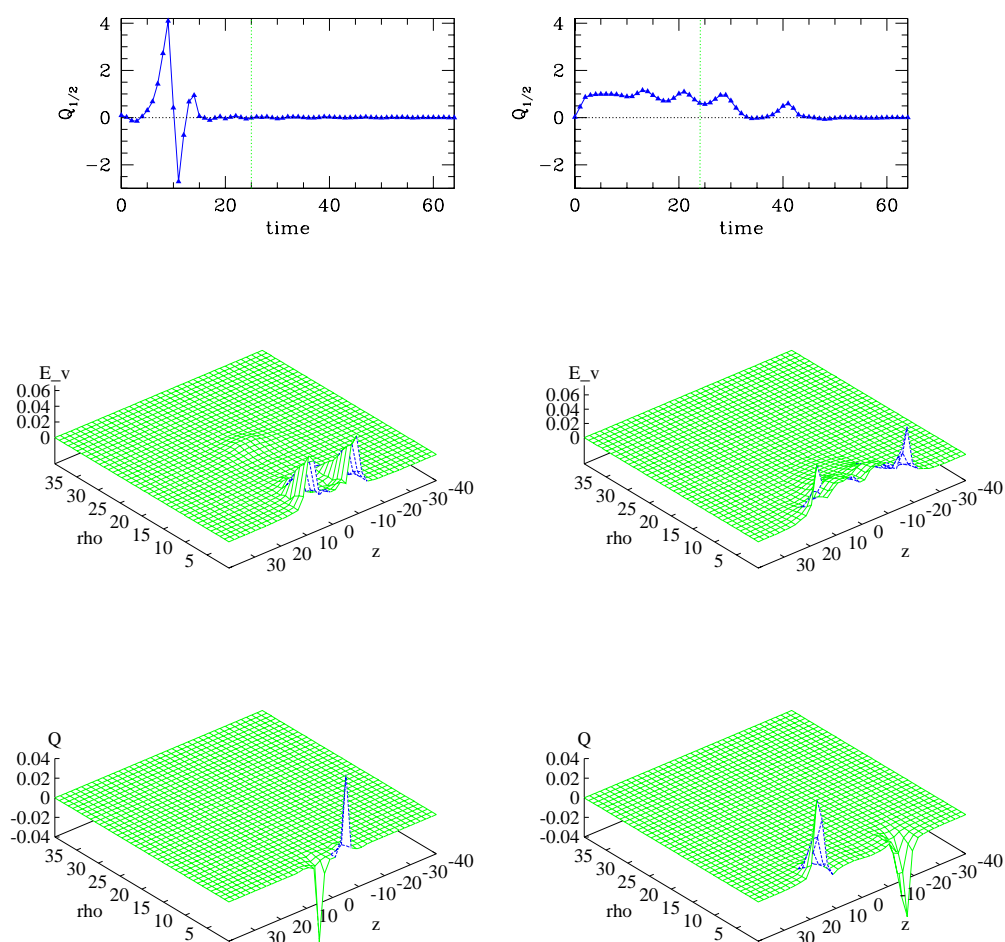
Chapter 9

Axisymmetric Gravitational Collapse

I have begun development of a two-dimensional axisymmetric gravitational model of collapse with Choptuik and Hirschmann. The method is based on the work of Nakamura and his collaborators [67, 59, 60] who use a (2+1)+1 decomposition outlined by Geroch [32]. Other notable success in axisymmetry includes [1, 2, 3, 5, 79, 86].

In Section 9.1, I briefly explain this method, following the notes of Hirschmann [46]. I then present the equations derived in this work which ultimately must be solved in Section 9.2. I then discuss a multigrid solver which solves the elliptic constraint equations. Presentation of physical results of this model must wait.

9.1 Overview of the (2+1)+1 Decomposition

We start with a 4 dimensional spacetime with metric $\gamma_{\mu\nu}$ wich is used for lowering and raising indices. Because we want to work in axisymmetry, we assume the existence of a Killing vector in the azimuthal direction

$$\xi = \frac{\partial}{\partial\varphi}, \tag{9.1}$$

which is spacelike with closed orbits. Because ξ is a Killing vector, it satisfies the Killing equation

$$\nabla_\mu \xi_\nu + \nabla_\nu \xi_\mu = 0. \tag{9.2}$$

We then project onto a 3 dimensional manifold with the projection operator (Greek letters span the full spacetime $0, 1, 2, 3$ while Latin span only the reduced spacetime $0, 1, 2$)

$$g_{\mu\nu} = \gamma_{\mu\nu} - \frac{1}{s^2} X_\mu X_\nu, \tag{9.3}$$

where $X^\mu = \delta^\mu_\varphi$. We let the norm be defined by

$$X^\mu X_\mu = s^2, \tag{9.4}$$

where s is a scalar field.

We can now proceed with a dimensional reduction where we project out the one-parameter family of isometries of $\gamma_{\mu\nu}$ generated by the Killing vector ξ. We are then left with the 3-metric g_{ab}, a scalar field, and a vector defined on the 3-spacetime. Our goal is then to find equations of motion involving only these quantities on the 3-spacetime.

This process is comparable to a Kaluza-Klein reduction from five to four dimensions, where the extra dimensions provide for the degrees of freedom of electromagnetism. In the 5 to 4 reduction, a 4 dimensional metric is recovered along with a vector which corresponds to the normal electromagnetic vector potential. The reduction also introduces a scalar field which can be set to a positive constant [4].

Here, I sketch only the basic method by which the equations of motion are obtained. The details have been worked out by Hirschmann [46]. Letting

$$A_\mu = \frac{1}{s^2} X_\mu,$$ (9.5)

the metric on the full, 4 dimensional spacetime becomes

$$\gamma_{\mu\nu} = \begin{pmatrix} g_{ab} + s^2 A_a A_b & s^2 A_a \\ s^2 A_b & s^2 \end{pmatrix}.$$ (9.6)

We also have

$$A^\mu A_\mu = \frac{1}{s^2}$$ (9.7)

and

$$A_{\nu;\mu} + A_{\mu;\nu} = 0$$ (9.8)

from the Killing Equation (9.2). Introducing a new tensor

$$F_{\mu\nu} = A_{\nu,\mu} - A_{\mu,\nu},$$ (9.9)

the connection coefficients are

$$
\begin{aligned}
{}^{(4)},{}^{\lambda}_{\mu\nu} &= {}^{(3)},{}^{\lambda}_{\mu\nu} + \Omega^{\lambda}_{\mu\nu} \\
{}^{(4)},{}^{\lambda}_{\mu\nu} &= {}^{(3)},{}^{\lambda}_{\mu\nu} + \frac{1}{2}s^2 g^{\lambda\sigma}\left[A_\nu F_{\mu\sigma} + A_\mu F_{\nu\sigma} - \partial_\sigma\left(\ln s^2\right) A_\mu A_\nu\right] \\
&\quad + \frac{1}{2}A^\lambda\left[\partial_\mu\left(s^2 A_\nu\right) + \partial_\nu\left(s^2 A_\mu\right)\right].
\end{aligned}
$$ (9.10)

Keeping in mind that $\gamma_{\mu\nu}$ and $\gamma^{\mu\nu}$ lower and raise indices, the following identities hold

$$
\begin{aligned}
g^{\mu\nu}A_\mu &= 0 && (9.11) \\
0 &= A^\nu A_{\nu,\mu} \neq A_\nu A^\nu{}_{,\mu} && (9.12) \\
A^\nu\partial_\nu\left(\log s^2\right) &= 0 && (9.13) \\
A^\nu F_{\nu\mu} &= 0. && (9.14)
\end{aligned}
$$

From the relation

$$
{}^{(4)}\Gamma^{\nu}_{\;\mu\nu} = \partial_\mu \left(\ln \sqrt{-\gamma} \right), \tag{9.15}
$$

the 4 dimensional volume element is found to be

$$
\sqrt{-\gamma} = s\sqrt{-g}. \tag{9.16}
$$

The Ricci tensor can now be written as a sum of the Ricci tensor on the three-space plus terms corresponding to the dimensional reduction

$$
{}^{(4)}R_{\mu\nu} = {}^{(3)}R_{\mu\nu} + {}^{(3)}\nabla_\lambda \Omega^{\lambda}_{\mu\nu} - {}^{(3)}\nabla_\mu \Omega^{\lambda}_{\nu\lambda} + \Omega^{\lambda}_{\mu\nu}\partial_\lambda(\ln s) - \Omega^{\sigma}_{\mu\lambda}\Omega^{\lambda}_{\nu\sigma} \tag{9.17}
$$

where ${}^{(3)}\nabla_\mu$ is the covariant derivative on the 3 dimensional manifold and we have used $\Omega^{\sigma}_{\sigma\lambda} = \partial_\lambda(\ln s)$. Expressed in terms of the 3 dimensional fields, the components of this tensor are

$$
\begin{aligned}
{}^{(4)}R_{\varphi\varphi} &= \frac{1}{4}s^4 F_{bc}F^{bc} - \kappa s\, {}^{(3)}\nabla^{a}\,{}^{(3)}\nabla_a s \\
{}^{(4)}R_{\varphi a} &= \frac{\kappa}{2s}\,{}^{(3)}\nabla^c(s^3 F_{ac}) + A_a \left[\frac{1}{4}s^4 F_{bc}F^{bc} - \kappa s\,{}^{(3)}\nabla^{a}\,{}^{(3)}\nabla_a s \right] \\
{}^{(4)}R_{ab} &= {}^{(3)}R_{ab} - \frac{1}{s}\,{}^{(3)}\nabla_a\,{}^{(3)}\nabla_b s - \frac{\kappa}{2}s^2 F_{ac}F_b{}^{c} \\
&\quad - \frac{\kappa}{s}\,{}^{(3)}\nabla^c\left[s^3 F_{c(a} \right] A_{b)} + A_a A_b \left[\frac{1}{4}s^4 F_{bc}F^{bc} - \kappa s\,{}^{(3)}\nabla^{a}\,{}^{(3)}\nabla_a s \right].
\end{aligned} \tag{9.18}
$$

The Ricci scalar is then

$$
{}^{(4)}R = {}^{(3)}R - \frac{2}{s}\,{}^{(3)}\nabla^{a}\,{}^{(3)}\nabla_a s - \frac{1}{4}s^2 F_{bc}F^{bc}, \tag{9.19}
$$

which in the absence of matter is consistent with contracting on ${}^{(3)}R_{ab}$ above and using the other equations. After specification of the matter, the equations (9.18) can now be used to get the Einstein field equations in the reduced dimensionality.

9.2 Equations to be Solved

Here I present the equations of motion assuming for the matter a complex scalar field representing a harmonic map (as discussed in spherical symmetry in Chapter 5).

To cast the equations in a first-order form, introduce auxiliary fields

$$
s_\rho = s_{,\rho} \qquad\qquad s_z = s_{,z} \tag{9.20}
$$

$$
w_\rho = w_{,\rho} \qquad\qquad w_z = w_{,z} \tag{9.21}
$$

$$
\phi_\rho = \phi_{,\rho} \qquad\qquad \phi_z = \phi_{,z}. \tag{9.22}
$$

For the complex scalar field (the matter), we make the decomposition into real and imaginary components by

$$\phi = \phi^1 + i\phi^2. \tag{9.23}$$

We use geometric units in which we have

$$G = 1. \tag{9.24}$$

For the elliptic constraints (the last four equations), the equations have been put into the form

$$Lu_i = f_i \tag{9.25}$$

where u_i runs over the fields $a, \beta_\rho, \beta_z, \alpha$. Hence, the four terms f_i represent the right sides of the four elliptic equations independent of the fields u_i.

The equations are then

$$\dot{s} = -\alpha s \chi + \beta^\rho s + \rho \beta^\rho s_\rho + \beta^z s_z \tag{9.26}$$

$$\dot{s}_\rho = \left(-\alpha s \chi + \beta^\rho s + \rho \beta^\rho s_\rho + \beta^z s_z\right)_{,\rho} \tag{9.27}$$

$$\dot{s}_z = \left(-\alpha s \chi + \beta^\rho s + \rho \beta^\rho s_\rho + \beta^z s_z\right)_{,z} \tag{9.28}$$

$$\dot{\chi} = -\frac{1}{sa^2}\left[(\alpha s_\rho)_{,\rho} + (\alpha s_z)_{,z}\right] - \frac{2}{s^2 a^2}(\alpha s^2)_{,\rho^2}$$
$$\quad -\frac{\rho^2 \alpha}{2a^2 s^4}\left[(4w + \rho w_\rho)^2 + (\rho w_z)^2 - \rho^2 a^2 u^2\right]$$
$$\quad +\rho \beta^\rho \chi_{,\rho} + \beta^z \chi_{,z} \tag{9.29}$$

$$\dot{w} = -\alpha u + 4\beta^\rho w + \rho \beta^\rho w_\rho + \beta^z w_z \tag{9.30}$$

$$\dot{w}_\rho = \left(-\alpha u + 4\beta^\rho w + \rho \beta^\rho w_\rho + \beta^z w_z\right)_{,\rho} \tag{9.31}$$

$$\dot{w}_z = \left(-\alpha u + 4\beta^\rho w + \rho \beta^\rho w_\rho + \beta^z w_z\right)_{,z} \tag{9.32}$$

$$\dot{u} = -\frac{s^3}{a^2}\left(\frac{\alpha}{s^3}\right)_{,\rho}\left(8\left(\rho w\right)_{,\rho^2} - 3w_\rho\right)$$
$$\quad -\frac{s^3}{a^2}\left[\left(\frac{\alpha}{s^3}\right)\left(10\left(\rho w_\rho\right)_{,\rho^2} - 4\left(w_\rho\right)_{,\rho}\right) + \left(\frac{\alpha}{s^3}w_z\right)_{,z}\right]$$
$$\quad -4\alpha u \chi + 4\beta^\rho u + \rho \beta^\rho u_{,\rho} + \beta^z u_{,z} \tag{9.33}$$

$$\dot{\phi} = -\alpha F + \rho \beta^\rho \phi_{,\rho} + \beta^z \phi_{,z} \tag{9.34}$$

$$\dot{\phi}_\rho = \left(-\alpha F + \rho \beta^\rho \phi_{,\rho} + \beta^z \phi_{,z}\right)_{,\rho} \tag{9.35}$$

$$\dot{\phi}_z = \left(-\alpha F + \rho \beta^\rho \phi_{,\rho} + \beta^z \phi_{,z}\right)_{,z} \tag{9.36}$$

$$\dot{F}^1 = -\frac{1}{sa^2}\left[\phi_\rho^1 (\alpha s)_{,\rho} + \left(\alpha s \phi_z^1\right)_{,z}\right] - \frac{2\alpha}{a^2}\left(\rho \phi_\rho^1\right)_{,\rho^2}$$
$$\quad +\rho \beta^\rho F^1_{,\rho} + \beta^z F^1_{,z}$$
$$\quad +\frac{2\kappa}{a^2 \left(1 - \kappa \left((\phi^1)^2 + (\phi^2)^2\right)\right)^2}\Bigg[$$

$$a^2\phi^1\left((F^1)^2-(F^2)^2\right)-\phi^1\left((\phi_\rho^1)^2-(\phi_\rho^2)^2\right)-\phi^1\left((\phi_z^1)^2-(\phi_z^2)^2\right)$$

$$+2\phi^2\left(a^2F^1F^2-\phi_\rho^1\phi_\rho^2-\phi_z^1\phi_z^2\right)\bigg] \tag{9.37}$$

$$\dot{F}^2 = -\frac{1}{sa^2}\left[\phi_\rho^2\left(\alpha s\right)_{,\rho}+(\alpha s\phi_z^2)_{,z}\right]-\frac{2\alpha}{a^2}\left(\rho\phi_\rho^2\right)_{,\rho^2}$$

$$+\rho\beta^\rho F_{,\rho}^2+\beta^z F_{,z}^2$$

$$+\frac{2\kappa}{a^2\left(1-\kappa\left((\phi^1)^2+(\phi^2)^2\right)\right)^2}\bigg[$$

$$-a^2\phi^2\left((F^1)^2-(F^2)^2\right)+\phi^2\left((\phi_\rho^1)^2-(\phi_\rho^2)^2\right)+\phi^2\left((\phi_z^1)^2-(\phi_z^2)^2\right)$$

$$+2\phi^1\left(a^2F^1F^2-\phi_\rho^1\phi_\rho^2-\phi_z^1\phi_z^2\right)\bigg]. \tag{9.38}$$

The elliptic equation for a is

$$(\log a^2)_{,\rho\rho}+(\log a^2)_{,zz} = -\frac{2}{s}\left[s_{\rho,\rho}+\frac{2}{\rho}s_\rho+s_{z,z}\right] \tag{9.39}$$

$$+a^2\bigg\{\frac{3}{2}\chi^2+\frac{\rho^4}{2s^4}u^2 \qquad -\frac{\rho^2}{2s^4}\left[(4w+\rho w_\rho)^2+(\rho w_z)^2\right]$$

$$+\frac{1}{2\alpha^2}\left[((\rho\beta^\rho)_{,\rho}-\beta^z_{,z})^2+(\beta^z_{,\rho}+\rho\beta^\rho_{,z})^2\right] \qquad -2\frac{(\phi_\rho^1)^2+(\phi_\rho^2)^2+(\phi_z^1)^2+(\phi_z^2)^2}{(1-\kappa((\phi^1)^2+(\phi^2)^2))^2}.$$

$$+16\pi\frac{(F^1)^2+(F^2)^2}{(1-\kappa((\phi^1)^2+(\phi^2)^2))^2}\bigg\}$$

The elliptic equation for β^ρ

$$3\left(\rho^2\beta^\rho_{,\rho}\right)_{,\rho^3}+\beta^\rho_{,zz} = 0. \tag{9.40}$$

$$-\frac{1}{\rho}\left(\log\frac{\alpha}{a^2s}\right)_{,\rho}(\rho\beta^\rho_{,\rho}+\beta^\rho)$$

$$-\left(\log\frac{\alpha}{a^2s}\right)_{,z}\beta^\rho_{,z}+\frac{1}{\rho^2}\left(\rho\beta^\rho_{,\rho}+\beta^\rho\right)$$

$$+\frac{1}{\rho}\left(\log\frac{\alpha}{a^2s}\right)_{,\rho}\beta^z_{,z}-\frac{1}{\rho}\left(\log\frac{\alpha}{a^2s}\right)_{,z}\beta^z_{,\rho}$$

$$-\frac{1}{\rho^2}\beta^z_{,z}-\frac{1}{\rho}\alpha\chi_{,\rho}-3\alpha\chi\left(\frac{1}{\rho^2}+\frac{s_\rho}{\rho s}\right)$$

$$-\frac{\alpha u}{s^4}\rho^2(4w+\rho w_\rho)-32\pi\frac{\alpha}{\rho}\frac{F^1\phi_\rho^1+F^2\phi_\rho^2}{(1-\kappa((\phi^1)^2+(\phi^2)^2))^2}$$

The elliptic equation for β^z

$$\beta^z_{,\rho\rho}+\beta^z_{,zz} = 0. \tag{9.41}$$

$$-\left[\left(\log\frac{\alpha}{a^2s}\right)_{,\rho}-\frac{1}{\rho}\right]\beta^z_{,\rho}-\left(\log\frac{\alpha}{a^2s}\right)_{,z}\beta^z_{,z}$$

$$- \left[\left(\log \frac{\alpha}{a^2 s} \right)_{,\rho} - \frac{1}{\rho} \right] \rho \beta^\rho_{,z} + \left(\log \frac{\alpha}{a^2 s} \right)_{,z} (\rho \beta^\rho)_{,\rho} - \alpha \chi_{,z}$$

$$- 3\alpha \chi \frac{s_z}{s} - \frac{\alpha u}{s^4} \rho^4 w_z - 32\pi\alpha a^2 \frac{F^1 \phi_z^1 + F^2 \phi_z^2}{(1 - \kappa ((\phi^1)^2 + (\phi^2)^2))^2}$$

The elliptic equation for α

$$2 (\rho \alpha_{,\rho})_{,\rho^2} + \alpha_{,zz} = 0. \qquad (9.42)$$

$$+ \frac{1}{s} (s_\rho \alpha_{,\rho} + s_z \alpha_{,z})$$

$$+ \alpha \left\{ \frac{2}{s} \left[3 \left(\rho^2 s_\rho \right)_{,\rho^3} + s_{z,z} \right] + \left[(\log a^2)_{,\rho\rho} + (\log a^2)_{,zz} \right] \right.$$

$$+ \frac{a^2}{2s^4} u^2 \rho^4$$

$$+ 32\pi \frac{(\phi_\rho^1)^2 + (\phi_\rho^2)^2 + (\phi_z^1)^2 + (\phi_z^2)^2}{(1 - \kappa ((\phi^1)^2 + (\phi^2)^2))^2} \right\}$$

The appropriate boundary conditions for the fields are determined by their behavior on the axis ($\rho = 0$) and at large radius $r = \sqrt{\rho^2 + z^2}$

$$\beta^\rho|_{r=r_{\max}} \propto \frac{1}{r\rho} \qquad (9.43)$$

$$\beta^z|_{r=r_{\max}} \propto \frac{1}{r} \qquad (9.44)$$

$$a|_{r=r_{\max}} \propto 1 + \frac{C}{r} \qquad (9.45)$$

$$\alpha|_{r=r_{\max}} \propto 1 + \frac{D}{r} \qquad (9.46)$$

$$\beta^\rho|_{\rho=0} = f(\rho = 0) + \rho^2 f''(0) \qquad (9.47)$$

$$\beta^z|_{\rho=0} = g(\rho = 0) + \rho^2 g''(0) \qquad (9.48)$$

$$a|_{\rho=0} = h(\rho = 0) + \rho^2 h''(0) \qquad (9.49)$$

$$\alpha|_{\rho=0} = k(\rho = 0) + \rho^2 k''(0), \qquad (9.50)$$

for real constants C and D, and free functions $f(\rho)$, $g(\rho)$, $h(\rho)$, and $k(\rho)$. The conditions enforced numerically are found by differentiating these conditions. For β^z, the condition is

$$\beta^z = -r\beta^z_{,r}$$
$$= -\rho\beta^z_{,\rho} - z\beta^z_{,z}. \qquad (9.51)$$

For a, the derivative of the Equation (9.45) is

$$a_{,r} = \frac{-C}{r^2} = -\frac{a-1}{r}, \qquad (9.52)$$

from which we get the condition

$$a = 1 - ra_{,r}$$

$$= 1 - \rho a_{,\rho} - z a_{,z}. \tag{9.53}$$

Similarly for α, the condition is

$$\alpha = 1 - \rho \alpha_{,\rho} - z \alpha_{,z}. \tag{9.54}$$

For β^ρ, substituting $\rho = r \cos \theta$ yields the condition

$$r \left(r \cos \theta \right) \beta^\rho = C, \tag{9.55}$$

whose derivative yields the condition which will be enforced along the outer boundary

$$
\begin{aligned}
2r \cos \theta \beta^\rho + r^2 \cos \theta \beta^\rho_{,r} &= 0 \\
2\rho \beta^\rho + r \rho \beta^\rho_{,r} &= 0 \\
2\rho \beta^\rho + \rho^2 \beta^\rho_{,\rho} + \rho z \beta^\rho_{,z} &= 0 \\
2\beta^\rho + \rho \beta^\rho_{,\rho} + z \beta^\rho_{,z} &= 0.
\end{aligned}
\tag{9.56}
$$

9.3   Tests of the Multigrid Solver

I have implemented a FAS multigrid solver for the four elliptic equations presented in the previous section (see [12] for a discussion of the FAS multigrid method). As a first indication of the efficiency of the solver, the residuals r_i are plotted in Figure 9.1 as defined using the notation of Equation (9.25)

$$r_i = L u_i - f_i. \tag{9.57}$$

Three cases are shown comparing the results of pure relaxation and v-cycles of the multigrid solver. The unit of work on the horizontal axis is one v-cycle for the multigrid output, and for the relaxation output I have equated 15 relaxation sweeps per unit number of v-cycles for comparison purposes. The residuals from the multigrid solver are shown for two configurations, one with fixed outer boundary conditions and the other with the proper outer boundary treatment discussed in the previous section.

The graph makes clear that the multigrid solver fails miserably when enforcing a non-fixed outer boundary condition, driving the residual to infinity. However, equally clear, the multigrid method with fixed outer boundary is superior to relaxation in its ability to rapidly drive the residual down to machine precision. Implementation of non-homogeneous boundary conditions with a multigrid solver is non-trivial, and here, further work with the solver is needed.

In fact, the method of Section 7.6 used to treat the axis boundary appears to decrease the effectiveness of the solver because of axis problems with the field β_ρ. This axis problem likely accounts for the decrease in the rate of residual reduction as the resolution is increased as shown in Figure 9.2.
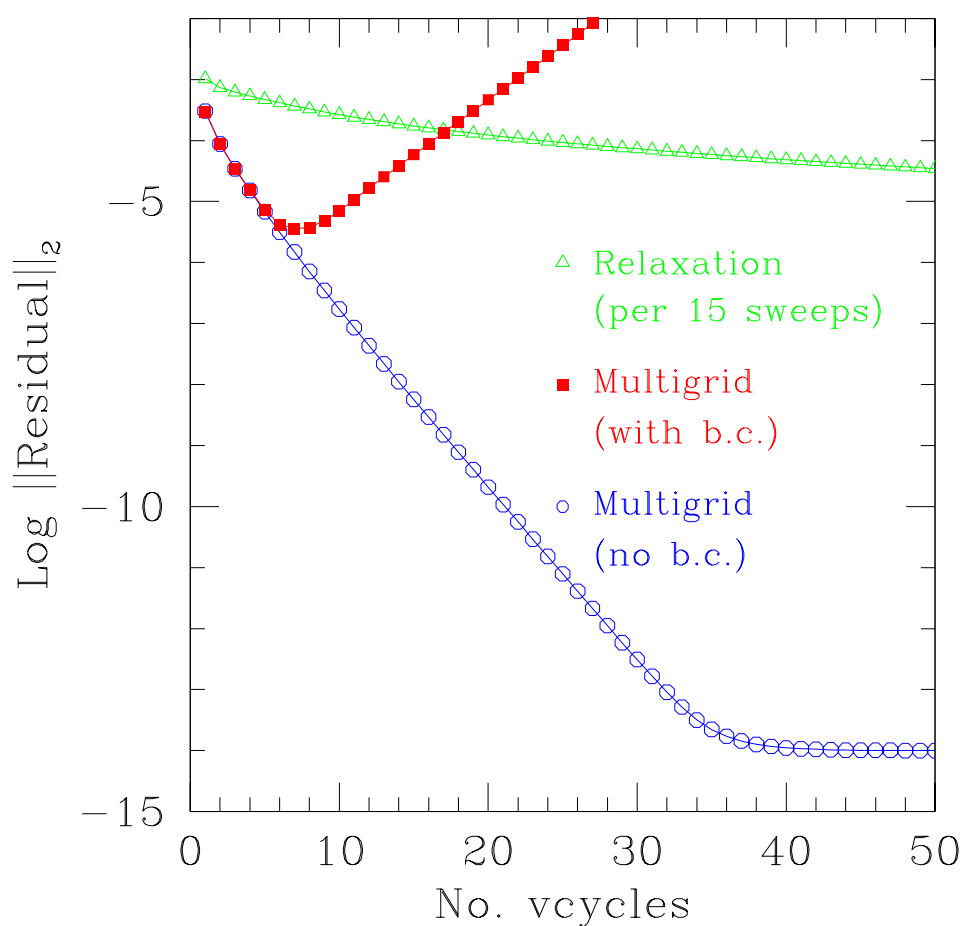
Figure 9.1: Comparison of the efficiency of relaxation and multigrid in driving the residual down. Equating 15 relaxation sweeps with the amount of work in one v-cycle, the log of the residual is plotted versus work done. In triangles, the relaxation residual is very slowly being driven down. However, in circles, the multigrid solver with fixed outer boundary conditions is seen to quickly drive the residual down to machine precision. When the outer boundary treatment is turned on (solid squares), the residual eventually increases showing the failure of the code. This boundary treatment needs further work.

Figure 9.2: Demonstration of a decreasing rate of residual reduction as the resolution is increased for the multigrid solver. The log of the residuals are shown as a function of the number of v-cycles for four resolutions. With increasing resolution, the rate at which the problem is solved decreases. This problem is likely attributable to the axis treatment of the field β_ρ.

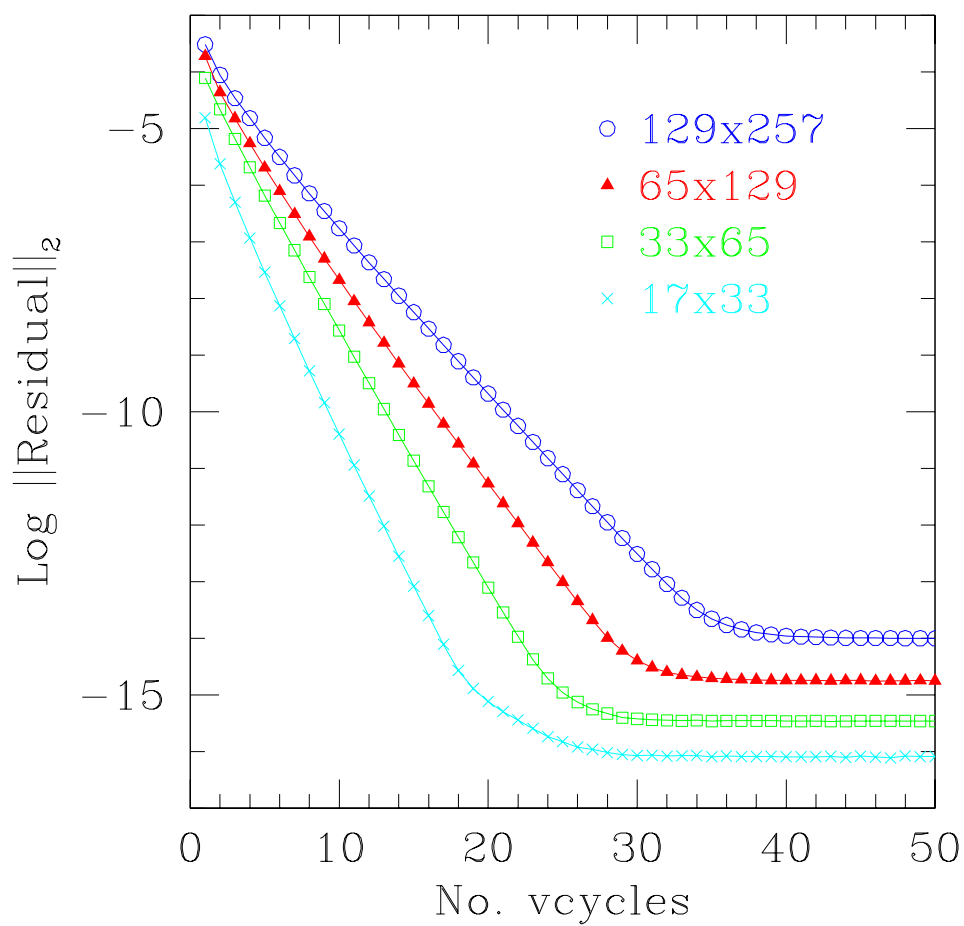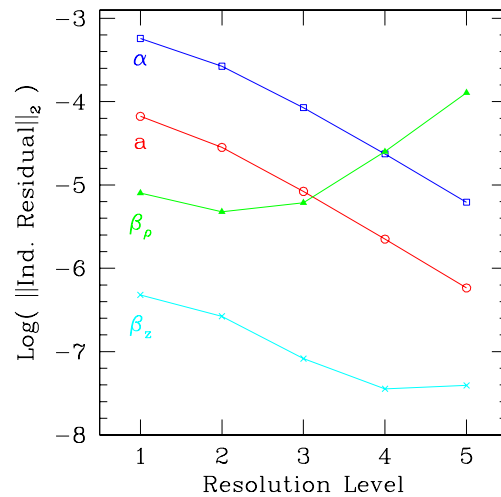Figure 9.3: Independent residuals as a function of resolution for the multigrid solver with fixed outer boundary condition. The norm of the residual is shown for each field for five different resolutions. The resolutions corresponding to the label level of resolution are (1) 17x33 (2) 33x65 (3) 65x129 (4) 129x257 (5) 257x512. The graph shows an obvious problem with the field β_ρ.

Another criterion by which the correctness of the solver can be measured is an independent residual evaluation. In other words, approximate the operator L in a different manner than implemented in the solver, and then evaluate the residual with that operator. This *independent residual* (as opposed to the dependent residual shown in Figure 9.2) will in general be non-zero, however, its norm must go to zero as the exact solution to the continuum equation is approached.

I plot the norm of an independent residual for different resolutions in Figure 9.3. Because the residual associated with the field β_ρ is growing, it is apparent that something is wrong. Two-dimensional plots of the residual in space show the problem to be at the axis.

Another test of the multigrid employs a method outlined by Choptuik [22]. Say we want to solve the continuum equation

$$Lu = R \tag{9.58}$$

for u, where L is some differential operator and R is just the right-hand side. If we then have a discrete solver which finds an approximation, $\tilde{u}$, to the finite-difference approximation of Equation (9.58), then we would like to be able to compare $\tilde{u}$ to some exact solution. However, in this case and many others, no exact solution is known.

Instead, we may choose some ansatz $\bar{u}$ which can serve as an exact solution. Of course, since it will in general not be a solution to the Equation (9.58), we cannot expect to be able to usefully compare $\bar{u}$ and $\tilde{u}$. Instead, we operate on the ansatz $\bar{u}$ with L and subtract R to get an effective source term S

$$S = L\bar{u} - R. \tag{9.59}$$

If $\bar{u}$ were a solution, then we would have $S = 0$. Instead, S will in general be nonzero. However, if we now define a new right-hand side, $\bar{R} = R + S$, then we observe that $\bar{u}$ is now an exact solution to the differential equation

$$L\bar{u} = \bar{R}. \tag{9.60}$$

To test the solver, we pick the ansatz and compute the source term S analytically. In the code, the source term S is calculated and added to R. The solver is then called with this new right-hand side, and returns a solution $\tilde{u}$. Since $\bar{u}$ is the exact solution to the equation being solved, the solver only works if $\tilde{u}$ converges to $\bar{u}$.

Consistent with the results of the previous tests, this test of convergence to an "exact" solution indicates a problem. Figure 9.4 displays the log of the norm of the differences $\bar{u} - \tilde{u}$, which should vanish for high resolutions. All the fields initial show convergence to the exact solution, but eventually increase. Again, this problem is likely due to the axis problem in β_ρ.

In summary, the multigrid solver as implemented has yet to correctly solve the boundary conditions. However, the tests as described here should lead the way to correcting the problems and ultimately having faith in the results once the solver passes these tests.

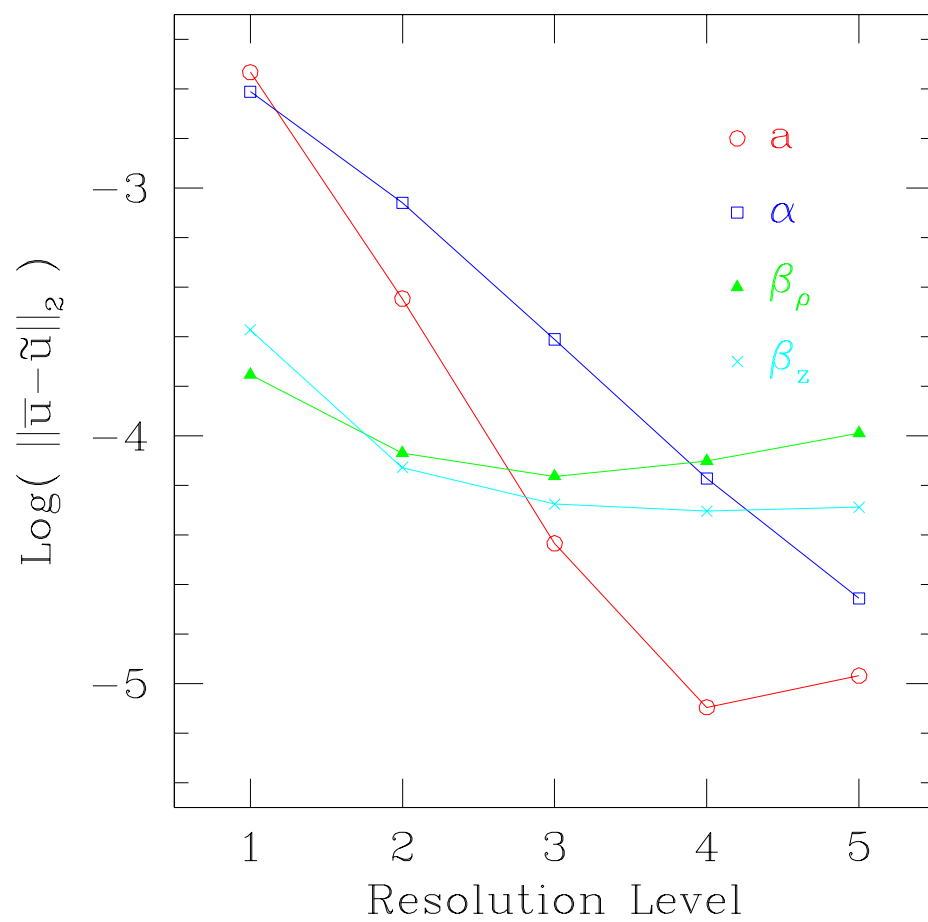Figure 9.4: Demonstration of convergence of the multigrid solver to an "exact" solution. The log of the norm of the difference between the assumed ansatz and the field is shown for each field. The resolution levels correspond to those in Figure 9.3. Problems with β_ρ near the axis are suspected of causing the growth of the difference for high resolutions. The outer boundary is held fixed for these runs.

Chapter 10

Conclusion

The results presented here describe the dynamics of scalar fields. Although a particularly simple form of matter, scalar fields allow for a rich solution space whose exploration is made possible by numerical modeling.

With the maturity of numerical methods in general and numerical relativity in particular, this solution space is being unlocked. No one could have predicted that a discretely self-similar solution to Einstein's equation would sit everywhere on the threshold of black hole formation in the real scalar field model [24]. Only through the efforts of numerical modeling has the study of these phenomena begun. One such interesting effort is Garfinkle's work that examines the structure of Einstein's equations [30].

Of course, Einstein's equations are suspected to be a low-energy effective approximation to a discrete theory of gravity whose effects become manifest at the Planck scale. If such a quantum theory of gravity were finally developed, perhaps numerical relativity might find exact solutions. Gentle and Miller present interesting numerical results with Regge calculus in [31].

Returning to the results studied here, this work begins with a study of black hole critical phenomena in Brans-Dicke gravity. In this model, two self-similar critical solutions exchange stability as the coupling parameter ω is changed. In the limit $\omega \to \infty$, the model corresponds to general relativity (GR) and the discretely self-similar solution (DSS) is the attracting critical solution as Choptuik found in GR [24]. However, as ω is decreased, the DSS is no longer seen, and instead a transition occurs such that a continuously self-similar solution (CSS) is the attracting critical solution.

This transition from one self-similar solution to another self-similar one is quite different than a transition from a self-similar solution to a static solution, as seen for example in [25]. In the latter case, the transition from the self-similar solution to a static solution with an inherent length scale occurs as terms in the action which set a length scale become important relative to the scale free terms. In fact, for the massive scalar field studied in [11] a transition from the DSS of the massless case to static stars was expected [27]. However, here

147

it is not at all well understood why a transition occurs from the CSS to the DSS. Further, that this transition occurs between an echoing critical solution, the DSS, and a solution with an internal rotation is remarkable. For the DSS, the entire spacetime undergoes echoing such that, modulo a scale transformation, it repeats itself every Δ in log time. For the CSS, this echoing takes the form of an internal rotation of the complex scalar field. Discovery of a relationship between the period of the DSS's echoing and the frequency of rotation of the CSS would likely lead to better understanding of the nature of the DSS.

Already having a code to model a scalar field coupled to Brans-Dicke gravity afforded the opportunity to study the stability of an irregular family of static solutions of the model. By solving for a particular member of the family, the static solution could be input to the evolution code as initial data. Adding at large radius a small perturbation to the static solution, this data was then evolved. A stable solution would then eventually settle down in time, however, these solutions generically grew in time. This growth demonstrates the instability of the solutions, a conclusion also reached by perturbation analysis. The perturbation analysis revealed a single unstable mode associated with the solutions which could then be compared to the growth in the fully nonlinear evolutions. This comparison provides a dramatic check of both results because the growth of the solution matches that predicted by the perturbation analysis. Further, the evolutions suggest that this family is in fact a critical solution.

Considering a generalization of the scalar field coupled to Brans-Dicke, I study the harmonic map parameterized by κ. Duplicating the same transition seen in the Brans-Dicke model, I find quite special initial data which find upon tuning only the CSS, oblivious to the change in stability of the CSS. I find that this initial data maximizes its charge for a given energy, and this symmetry excludes the growth of the extra unstable modes of the CSS.

The harmonic map also extends the Brans-Dicke model, and in this new region of parameter space, I find a new critical solution. This solution appears to have discrete structure similar to the DSS, but the details are still unclear.

The studies of electromagnetic propagation and texture collapse have shown the utility of a Crank-Nicholson evolution scheme in two and three dimensions. The model of collapse with the broken symmetry $SO(3)/SO(2)$ has revealed interesting dynamics including the nucleation of a monopole-antimonopole pair. Not only have the evolutions shown that such nucleation occurs only with the toroidally symmetric texture and not the spherically symmetric, but evolutions have also shown that the monopoles are stable to three-dimensional perturbations. Both these codes should be useful for future studies of electromagnetic solitons and other broken symmetries.

Finally, the ambitious goal of modeling axisymmetric collapse with a (2+1)+1 decomposition of spacetime has begun with encouraging results. Though further work remains

with the multigrid elliptic solver, future results will be able to answer questions about angular momentum scaling, naked singularity formation, and stability of critical solutions to asymmetric modes.

Bibliography

[1] A.M. Abrahams and C.R. Evans, "Critical Behavior and Scaling in Vacuum Axisymmetric Gravitational Collapse," *Phys Rev. Lett.,* **70**, 2980-2983 (1993).

[2] A.M. Abrahams, G.B. Cook, S.L. Shapiro, and S.A. Teukolsky, "Evolution of Relativistic Stellar Systems with Rotation," *Phys. Rev.* **D49**, 5153-5164 (1994).

[3] P. Anninos, D. Hobill, E. Seidel, L. Smarr, and W. Suen, "The Head-On Collision of Two Equal Mass Black Holes," *Phys. Rev.* **D52**, 2044-2058 (1995).

[4] T. Appelquist, A. Chodos, and P.G.O. Freund, "Modern Kaluza-Klein Theories," (Addison-Wesley, Menlo Park, 1987).

[5] J.M. Bardeen, and T. Piran, "General Relativistic Axisymmetric Rotating Systems: Coordinates and Equations," *Phys. Reports* **96**, 205-250 (1983).

[6] G.I. Barenblatt, *Similarity, Self-Similarity, and Intermediate Asymptotics*, (Consultants Bureau, New York, 1979).

[7] R. Bartnik and J. McKinnon, "Particlelike Solutions of the Einstein-Yang-Mills Equations," Phys. Rev. Lett. **61**, 141-144 (1988).

[8] A.A. Belavin and A.M. Polyakov, *JETP Lett.* **22**, 245 (1975).

[9] D.P. Bennett and S.H. Rhie, "Cosmological Evolution of Global Monopoles and the Origin of Large-Scale Structure," *Phys. Rev. Lett.* **65**, 1709-1712 (1990).

[10] P. Bizon, "How to Make a Tiny Black Hole?," LANL preprint gr-qc/9606060 (1996).

[11] P.R. Brady, C.M. Chambers, and S.M.C.V. Goncalves, "Phases of massive scalar field collapse," *Phys. Rev.* **D56**, 6057-6061 (1997).

[12] A. Brandt, "MultiLevel Adaptive Solutions to Boundary Value Problems," *Math. of Computation* **31**, 333-390 (1977).

[13] A. Brandt, "Guide to Multigrid Development," in *Lecture Notes in Mathematics* **960**, 220-312, (Springer-Verlag, New York, 1982).

[14] C. Brans and R.H. Dicke, "Mach's Principle and a Relativistic Theory of Gravitation." *Phys. Rev.* **124**, 925-935 (1961).

[15] M.W. Browne, "A Bet on a Cosmic Scale, and a Concession, Sort of," *NY Times*, Feb. 12, (1997).

[16] H.A. Buchdahl, "Reciprocal Static Metrics and Scalar Fields in the General Theory of Relativity," Phys. Rev. **115**, 1325-1328 (1959).

[17] M. Carmeli, *Classical Fields: General Relativity and Gauge Theory*, (Wiley, New York, 1982).

[18] G. Chao-Hao, "On the Cauchy Problem for Harmonic Maps Defined on Two-Dimensional Minkowski Space," *Comm. on Pure and Applied Math.* **33**, 727-737 (1980).

[19] M. Creutz, "Phase Transitions," LANL preprint hep-lat/9708021 (1997).

[20] D. Christodoulou and A.S. Tahvildar-Zadeh, "On the Regularity of Spherically Symmetric Wave Maps," *Comm. on Pure and Applied Math.* **46**, 873-886 (1993).

[21] I. Chuang, R. Durrer, N. Turok, B. Yurke, "Cosmology in the Laboratory: Defect Dynamics in Liquid Crystals," *Science* **251**, 1336 (1991).

[22] M.W. Choptuik, "A Study of Numerical Techniques for Radiative Problems in General Relativity," Ph.D. thesis, The University of British Columbia, unpublished (1982).

[23] M.W. Choptuik, "Consistency of Finite-difference Solutions of Einstein's Equations," *Phys. Rev.* **D44**, 3124-3135 (1991).

[24] M.W. Choptuik, "Universality and Scaling in Gravitational Collapse of a Massless Scalar Field", *Phys. Rev. Lett.,* **70**, 9-12 (1993).

[25] M.W. Choptuik, T. Chmaj, and P. Bizon, "Critical Behaviour in Gravitational Collapse of a Yang-Mills Field," *Phys. Rev. Lett.* **77**, 424-427 (1996).

[26] M.W. Choptuik, E.W. Hirschmann, and S.L. Liebling, "Instability of an 'Approximate Black Hole'," *Phys. Rev.* **D55**, 6014-6018 (1997).

[27] M.W. Choptuik, Personal communication, (1997).

[28] D.M. Eardley, E.W. Hirschmann, and J.H. Horne, "S Duality at the Black Hole Threshold in Gravitational Collapse," *Phys. Rev.* **D52**, 5397-5401 (1995).

[29] C.R. Evans and J.S. Coleman, "Critical Phenomena and Self-similarity in the Gravitational Collapse of Radiation Fluid," *Phys. Rev. Lett.,* **72**, 1782-1785 (1994).

[30] D. Garfinkle, "Choptuik Scaling and the Scale Invariance of Einstein's Equation," *Phys. Rev.* **D56**, 3169-3173 (1997).

[31] A.P. Gentle and W.A. Miller, "A Fully (3+1)-D Regge Calculus Model of the Kasner Cosmology," *Class. Quant. Grav.* **15**, 389-405 (1998).

[32] R. Geroch, "A Method for Generating Solutions of Einstein's Equations," *Journal of Math. Physics* **12**, 918-824 (1971).

[33] N. Goldenfeld, *Lectures on Phase Transitions and the Renormalization Group*, (Addison-Wesley, Reading, 1992).

[34] A.S. Goldhaber, "Collapse of a 'Global Monopole', " *Phys Rev. Lett.* **63**, 2158 (1989).

[35] H.B. Griffiths and A. Oldknow, *Mathematics of Models: Continuous and Discrete Dynamical Systems*, (Ellis Horwood, New York, 1993).

[36] J. Guckenheimer, P. Holmes, *Nonlinear Oscillations, Dynamical Systems, and Bifurcations of Vector Fields*, (Springer-Verlag, New York, 1983).

[37] C. Gundlach, "The Choptuik Space-time as an Eigenvalue Problem," *Phys. Rev. Lett.* **75**, 3214-3217 (1995).

[38] C. Gundlach, "Charge Scaling and Universality in Critical Collapse," *Phys. Rev.* **D54**, 7353-7360 (1996).

[39] C. Gundlach, "Understanding Critical Collapse of a Scalar Field," *Phys. Rev.* **D55**, 695-713 (1997).

[40] C. Gundlach, "Critical Phenomena in Gravitational Collapse," LANL preprint gr-qc/9712084 (1997).

[41] B. Gustafsson, H. Kreiss, and J. Oliger, "Time Dependent Problems and Difference Methods," (Wiley, New York, 1995).

[42] T. Hara, T. Koike, and S. Adachi, "Renormalization Group and Critical Behavior in Gravitational Collapse," LANL preprint gr-qc/9607010 (1996).

[43] E.W. Hirschmann and D.M. Eardley, "Criticality and Bifurcation in the Gravitational Collapse of a Self-Coupled Scalar Field," *Phys. Rev.* **D56**, 4696-4705 (1997).

[44] E.W. Hirschmann and D.M. Eardley, "Universal Scaling and Echoing in Gravitational Collapse of a Complex Scalar Field," *Phys. Rev.* **D51**, 4198-4207 (1995).

[45] E.W. Hirschmann and D.M. Eardley, "Critical Exponents and Stability at the Black Hole Threshold for a Complex Scalar Field," *Phys. Rev. D***52**, 5850-5856 (1995).

[46] E.W. Hirschmann, Unpublished notes, (1997).

[47] S. Hod and T. Piran, "Critical Behavior and Universality in Gravitational Collapse of a Charged Scalar Field," *Phys. Rev.* **D55**, 3485-3496 (1997).

[48] S. Hod and T. Piran, "Fine-Structure of Choptuik's Mass-Scaling Relation," *Phys. Rev.* **D55**, 440-442 (1997).

[49] O. Iguchi, A. Hosoya, and T. Koike, "Renormalization Group Approach to Einstein Equation in Cosmology," LANL preprint: gr-qc/9709042 (1997).

[50] A.I. Janis, E.T. Newman, and J. Winicour, "Reality of the Schwarzschild Singularity," *Phys. Rev. Lett.* **20**, 878-880 (1968).

[51] P. Jetzer and D. Scialom, "Dynamical Instability of the Static Real Scalar Field Solutions to the Einstein-Klein-Gordon Equations," *Phys. Lett.* **A169**, 12-20 (1992).

[52] G. Johnson, "What a Physicist Finds Obscene," *NY Times*, Feb. 16, (1997).

[53] T. Koike, T. Hara, and S. Adachi, "Critical Behavior in Gravitational Collapse of Radiation Fluid: A Renormalization Group (Linear Perturbation) Analysis," *Phys. Rev. Lett.* **74**, 5170-5173 (1995).

[54] S.L. Liebling and M.W. Choptuik, "Black Hole Criticality in the Brans-Dicke Model," *Phys. Rev. Lett.* **77**, 1424-1427 (1996).

[55] S.L. Liebling, "Massless Scalar Field Collapse in Brans-Dicke Theory," M.A. thesis, The University of Texas at Austin, unpublished (1995).

[56] S.L. Liebling and E.W. Hirschmann, "Pair Production in the Collapse of a Hopf Texture," In preparation, (1998).

[57] S.L. Liebling, "Mutliply Unstable Black Hole Critical Solutions," In preparation, (1998).

[58] X. Luo, "Toroidal Symmetric Global Texture in O(3) σ-models," *Physics Letters B* **287**, 312-324 (1992).

[59] K. Maeda, M. Sasaki, T. Nakamura, and S. Miyama, "A New Formalism of the Einstein Equations for Relativistic Rotating Systems," *Prog. Theor. Phys.* **63**, 719-721 (1980).

[60] K. Maeda, "[(2+1)+1]-Dimensional Representation of the Einstein Equations," in *Proceedings of Third Marcel Grossmann Meeting on General Relativity*, ed. Hu Ning, (Science Press, 1983).

[61] D. Maison, "Non-Universality of Critical Behaviour in Spherically Symmetric Gravitational Collapse," *Phys. Lett.* **B366**, 82-84 (1996).

[62] R.L. Marsa, "Radiative Problems in Black Hole Spacetimes," Ph.D. Thesis, The University of Texas at Austin, unpublished, (1995).

[63] R.L. Marsa and M.W. Choptuik, "The RNPL User's Guide," `http://godel.ph.utexas.edu/Center/Rnpl_users_guide.html` (1995).

[64] C.W. Misner, K.S. Thorne, and J.A. Wheeler, *Gravitation*, (Freeman, New York, 1973).

[65] C.W. Misner, "Values and Arguments in Homogeneous Spaces," in *Essays in General Relativity*, ed. F.J. Tipler, (Academic Press, New York, 1980).

[66] T.F. Morris, "Electrodynamics of Charged Scalar Solitons," *Can. J. Phys.* **57**, 2171-2177 (1979).

[67] T. Nakamura, "General Relativistic Collapse of Axially Symmetric Stars Leading to the Formation of Rotating Black Holes," *Prog. of Theor. Physics* **65**, 1876-1890 (1981).

[68] L. Perivolaropoulos, "Nontopological Global Field Dynamics," *Phys. Rev.* **D46**, 1858-1862 (1992).

[69] T. Prokopec, A. Sornborger, and R.H. Brandenberger, "Texture Collapse," *Phys. Rev.* **D45**, 1971-1981 (1992).

[70] M.H.P.M. van Putten, "Approximate Black Holes for Numerical Relativity," *Phys. Rev.* **D54**, R5931-R5934 (1996).

[71] R. Rajaraman, *Solitons and Instantons* (North Holland Pub. Co., New York, 1982).

[72] S.H. Rhie and D.P. Bennett, "Hopf Textures," LANL preprint hep-ph/9206234 (1992).

[73] S.H. Rhie and D.P. Bennett, "Global Monopoles Do Not 'Collapse'," *Phys Rev. Lett.* **67**, 1173 (1991).

[74] L.F. Richardson, "The Approximate Arithmetical Solution by Finite Differences of Physical Problems Involving Differential Equations, with an Application to the Stresses in a Masonry Dam," *Phil. Trans. Roy. Soc.* **210**, 307-357 (1910).

[75] L. H. Ryder, *Quantum Field Theory* (Cambridge Univ. Press, Cambridge, 1996).

[76] L. Sadun, Personal communication (1998).

[77] N. Sanchez, "Harmonic Maps in General Relativity and Quantum Field Theory," in *Harmonic Mappings, Twistors, and σ-models*, Ed. P. Gauduchon, 270-305 (World Scientific, New Jersey, 1988).

[78] C. Schmidhuber, "On Water, Steam and String Theory," *Am. J. Phys.* **65**, 1042 (1997).

[79] S.L. Shapiro, S.A. Teukolsky, and J. Winicour, "Toroidal Black Holes and Topological Censorship," *Phys. Rev.* **D54**, 977-990 (1997).

[80] J. Shatah and A. Tahvildar-Zadeh, "Regularity of Harmonic Maps from the Minkowski Space into Rotationally Symmetric Manifolds," *Comm. on Pure and Applied Math.* **45**, 947-971 (1992).

[81] J. Shatah, "The Cauchy Problem for Harmonic Maps on Minkowski Space," in *Proceedings of the International Congress of Mathematicians, Volume 2*, 1126-1132 (Birkhauser Verlag, Boston, 1995).

[82] J. Shatah and A. Tahvildar-Zadeh, "On the Cauchy Problem for Equivariant Wave Maps," Comm. on Pure and Applied Math. **47**, 719-754 (1994).

[83] T.H.R. Skyrme, "A Non-linear Field Theory," *Proc. Roy. Soc. Lond.* **A260**, 127-138 (1961).

[84] A. Sornborger, "Semianalytical Study of Texture Collapse," *Phys. Rev.* **D48**, 3517-3521 (1993).

[85] A. Sornborger, S.M. Carroll, and T. Pyne. "The Collapse of Exotic Textures," *Phys. Rev.* **D55**, 6454-6456 (1997).

[86] R.F. Stark and T. Piran, "A General Relativistic Code for Rotating Axisymmetric Configurations and Gravitational Radiation: Numerical Methods and Tests," *Computer Phys. Reports* **5**, 221-264 (1987).

[87] M. Struwe, "Regularity Results for Harmonic Maps of Minkowski Space," in *Nematics*, 357-269 (Kluwer, Boston, 1991).

[88] A. Vilenkin and E.P.S. Shellard, *Cosmic Strings and Other Topological Defects*, (Cambridge Press, Cambridge, 1994).

[89] R. M. Wald, *General Relativity* (The Univ. of Chicago Press, Chicago, 1984).

[90] R. M. Wald, "Gravitational Collapse and Cosmic Censorship," LANL gr-qc/9710068, (1997).

[91] S. Weinberg, *Gravitation and Cosmology* (Wiley, New York, 1972).

[92] C.M. Will, *Theory and Experiment in Gravitational Physics*, (Cambridge, New York, 1993).

[93] Y. Wu and A. Zee, "A Closed-string (or Ring) Soliton Configuration with Non-zero Hopf Number," *Nuclear Physics* **B324**, 623-629 (1989).

[94] M. Wyman, "Static spherically symmetric scalar fields in general relativity," *Phys. Rev.* **D24**, 839-841 (1981).

[95] J.M. Yeomans, *Statistical Mechanics of Phase Transitions*, (Clarendon, Oxford, 1992).

[96] J.W. York, Jr. and T. Piran, "The Initial Value Problem and Beyond," in *Spacetime and Geometry*, ed. by Richard A. Matzner and L. C. Shepley, (UT Press, Austin, 1982).

Vita

Steven Lawrence Liebling, the son of Carol Sue Liebling and Norman Harris Liebling, was born in Phoenix, Arizona, on November 27, 1970, After graduating from Clear Lake High School in Houston, Texas, in 1989, he traveled north to study physics at Brown University. He spent his junior year abroad studying Mandarin at the Chinese University of Hong Kong. He received an A.B. from Brown University in May, 1993. After completing research with Peter Timbie, Physics Professor at Brown University, he entered The Graduate School at The University of Texas at Austin in August, 1993. While studying towards completion of a doctorate, he received an M.A. for work with Matthew W. Choptuik in May, 1995. On March 15, 1998, while completing this dissertation and seeking employment, he married Tiffany Christina McKee.

Permanent address: 807 B East 45th Street
Austin, Texas 78751

This dissertation was typeset with LaTeX[‡] by the author.

[‡] LaTeX is a document preparation system developed by Leslie Lamport as a special version of Donald Knuth's TeX Program.